

AN ABSTRACT OF THE THESIS OF

Thomas J. Gannon for the degree of Doctor of Philosophy in Chemistry presented on October 20, 1999. Title: Time-of-Flight Scattering and Recoil Spectrometry (TOF-SARS) Applied to Molecular Liquid Surfaces: A New Approach to Surface Composition and Orientation.

Redacted for Privacy

Abstract approved: _____

Philip R. Watson _____

In spite of their importance in many systems, liquid surfaces have been explored at the microscopic level to a much lesser extent than solids. Most surface analysis must take place in vacuum, a major drawback for liquids. The technique of time-of-flight scattering and recoil spectrometry (TOF-SARS) has been applied to molecular liquid surfaces for the first time. The apparatus borrows key elements from previous TOF-SARS experiments on solids and from molecular beam scattering (MBS) and features excellent surface specificity and the ability to detect all elements. A high-vacuum time-of-flight spectrometer was developed for the purpose of measuring the surface atomic concentration of atoms in low-vapor pressure liquid samples, and hence to infer preferred surface orientations.

The TOF-SARS experiment involves surface bombardment with inert gas ions in the 1-3 keV energy range. During the interaction surface atoms may either (a) induce scattering of primary ions or (b) recoil from the surface. A binary collision

model describes the kinematics and dynamics of the interactions well, allowing prediction of velocities and probabilities of particles leaving the surface. Particles that reach a detector along a ~ 1.1 m flight path are separated by velocity, and signals are collected as a histogram, revealing relative measured intensities that are converted to ratios of accessible surface atoms. Comparing the measured atomic ratios with computer-simulated accessible atomic ratios for various possible orientations gives insight into preferred surface orientation.

A number of systems were explored in this work: liquids including a complementary pair of molecules having distinct 'head-tails' structures; glycerol as a highly H-bonded system, and a room-temperature molten salt. Preliminary results reveal that surface molecules appear in most cases to adopt some preferred orientation at the interface. The TOF-SARS technique was able to distinguish 'head' from 'tail' in molecules exhibiting that structure, suggesting only part of the head was accessible. In glycerol, all but two possible orientations were ruled out but the symmetrical nature of the molecule prohibits definitive assignment. The ionic liquid was found to have the cation and anion sharing the surface population roughly equally, and a preferred orientation for the substituted aromatic anion was discovered.

**Time-of-Flight Scattering and Recoil Spectrometry (TOF-SARS) Applied to
Molecular Liquid Surfaces: A New Approach to Surface Composition and
Orientation**

by

Thomas J. Gannon

A THESIS

submitted to

Oregon State University

in partial fulfillment of
the requirements for the
degree of

Doctor of Philosophy

Presented October 20, 1999

Commencement June 2000

Doctor of Philosophy thesis of Thomas J. Gannon presented on October 20, 1999.

APPROVED:

Redacted for Privacy

Major Professor, representing Chemistry

Redacted for Privacy

Chair of Department of Chemistry

Redacted for Privacy

Dean of Graduate School

I understand that my thesis will become part of the permanent collection of Oregon State University libraries. My signature below authorizes release of my thesis to any reader upon request.

Redacted for Privacy

Thomas J. Gannon, Author

Acknowledgements

The primary driving force behind my success in completing this project as we know it is our own Dr. Phil Watson. I owe him deep gratitude for the chance to undertake this major challenge, as well as the confidence that I could accomplish all the goals along the way. I fondly remember the day of my first visit to the OSU Department of Chemistry; after an entire morning of “So, what have you done with your life?,” his opening question was “How long since you’ve had something to drink?”. Thanks, Phil, for the breath of fresh air- on that day and whenever I needed it. At this point it would be nice to thank the Research Corporation, National Science Foundation, and OSU Research Council for financial support and Dr. Kenneth Seddon and Dr. Wayne Rabalais for generous assistance and helpful insights.

Very special recognition is due to my co-worker in the Watson group, Michael Tassotto. Various stages of construction and modification of the spectrometer used were completed jointly with Michael. With this being the first documentation of the development of the instrument, material has been included here that was originally either completed solely by Michael or partially by both of us, for the sake of completeness. The Contribution of Authors page that follows details his additions to this project. For these major contributions, as well as minor modifications that have made the spectrometer run more smoothly are too many to mention individually; I am deeply indebted to Michael. Of equal value to his material contributions are the numerous conversations we have shared in which his insight proved crucial to the success of this work.

On a similar note, I owe thanks to Jim Swirczynski for the ion optics power supply described in Chapter 3. I am certain that I could not have made this unit work as desired without the tireless and capable assistance that Jim provided throughout, and for this I am sincerely grateful.

All things considered, my parents have done the most important jobs in terms of getting me to this point. Everything went just as well as it could have, and I know they both worked extremely hard to make it so for the entire family. The material support came when I least expected; the advice came only when I asked, but the love and guidance was there from day one. No thanks could ever be enough, Mom and Dad.

The other folks in the family have given me much happiness and support over the years, making things a little easier and a lot nicer. Special thanks go in no particular order to Lisa, Jeanne, and Maureen, my elder sisters. Without your caring and understanding, as well as the occasional sound thrashing, I would not have maintained much sanity through it all. Thanks to you as well for the chance meetings you've made possible- the institution called brothers-in-law is still alive and well. The contributions of grandparents, aunts, uncles, and cousins on both sides of the family have made differences both big and small, but the whole is much greater than the sum of the parts. You've all been wonderful and I can only hope to thank all of you personally in some way.

The one person who has helped me the most on a daily basis to get through this madness is my wife, Hua. I'll never fully understand how she put up with my antics for these last (n) years, keeping my head on as straight as possible with one hand on

her own academic career and the other wrapped firmly around my future. I have no clue how one goes about graduate school without a partner, but I happen to have ended up with a great one. I'll thank you every day for what you've done for me.

Throughout the years I have had contact with many whom I would call friends as well as teachers, mentors, and co-workers- far too many to name. At OSU, the support staff has been exceptional- Joey, all the Karens, Jack, even Bob Boyer (it takes six years to realize he's not a bad guy after all). Ted Hinke, and Jim Swirczynski deserve a bit of special mention for aiding and abetting my research way beyond the call of duty. These two truly helped make this "excellent adventure" happen in style. I would put Mike Schuyler, John Loeser, Joe Nibler, and Mark Zabriskie high on the list at OSU, for an additional helping hand as needed. WPI added Steve Weininger, Grant McGimpsey, and Doug Weeks, among others. I can't forget the Westfield High School contingent- Miss Pat Turner, the late John Jachym, and Mr. J., who really got this chemistry ball rolling. If you're reading this, you know who you are.

The friends who have helped all of this happen are far too many to mention, but here goes:

- ▶ Eric P., Cathy M., and Berj H. for making high school livable.
- ▶ Marc L. and Joe W., the best roommates money can buy. Anywhere.
- ▶ Pooya T., for academic and fitness inspiration, and a benchmark for artistic standards...
- ▶ Michael and Mary Lynn. Hua and I can't count the ways you have enriched our lives since knowing you. Thanks so much.

- ▶ Rebecca, Lissa, Tony, and Jeff, plus a few sometime entries... thanks for the holidays, and my Fridays will never be quite the same (I guess???)
- ▶ George, glad we had the opportunity to experience the finer things in life. You are the man from now on- but don't get too comfortable.
- ▶ And oh yes, Mr. Diaz. Only the Shadow knows what we have managed to accomplish. *TO BE CONTINUED*

The music of one Leo Kottke was quite inspirational during the painful process of writing this work.

Through this all, I still wonder... what would Ray Bourque do?

Contribution of Authors

Dr. Phil Watson assisted with interpretation of data in chapters 5, 6, and 7.

Michael Tassotto contributed the design and construction of the diffusion pump control unit (Chapter 3.1.7) and in the latest version of the Wien filter (Chapter 3.3.1) that are presented here. The Figures 3.1.3 and 3.1.4 are my reproductions of original drawings done by Michael based on his work. Figure 3.3.1 is also based on Michael's original drawings of the ion optics and Wien filter. A control device for sample wheel operation and sample cell filling *in situ* not explicitly mentioned in this work was also designed and constructed solely by Michael.

Jim Swirczynski of the OSU Chemistry Department contributed to the development of the ion optics power supply described in Chapter 3.4. Figure 3.4.1 is my representation of Jim's schematic drawing of the circuit used.

TABLE OF CONTENTS

	<u>Page</u>
1. INTRODUCTION	1
1.1 Historical Development: Liquid Surfaces	1
1.2 Historical Development: Ion Interactions with Solid Surfaces	5
1.3 Motivation	8
1.4 Technical Challenges: Vacuum Considerations for Liquid Samples	9
1.4.1 Sample	10
1.4.2 Ion Source and Detector	12
1.5 TOF-SARS as a Viable Approach to Liquid Surface Investigations	13
2. KINEMATICS AND DYNAMICS OF LOW ENERGY ION-SURFACE COLLISIONS	14
2.1 Kinematics of Elementary Collisions	14
2.1.1 Single Scattering	15
2.1.2 Multiple Scattering	17
2.1.3 Direct Recoiling	18
2.1.4 Surface Recoiling	19
2.1.5 Cascade Sputtering	19
2.2 Energy Losses	20
2.2.1 Inelastic Losses	20
2.2.2 Surface Potential Losses	21
2.3 Dynamics of Elementary Collisions	21
2.3.1 Trajectory Calculations	21
2.3.2 Approximate Formalisms	22
2.4 Examples of Cross Sections	25

TABLE OF CONTENTS (Continued)

	<u>Page</u>
2.5 Separation of Scattering and Recoiling Particles	27
2.6 Trajectory Calculations	29
3. DETAILS OF THE TOF-SARS LIQUID SURFACES EXPERIMENT.....	30
3.1 Vacuum System.....	30
3.1.1 Introduction.....	30
3.1.2 Physical Resources.....	34
3.1.3 Roughing Vacuum	36
3.1.4 High Vacuum	38
3.1.5 Differential Pumping.....	41
3.1.6 Pressure Measurement	43
3.1.7 Diffusion Pump Control Unit.....	46
3.2 Ion Source.....	47
3.3 Ion Optics	51
3.3.1 Wien Filter.....	54
3.3.2 X-Y Deflectors.....	58
3.3.3 Tilt Positioner.....	59
3.3.4 Lens One Assembly.....	60
3.3.5 Lens Two Assembly.....	62
3.4 Optics Power Supply	61
3.4.1 Introduction.....	61
3.4.2 Principle of Operation.....	62
3.5 Ion Current Measurement.....	64
3.5.1 Introduction.....	64
3.5.2 Electrometers	65
3.5.3 Test Points.....	65
3.6 Sample Delivery	67

TABLE OF CONTENTS (Continued)

	<u>Page</u>
3.6.1 Design and Operation.....	70
3.6.2 Manipulator and Feedthroughs.....	73
3.7 Detection	73
3.8 Procedure.....	75
3.8.1 Sample Introduction.....	75
3.8.2 Pumpdown	76
3.8.3 Ion Gun Initialization.....	76
3.8.4 Sample Temperature Regulation.....	77
3.8.5 Creation of Liquid Surface.....	78
3.8.6 Ion Beam Optimization.....	78
3.8.7 Detection Optimization.....	78
4. INITIAL TESTING OF THE TOF-SARS SPECTROMETER AND EARLY RESULTS	80
4.1 Introduction	80
4.2 Solid Surfaces.....	80
4.3 First Observations of a Liquid Surface.....	87
4.4 Conclusion.....	90
5. FIRST OBSERVATION OF LIQUID SURFACE MOLECULAR ORIENTATION: "HEADS" OR "TAILS"	92
5.1 Introduction	92
5.2 Experimental	94
5.3 Results	94
5.4 Discussion	98

TABLE OF CONTENTS (Continued)

	<u>Page</u>
5.4.1 Experimental Intensities.....	98
5.4.1 Surface Atomic Ratios	99
5.5 Conclusion.....	103
6. TOF-SARS INVESTIGATION OF THE LIQUID GLYCEROL SURFACE.....	105
6.1 Introduction	106
6.2 Bulk Chemistry of Glycerol	106
6.3 Experimental	107
6.4 Results	107
6.4.1 Argon	107
6.4.2 Neon	110
6.5 Discussion	111
6.5.1 Spectral Intensity Ratios	111
6.5.2. Surface Atomic Ratios	120
6.5.3 Molecular Orientation Simulations.....	122
6.5.4 Quantitative Comparison of C/O Ratios	139
6.6 Conclusions	141
7. TOF-SARS INVESTIGATION OF A ROOM-TEMPERATURE IONIC LIQUID SURFACE	144
7.1 Introduction	144
7.2 Bulk Chemistry of Ionic Liquids.....	145
7.3 Experimental	146

TABLE OF CONTENTS (Continued)

	<u>Page</u>
7.4 Results	147
7.4.1 Argon	147
7.4.2 Neon	151
7.5 Discussion	158
7.5.1 Cation-Anion Surface Composition.....	158
7.5.2 Cation Surface Orientation.....	161
7.6 Conclusion.....	7.6
8. CONCLUDING REMARKS.....	168
8.1 General	168
8.2 ‘Head’ vs. ‘Tail’ Orientation.....	168
8.2.1 Summary	168
8.2.2 Future Studies	169
8.3 Glycerol Surface.....	170
8.3.1 Summary	170
8.3.2 Future Studies	171
8.4 Ionic Liquid Surfaces	172
8.4.1 Summary	172
8.4.2 Future Studies	173
BIBLIOGRAPHY	174
APPENDICES.....	182
Appendix A. Ion Beam Optimization and Pulsing.....	183
Appendix B. Supplemental TOF-SARS Data for Bis(2-Ethylhexyl) Chlorendate...186	
Appendix C. Calculated Recoil Cross Sections.....	183

LIST OF FIGURES

<u>Figure</u>	<u>Page</u>
1.3.1 Preferential ordering at the vacuum-liquid interface of a surfactant-like molecular liquid.....	9
2.1.1 Physical definition of angles.....	14
2.1.2 Schematic definition of angles in the liquid TOF-SARS experiment.....	15
2.4.1 Recoil cross sections for oxygen as a function of projectile mass.....	27
2.4.2 Recoil cross sections for 2.5 keV Ar ⁺ recoiling C, Cl, H, and Cu atoms.....	28
2.6.1 a. Example of a shadow cone simulation.....	29
3.1.1 Schematic overview of the TOF-SARS apparatus.....	32
3.1.2 Schematic diagram of the spectrometer vacuum system.....	34
3.1.3 Schematic of the diffusion pump control circuit.....	48
3.1.4 Detail of the sensing circuit for the diffusion pump control unit.....	48
3.2.1 Electron impact ion source.....	51
3.3.1 a. Expanded side view of the electrostatic ion optics elements.....	56
3.4.1 Ion optics power supply circuit.....	63
3.6.1 Frontal view of liquid sample cell.....	71
3.6.2 Overhead semi-exploded view of the lower half of the liquid sample cell.....	74
3.7.1 Schematic diagram of channeltron operation.....	76
4.2.1 Schematic of the solid sample mounting apparatus.....	82
4.2.2 TOF spectra of solid surfaces obtained using 3.0 keV Ar ⁺ incident ions.....	84
4.2.3 3 keV Ar ⁺ TOF spectra of contaminated graphite, before (297 K) and during (388 K) heating.....	86
4.2.4 Space-filling model of TTTS.....	87
4.3.1 3.0 keV Ar ⁺ TOF-SARS spectra from glycerol and the stainless sample wheel.....	89

LIST OF FIGURES (Continued)

<u>Figure</u>	<u>Page</u>
4.3.2 2.5 keV He ⁺ TOF-SARS spectrum of glycerol.....	90
5.1.1 Ball-and-cylinder representations of the DOP (A.) and BEHC (B.) molecules.....	93
5.3.1 TOF-SARS spectra using 3 keV Ar ⁺ ions from DOP (•) and BEHC (–).	95
5.3.2 TOF-SARS spectrum of BEHC using 2.5 keV Ne ⁺ ions.....	96
5.3.3 TOF-SARS spectra of BEHC as a function of energy.....	97
5.3.4 Difference spectrum (BEHC-DOP) based on the data in Fig. 5.3.1.....	98
5.4.1 Possible surface orientations of BEHC (A.-C.) and DOP (D.-F.).....	103
6.4.1 Composite of TOF-SARS spectra obtained from glycerol using 2.5 keV Ar ⁺ ions.....	110
6.4.2 Composite of TOF-SARS spectra obtained from glycerol using 2.5 keV Ne ⁺ ions.....	113
6.4.3 Composite of TOF-SARS spectra obtained from glycerol using 2.0 keV Ar ⁺ ions.....	116
6.5.1 Deconvolution of peaks for 2.5 keV Ne ⁺ on glycerol, neglecting the multiple scattering tail contribution.....	119
6.5.2 Deconvolution of peaks for 2.5 keV Ne ⁺ on glycerol, neglecting the multiple scattering tail contribution.....	120
6.5.3 Experimental intensity ratios as a function of incident angle α for 2.5 keV Ne ⁺ incident ions.....	122
6.5.4 Corrected atomic ratios as a function of incident angle α for 2.5 keV Ne ⁺ incident ions.....	124
6.5.5 A. $\alpha\alpha$ -glycerol.....	127
6.5.6 A1. $\alpha\alpha$ -glycerol “out-of-plane” orientation.....	128
6.5.7 A1. $\beta\gamma$ -glycerol “out-of-plane” orientation.....	128
6.5.8 LOS atomic ratios for horizontal “out-of-plane” orientations as a function of α	129
6.5.9 A1. $\alpha\alpha$ -glycerol orientations with “in-plane” carbon backbones.....	130

LIST OF FIGURES (Continued)

Figure	Page
6.5.10 “in-plane” horizontal orientations of $\beta\gamma$ -glycerol.....	131
6.5.11 LOS atomic ratios for horizontal “in-plane” glycerol orientations as a function of α	132
6.5.12 $\alpha\alpha$ -glycerol in vertical orientations.....	133
6.5.13 $\beta\gamma$ -glycerol in vertical orientations.....	133
6.5.14 LOS atomic ratios vertical glycerol orientations as a function of α	134
6.5.15 $\alpha\alpha$ -glycerol tilted in Y.....	136
6.5.16 $\beta\gamma$ -glycerol tilted in Y.....	136
6.5.17 LOS atomic ratios for backbone orientations tilted in Y as a function of α	137
6.5.18 $\alpha\alpha$ -glycerol tilted in X.....	138
6.5.19 $\beta\gamma$ -glycerol tilted in X.....	138
6.5.20 LOS atomic ratios for glycerol orientations tilted in X as a function of α	140
6.6.1 Plausible orientations of glycerol.....	142
6.6.2 Comparison of the experimental C/O ratio with the closest LOS-simulated C/O ratios.....	143
7.2.1 Examples of ionic liquids.....	147
7.4.1 Composite of TOF-SARS spectra obtained from [bmim][PF ₆] using 2.5 keV Ar ⁺ ions.....	149
7.4.2 Composite of TOF-SARS spectra obtained from [bmim][PF ₆] using 1.5 keV Ar ⁺ ions.....	151
7.4.3 Composite of TOF-SARS spectra obtained from [bmim][PF ₆] using 2.5 keV Ne ⁺ ions.....	153
7.4.4 Composite of TOF-SARS spectra obtained from [bmim][PF ₆] using 2.0 keV Ne ⁺ ions.....	155
7.4.5 Fitted 2.5 keV Ar ⁺ TOF-SARS of [bmim][PF ₆].....	157

LIST OF FIGURES (Continued)

<u>Figure</u>	<u>Page</u>
7.4.6 Fitted 2.0 keV Ne ⁺ TOF-SARS of [bmim][PF ₆]	158
7.5.1 TOF-SARS spectra of squalane and [bmim][PF ₆].....	162
7.5.2 Rotations of the [bmim] cation relative to the surface-parallel ring axis.....	163
7.5.3 90° azimuthal rotations of [bmim] viewed at $\alpha=36^\circ$	165
7.5.4 90° azimuthal rotations of [bmim] viewed at $\alpha=36^\circ$	167

LIST OF TABLES

<u>Table</u>	<u>Page</u>
3.1 Rough Pump Specifications.....	38
3.2 High/UHV Vacuum Pump Specifications.....	40
4.1 TOFs for 3.0 keV Ar ⁺ events.....	85
4.2 TOFs for 2.5 keV Ar ⁺ events.....	91
5.1 Bulk Properties of DOP and BEHC.....	93
5.2 TOFs for 3.0 keV Ar ⁺ events.....	96
5.3 TOFs for 2.5 keV Ar ⁺ events.....	97
5.4 Experimental intensity ratios and derived atomic ratios for DOP and BEHC.....	101
6.1 Bulk properties of glycerol.....	108
6.2 TOFs for 2.5 keV Ar ⁺ events.....	109
6.3 TOFs for 2.5 keV Ne ⁺ events.....	114
6.4 TOFs for 2.0 keV Ne ⁺ events.....	117
6.5 Spectral intensity ratios for glycerol (2.5 keV Ne ⁺ data).....	123
6.6 Average deviations between LOS and experiment C/O Ratios.....	142
7.1 TOFs for selected 2.5 keV Ar ⁺ events.....	150
7.2 TOFs for selected 1.5 keV Ar ⁺ events.....	152
7.3 TOFs for selected 2.5 keV Ne ⁺ events.....	154
7.4 TOFs for 2.5 keV Ne ⁺ events.....	156
7.5 Spectral Intensity Ratios in [bmim][PF ₆] from 2.5 keV Ar ⁺ and 2.0 keV Ne ⁺ data.....	159
7.6 Surface Atomic Ratios in [bmim][PF ₆] based on 2.5 keV Ar ⁺ and 2.0 keV Ne ⁺ data.....	159

LIST OF TABLES (Continued)

<u>Table</u>		<u>Page</u>
7.7	Estimated C and H atoms per [bmim] cation for the azimuthal rotations in Fig. 7.5.3 ($\alpha = 36^\circ$).....	165

LIST OF APPENDIX FIGURES

<u>Figure</u>	<u>Page</u>
B.1 Composite of TOF-SARS spectra obtained from BEHC using 3.0 keV Ar ⁺ ions.....	188
B.2 Composite of TOF-SARS spectra obtained from BEHC using 2.5 keV Ar ⁺ ions.....	189
B.3 Composite of TOF-SARS spectra obtained from BEHC using 2.0 keV Ar ⁺ ions.....	190
B.4 Composite of TOF-SARS spectra obtained from BEHC using 1.5 keV Ar ⁺ ions.....	191
B.5 Composite of TOF-SARS spectra obtained from BEHC using 2.5 keV Ne ⁺ ions.....	192

*For Doris V. Painter, who always encouraged me to
do better in the least subtle of ways.*

Time-of-Flight Scattering and Recoiling Spectrometry (TOF-SARS) Applied to Molecular Liquid Surfaces: A New Approach to Surface Composition and Orientation

1. Introduction

1.1 Historical Development: Liquid Surfaces

The origins of interest in the study of liquid surfaces are not well documented, but reach back to ancient times, when the calming effect of oil films on turbulent seas was first observed (Giles 1969). Some of the earliest experiments regarding this phenomenon, and liquid surface behavior as a whole, can be attributed to Benjamin Franklin, arising from his own observations in 1757. Soon afterward he conducted a series of his own experiments, the first of which demonstrated the rapid spreading and remarkable calming effect of a “teaspoonful” of olive oil over the rough surface waves of a local pond on a windy day. However, since the initial interest, experiments regarding the nature of liquid surfaces have lagged far behind those studies done on solids.

Molecular liquid surfaces have extremely consequential roles in many naturally and technologically important processes. These interface processes include mass transfer, such as evaporation/condensation and solvation of gas-phase species; energy transfer in the form of heating and cooling; and reactions involving surface-active films. Understanding of these interface processes hinges on detailed information of the interface at the molecular level, including atomic compositions, molecular orientations, and gas-liquid exchange and solvation dynamics.

Theoretical predictions for the microscopic interfacial structures of a broad sampling of different liquids, ranging from simple atomic liquids to molten metals to liquid crystals, have been reported from the mid 1980s on (Croxtton 1986). Liquid metals are perhaps the best understood of these systems (Rice, Gryko et al. 1986), but relatively little work has yet been devoted to molecular liquid interfaces.

Experimental methods explored, until recently, have yielded some interesting qualitative descriptions of molecular liquid interfacial properties. However, many of them rely on *a priori* theoretical treatments or approximations, and most are capable only of providing information indirectly through rigorous treatment of the data. Surface tension measurements can indirectly provide descriptive insights into surface composition molecular orientations (Macritchie 1990). In the area of surfactants, radioactive tracers have been used to measure surface excess quantities for aqueous solutions, a more direct approach (Hall, Pethica et al. 1970). Light scattering techniques can be used to determine the interface profile thickness, assuming that the functional form for the profile is known (Beaglehole 1986; Langevin 1992). Ellipsometry investigations of simple molecules have suggested that in water the surface molecules are aligned with the dipole normal to the interface, whereas CS₂ exhibits little preferential ordering (Beaglehole 1983).

A number of new non-vacuum based methods for probing the precise structure of the liquid-vapor interface have appeared over the last decade or so. Neutron and X-ray reflectivity measurements have been performed on liquid metals, surfactant films, and liquid crystals (Schlossman 1992). Simple molecular liquids generate weak signals, hindering the effectiveness of these techniques, but probes of the liquid-vapor

interface of water have been implemented through X-ray (Schwartz, Schlossman et al. 1990) and neutron scattering (Penfold and Thomas 1990). Each of these methods lacks the ability to extract a real-space model of the surface, and requires comparison of measured reflectivities with calculated values from an assumed profile. Neutron scattering exhibits the advantageous capability of distinguishing hydrogen from deuterium, allowing for isotopic substitution as a diagnostic tool.

The period from 1986 to present has seen significant advances in laser technology, accelerating the development of new experimental techniques for surface investigations, namely sum-frequency generation (SFG) spectroscopy (Shen 1989) and second harmonic generation (SHG) spectroscopy (Eisenthal 1996). Possible over a broad pressure range (UHV to atmosphere), both SFG and SHG have contributed qualitative information on the orientations of molecules at liquid interfaces but not without limitations. The SHG experiment has been used to investigate neat liquids and solutions. One study involving aqueous solutions of phenols, which display a strong nonlinear optical response along one axis, determined the long axis tilt angle to be $50 \pm 5^\circ$ relative to the surface normal (Hicks, Kemnitz et al. 1986)(Hicks et al, 1986). An early investigation of pure water indicated that the protons are oriented downward in the surface, but the authors noted that the result was inconclusive without a better understanding of the molecular hyperpolarizability of water (Goh, Hicks et al. 1988). Sum-frequency generation spectroscopy has been used to probe adsorbates on solid substrates, Langmuir films, and to the liquid-vapor interface. The technique has high surface sensitivity and provides surface vibrational spectra, which unlike SHG can be used to positively identify the surface molecules. Laser crystals, though continually

improving, limit the range of optical frequencies, making observation of some vibrational modes impossible. Orientation information is obtained through investigation of the polarization dependence of the SFG signal. Results for orientations of pure liquids have appeared for the methanol methyl group (Superfine, Huang et al. 1990) and water (Wolftrum, Graener et al. 1993), as well as several binary systems: ammonia/water (Simonelli, Baldelli et al. 1999), HCl/water (Baldelli, Schnitzer et al. 1998), and aqueous surfactants (Gragson, McCarty et al. 1996). SFG additionally has been used to probe buried liquid/liquid interfaces (Gragson and Richmond 1997; Chen, Gracias et al. 1999), and is capable of identifying species adsorbed on solid substrates.

Of the vast array of vacuum-based techniques applied to solid samples, a few have been adapted for use on liquid surfaces. Low vapor-pressure liquids have been probed through the use of both X-ray and ultraviolet photons in photoelectron spectroscopy (Siegbahn 1985). XPS suffers some loss of surface sensitivity due to the large sampling depth, and thus correlates more to bulk phenomena; nonetheless, an angle-resolved study of tetrabutylammonium iodide in formamide suggested some surface segregation relative to the bulk (Holmberg, Moberg et al. 1986). UV-photoelectron spectroscopy also has suggested surface concentration enhancement of solute (Ballard, Jones et al. 1984). Another version of photoelectron spectroscopy, Penning ionization electron spectroscopy (PIES, also denoted as MIES for metastable impact electron spectroscopy) has been applied to various neat liquids, mixtures, and solutions. PIES utilizes the probability of molecular orbital overlap between incident excited-state atoms and surface molecules to infer surface orientations and surface excesses. Investigations have been performed for formamide (Keller, Morgner et al.

1986), n-methylformamide (Keller, Morgner et al. 1986), formamide/benzyl alcohol (Morgner, Oberbrodage et al. 1991), t-butyl ammonium iodide in formamide (Morgner and Oberbrodage 1995) are among several others. Molecular beam scattering (MBS) has been explored more as a method for investigating energy transfer mechanisms between the liquid interface and molecules in the vapor phase than as a method for determining surface structures. While portions of the experimental setup are quite applicable to the presently used apparatus, the information gained can only indirectly infer surface orientations. Some systems investigated include Ne, CH₄, NH₃, and D₂O collisions with both glycerol and the hydrocarbon squalane (Saecker and Nathanson 1993), H₂O from concentrated sulfuric acid (Govoni and Nathanson 1994), inert gases from molten metals (Ronk, Kowalski et al. 1996), and penetration of water through perfluorinated polyether films (Porter, Klassen et al. 1997).

1.2 Historical Development: Ion Interactions with Solid Surfaces

Surface analysis investigations through interactions between energetic ions and solids became increasingly popular during the 1960s on the heels of recent improvements in ultra-high vacuum technology. The year 1961 saw a series of chemical surface analysis investigations using large-angle scattering of charged particles (Turkevich 1961). Later in the decade, MeV-alpha particle backscattering from the lunar surface generated considerable interest (Turkevich 1968). Concurrently, Smith (Smith 1967) developed a spectrometer that utilized 1 keV inert gas ions scattering from a solid: an electrostatic analyzer monitored energy lost through collisions at the surface, yielding information about the target atoms. The spectra

generated displayed the capability to differentiate target atoms of varying masses (Chu, Mayer et al. 1978). Within that decade, computer simulations (Robinson and Oen 1963) demonstrated that ions penetrating a surface in different directions would have widely varying transmission probabilities, a feature that would lead to important structural information for bulk crystal studies as well (Gemmel 1974). Thorough experimental and theoretical studies of keV-energy ion scattering were begun in the early 1960s in the Soviet Union, but the information has only recently become available in the English language (Mashkova 1985, Parilis, 1993 #145).

The late 1970s brought a wealth of interest in several related techniques for surface analysis, including Rutherford back-scattering spectrometry (RBS, MeV-energy projectiles), medium energy ion scattering (MEIS, ~100 keV ions), and low energy ion scattering (LEIS), or simply ion scattering spectrometry (ISS, 1 to 10 keV ions). All of these came into wider use as tools for investigating crystalline structure near the surface of a crystalline solid (Poelsema and Boers 1977; Stensgaard, Feldman et al. 1978; Turkenburg, Smeenk et al. 1978). These techniques exploited local “shadowing” and “blocking” effects of incident ions by atoms in the surface layers, and geometric analysis of angular dependencies and backscattering yields allowed measurements of atomic positions on the surface. Shadowing refers to the inability of an incident ion to penetrate directly behind a surface atom, and blocking describes the analogous effect of surface atoms on the ability of the projectiles to leave the surface after penetration occurs.

Just prior to the advent of the ion scattering experiment used for the present work, ion beams were used to probe surfaces in both ion scattering spectrometry (ISS)

and secondary ion mass spectrometry (SIMS). Both of these techniques involve projection of energetic ions onto a target surface and analysis of either scattered ions (ISS) or secondary ions produced (SIMS). Electrostatic analyzers were the best available detectors, and they were limited exclusively to ion detection, and operable only in single-channel mode meaning that a large ion dose is necessary to generate data. This problem is amplified by the fact that $\geq 90\%$ of all scatters and secondaries are neutralized during the collision processes (Buck, Wheatley et al. 1978). SIMS is inherently destructive, as large clusters and fragments as well as ions and atoms are constantly removed from the surface under bombardment.

In order to overcome the destructive nature of these techniques, Buck and co-workers employed a multiplier-type detector (Johnston MMI) in the late 1970s, capable of detecting both energetic neutrals and ions, thus making more efficient use of the ion dose used. Additionally, the device is operable in a multichannel mode, so it can collect a TOF spectrum in a brief time relative to a single-channel device generating an energy spectrum through data collection in sequential discrete energy steps. These features dramatically decrease the ion dose necessary for generating a spectrum by a factor of ca. 10^4 (Buck, Wheatley et al. 1978), an important step toward a non-destructive technique. The introduction of the multiplier detector paved the way for scattering and recoil spectrometry experiments as effective means of surface analysis.

Recoil spectrometry investigations began in earnest soon after the introduction of a suitable detector. A number of studies from the early 1980s on demonstrated the capabilities of (TOF-SARS) for solid surface analysis (Eckstein 1981; Rabalais, Schultz et al. 1983; Boers 1984; O'Connor, MacDonald et al. 1986). The Rabalais

group rapidly explored the TOF-SARS technique extensively for a variety of systems, including alkali halide salts (Rabalais, Schultz et al. 1983), chemisorbed O_2 , H_2O , and H_2 on metal substrates (Mintz, Schultz et al. 1984; Schultz, Mintz et al. 1984; Schultz, Jo et al. 1985), metal oxides (Aduru and Rabalais 1987), and polyimide decomposition (Contarini, Schultz et al. 1987). In all, a wide variety of systems have been investigated, exemplifying the versatility of the technique for solid surfaces. Many of these investigations also involved standard complementary techniques such as SIMS, X-ray photoelectron spectroscopy (XPS), and/or ultraviolet photoelectron spectroscopy (UPS).

1.3 Motivation

In view of previous investigations into the ordering and orientations of molecules at liquid surfaces, further work is justified. Still missing is a direct method for gaining insight into the true composition of the outermost atomic layer of the surface. We document here the application of the time-of-flight scattering and recoil spectrometry (TOF-SARS) technique to molecular liquid surfaces. The goals of this work are to determine whether TOF-SARS is a viable and feasible method for molecular orientation studies of liquid surfaces, and to demonstrate its capabilities in exploratory investigations of a number of representative molecular liquid systems.

The primary goal of this project is to assemble a working time-of-flight ion scattering spectrometer capable of supporting liquid samples for analysis, and evaluate its usefulness in that capacity. The spectrometer will consist of a high-vacuum chamber designed to accommodate a pulsed ion source, a cell for liquid sample

introduction, and a time-of-flight detection scheme. Once assembled and operational, the spectrometer will be used to probe several systems including:

- A polysiloxane, commonly used as a diffusion pump fluid (condensed on stainless steel)
- A pair of distinct “head-tail” molecules, in order to determine gross orientations
- Glycerol as an example of a hydrogen-bonding liquid
- An ionic liquid comprised of an inorganic anion and organic cation

The work presented here is by no means exhaustive- these systems offer general representation of several different classes of molecules, and future work will include more extensive studies of some of the individual classes.

The type of information sought includes the orientation of molecules at the air-liquid interface; we seek direct experimental evidence of the presence of preferential orientation. Figure 1.3.1 schematically illustrates preferential surface ordering of a surfactant-like molecule having distinguishable “head and tail” features, representative of the type of information we expect to obtain. In principle, the technique may also be used to probe for the presence and degree of surface segregation of solutions, a situation in which the interface number density of solute particles differs from that of the bulk.

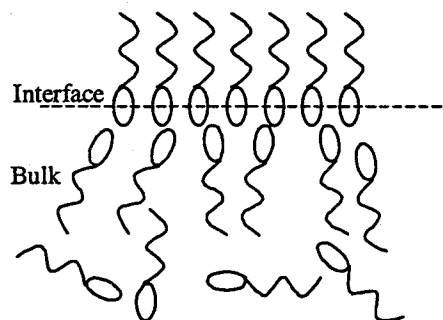


Figure 1.3.1 Preferential ordering at the vacuum-liquid interface of a surfactant-like molecular liquid.

1.4 Technical Challenges: Vacuum Considerations for Liquid Samples

1.4.1 Sample

It is well known that solid surface investigations must be carried out under ultra-high vacuum (UHV) conditions. One obvious reason for this need is the cleanliness of the surface; the higher the background pressure in the sample region, the sooner that contamination of the surface will occur. The experimental design of the vacuum system must take into account the time scale of the experiment relative to the time it takes for surface coverage by contaminants; the longer the experiment takes, the higher the vacuum requirements. Generally for solids the vacuum must be maintained on the order of 10^{-8} Torr or lower, or in UHV, in order to complete an investigation before the surface is contaminated beyond acceptable limits. Additionally, the sample can be prepared repeatedly *in vacuo*- cleaning by ion sputtering, re-exposure to adsorbates, etc. However, liquid samples must be handled differently, as the phenomena occurring during an experiment differ dramatically from those of solids.

The intrinsically higher vapor pressure of liquids dictates that material leaves the surface at a higher rate, thus contributing to a higher ambient pressure which can lead to faster surface contamination. An obvious necessity is to remove the vapor produced by evaporation of the sample, a task in part accomplished by large diffusion pumps capable of high pumping speeds. One method for limiting the amount of surface contamination is to continuously prepare a fresh liquid surface, by means such as a liquid jet or a rotating wheel dipped in a reservoir of sample. In this way, the surface is refreshed before contamination can become a problem. The chosen solution

to this problem, a rotating wheel mechanism of sample introduction, will be discussed in detail in the experimental chapter of this work.

The second major vacuum-related consideration, true especially for particle beam- based spectrometries such as TOF-SARS, has to do with transport of the ion projectiles onto and away from the target in the form of scattered and recoiled particles. The mean free path (λ) is defined as the average distance a particle can travel in a straight line before colliding with another particle. From kinetic theory of gases, the mean free path is (O'Hanlon 1980)

$$\lambda = \frac{1}{2^{1/2} \pi d_0^2 n} \quad 1.4.1$$

where d_0 is the molecular diameter and n is the gas density. A simple estimate for air at room temperature is

$$\lambda = \frac{6.6}{P} \quad 1.4.2$$

where λ has units of mm and P is the pressure in pascals. This quantity is primarily dependent on the pressure of ambient gas; it follows that the lower the background pressure, the larger the mean free path for the important particles. The importance of the mean free path is magnified when TOF techniques are involved, as detection of scattered and recoiled particles hinges on whether they are able to traverse the ~1 m flight path. Thus it is imperative that the vacuum is capable of removing ambient gases from the TOF region of the instrument.

The mean free path is also a prime concern in the region closest to the sample itself, where beam-target interaction is to take place. This volume is subject to the

highest pressure due to evaporating sample material, and as a result suffers from the shortest mean free path for particles. The mean free path quickly decreases as a function of the pressure, and becomes a significant concern, especially in the vicinity of the sample where the equilibrium pressure is highest. For a pressure of 10^{-5} Torr, λ approaches the order of a few centimeters in air, and will be less than that for bulkier molecules including most of the samples considered here. This fact poses a major challenge to the experiment involving transport of the beam into and out of the sample region, a consideration to be discussed in greater detail in the experimental section. It is also important to recall that the desired signal should originate from the surface of the condensed liquid, and not from ambient vapor.

1.4.2 Ion Source and Detector

A less obvious problem is associated with the cleanliness of components not in close proximity to the liquid sample. Condensation of stray sample vapor on ion optics could lead to electrostatic charging problems; presence of vapor in the ionization chamber of the ion source reduces its lifetime, and certainly would affect the detector's performance, either damaging the component or altering its efficiency. In order to reduce these risks the vacuum system must include barriers against contamination by sample vapor. The present system employs differential pumping, which allows "separation" of adjacent regions of the instrument, in the sense that solid barriers with small apertures allow transport of the desired particle beam while limiting migration of sample to areas that should be kept clean. The challenges presented here are

significant obstacles that must be overcome; this work provides details of the means by which they are handled and an evaluation of the success in doing so to this point.

1.5 TOF-SARS as a Viable Approach to Liquid Surface Investigations

The TOF-SARS technique as developed for solid surfaces has several beneficial attributes. Foremost is its surface sensitivity; the experimental conditions are chosen such that the spectral signals originate from the outermost atomic layer, within the top few Å of the surface, a very limited sample depth. Another feature is its elemental sensitivity- it can detect all elements, including hydrogen, and this cannot be said for many of the previously developed surface spectroscopies. TOF-SARS has the capability to resolve H from D, making it a candidate for isotopic labeling studies. Although an interesting possibility, at present this idea has limited application as isotope-substituted samples are expensive and of somewhat limited availability.

It should be noted that some of the information available when this technique is applied to solids will not be possible with liquids. Where the atoms in solids remain essentially stationary relative to their neighbors during an experiment, allowing spatial resolution of the surface, atoms in liquids are subject to molecular tumbling that averages out the absolute spatial information one can obtain for solids. We expect to obtain a time-averaged atomic composition of the liquid surface, from which we can obtain the average orientation of the molecules and information on solute surface segregation. Application of TOF-SARS to molecular liquid surfaces should provide a great deal of insight into molecular orientations at the interface.

2. Kinematics and Dynamics of Low Energy Ion-Surface Collisions

2.1 Kinematics of Elementary Collisions

The kinematics and dynamics of elementary particle collisions are well understood for incident ion energies in the kiloelectron volt range. The kinematics are described well by the binary elastic collision model, and the laws of conservation of kinetic energy and linear momentum can be used to describe the trajectories and

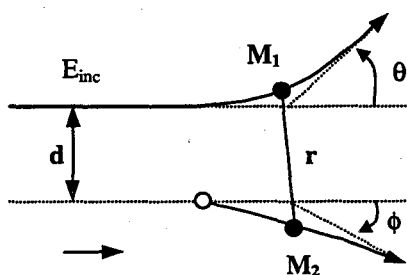


Figure 2.1.1 Physical definition of angles. E_{inc} = direction of incidence, M_1 = projectile, M_2 = target, d = impact parameter, θ = LAB scattering angle, ϕ = LAB recoil angle.

energies of recoiled and scattered particles (Smith 1967). In the classical treatment, the recoiling particles are rigid spheres, and the repulsive potential is zero before contact and infinity when the distance of closest approach reaches the sum of the radii of the two colliding spheres. The important angles of scattering (θ) and recoiling (ϕ) in the laboratory frame are defined in Figure 2.1.1.

The figure represents the projectile and target as M_1 and M_2 respectively, and defines the scattering and recoil angles relative to the incident ion direction. In terms of the experiment, Figure 2.1.2 defines the important angles as they apply. The figure is a schematic view from above the beam-sample interaction region. The plane of the sample and the beam axis define the incident angle α . An additional angle β is defined as the difference between the scattering/recoil angle and the incident angle; the relationship between these angles is

$$\alpha + \beta = \theta = \phi = 45^\circ$$

2.1.1

The interaction consists of a collision between an incident particle of mass m_1 and energy E_0 and a target atom with mass m_2 that is initially at rest. If no interaction occurs between the impinging particle and the target, the projectile passes by at a distance p from the target; this distance is called the impact parameter of the collision. As a result of the collision, the projectile is scattered through an angle θ relative to the initial direction of motion, and the target atom is recoiled through an angle ϕ relative to the initial motion. The

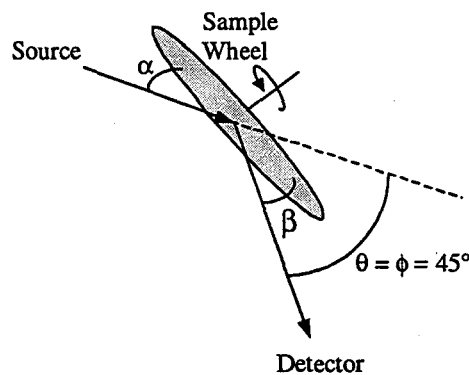


Figure 2.1.2 Schematic definition of angles in the liquid TOF-SARS experiment. θ =scattering, ϕ =recoil, α =incident, β =exit.

major identifying spectral features corresponding to these scattering and recoil events can be categorized in five simple classifications described below, for the purpose of interpretation and discussion of spectra. It should be noted that these descriptions are purely theoretical, and thus greatly simplified compared to the experimentally occurring events; they generally account for single collision events, whereas both the projectile and target are subject to many interactions.

2.1.1 Single Scattering

Single scattering (SS) describes the case of one large-angle deflection of a projectile that is preceded and followed by a small number of small deflections that do

not result in significant trajectory changes or energy losses. The result in the TOF spectrum is typically a sharp scattering peak whose energy is near the theoretical single-collision energy (Rabalais 1988). This energy (E_s) of a particle scattered from a single-collision event is given by (Marion and Thornton 1995):

$$E_s = E_0 \frac{m_1^2}{(m_1 + m_2)^2} \left[\cos \theta \pm \left(\left[\frac{m_2}{m_1} \right]^2 - \sin^2 \theta \right)^{1/2} \right]^2 \quad 2.1.2$$

If the mass of the projectile is less than or equal to the mass of the target atom ($m_1 \leq m_2$), then the positive sign of equation 2.1.2 is used. If the mass of the impinging particle is greater than that of the target ($m_1 > m_2$), both signs are used. The energy of the scattered particle in this case is a double-valued function of the scattering angle, meaning that there are two E_s values for each θ . This somewhat unusual finding is due to the fact that the energy transferred during the collision can result in either a “fast” scatter or a “slow” scatter depending on the magnitude of the energy transfer. For the case of $m_1 > m_2$, the maximum (critical) angle for occurrence of SS is (Rabalais 1988):

$$\theta_{\max} = \sin^{-1} \left(\frac{m_2}{m_1} \right) \quad 2.1.3$$

Above this angle, no single scattering is observed, and the physical significance is that there is a limit to the change in scattering trajectory induced during the interaction. For example, a light target (m_2) such as carbon cannot markedly alter the trajectory of a heavy projectile (m_1) such as argon. This is helpful to us in some cases, allowing fair separation of scattering signals from recoil signals, a topic to be discussed below. The corresponding predicted flight time t_{ss} for the SS particle is (Rabalais 1991):

$$t_{ss} = \frac{l(m_1 + m_2)}{(2m_1 E_0)^{1/2}} \left\{ \cos \theta + \left[\left(\frac{m_2}{m_1} \right)^2 - \sin^2 \theta \right]^{1/2} \right\} \quad 2.1.4$$

where l is the distance from target to detector.

2.1.2 Multiple Scattering

Multiple scattering (MS) is the designation for scattering events where more than one large-angle deflection occurs. Again, this treatment assumes that two or more deflections significantly alter the particle trajectory, and any other interactions are minor by comparison, affecting the trajectory very little. The resulting spectral feature is a scattering peak that is broader than the SS peak and appears at slightly higher energy (Rabalais 1995). The high-energy limit is approximated by repeated application of equation 2.1.2 for each successive large-angle deflection. Considering the simple example of a double collision, the equation would be applied twice using a scattering angle of $\theta/2$, and E_0 for the second application would be E_s from the first application. The approximation converges rapidly to the MS high-energy limit as several small angle deflections are summed to represent the total scattering angle. The width of the MS peak is attributed to the fact that several different combinations of small-angle deflections can lead to a similar overall trajectory. In addition to the high-energy signal, MS can contribute a broad, low-intensity feature at lower energies than the SS peak. The slower scattered particles arise from other combinations of deflections, such as a backward-scattering event followed by a forward scatter, or by a sequence

involving deeper penetration of the surface, incurring additional energy losses before emerging as a scattered particle.

2.1.3 Direct Recoiling

Perhaps the most useful of the binary events in terms of gaining insight into the composition of the surface under study is direct recoiling (DR). This event occurs as the result of a single, direct collision of a primary incident projectile with a target atom, ejecting (recoiling) that target atom out of the surface. DR produces energetic atoms of a relatively narrow kinetic energy distribution. The energy E_R of a recoiled particle is given by (Marion and Thornton 1995):

$$E_R = \frac{4E_0 m_1 m_2}{(m_1 + m_2)^2} \cos^2 \phi \quad 2.1.5$$

and the corresponding predicted flight time for recoils t_{DR} is (Rabalais 1988):

$$t_{DR} = l \frac{m_1 + m_2}{(8m_1 E_0)^{1/2} \cos^2 \phi} \quad 2.1.6$$

Geometry considerations dictate that DR can occur only in the forward direction, or where $\phi < 90^\circ$. Recoil energies are highest for small recoil angles and similar projectile/target masses, the ideal conditions for maximum energy transfer.

2.1.4 Surface Recoiling

A sequence involving a combination of recoils and scattering collisions gives rise to surface recoiling (SR). For example, a primary incident ion can DR a light surface atom into a heavier surface atom, and the lighter atom may scatter into a scattering direction, usually but not always backscattering. This type of sequence is capable of producing energetic target atoms in backscattering trajectories, and is particularly sensitive to light atoms such as H which may encounter heavier surface atoms (Rabalais 1988). The spectral result is generally a low-intensity feature occurring on the short-TOF side of the DR signal for a given atom. Broadening of the feature occurs as a result of several similar SR sequences involving various combinations of recoil and scattering events with different ϕ and θ . The SR energy for a given sequence may be approximated via the application of the E_R and E_{SS} equations using $\phi = 0$ and θ equal to the scattering angle being investigated. SR events are observed sparingly in this work primarily in the form of hydrogen surface recoils.

2.1.5 Cascade Sputtering

When the energy of the incident projectile is transferred to several target atoms through collision cascades, some of which may eventually be directed toward the surface, the result is cascade sputtering. The eventual ejected material may include atoms, molecules, fragments, and clusters, and the energy distributions generally peak at low energies (1 to 20 eV) and tail out to ca. 200 eV. Cascade sputtering events produce many particles that are far too slow to be detected by a channel electron

multiplier, and the flight times are far longer than the experimental TOF window; as a result the only contribution is generally a low-intensity addition to the continuous background (Rabalais 1988).

2.2 Energy Losses

2.2.1 Inelastic Losses

The elastic collision approximation is not perfect; although the majority of energy is lost via elastic collisions, energy is lost through inelastic channels as well. Modes of inelastic energy loss include primarily electronic excitation and ionization of the projectile and/or the target atom. These excitation processes are common for atomic collisions in the kiloelectron-volt energy range, in which the distances of closest approach allow significant overlap of the atomic orbitals of the pair involved in the collision. The details of the modes of inelastic energy loss are given elsewhere (Rabalais 1988), but are beyond the scope of this treatment. Two important considerations that result are (a) that the magnitude of these energy losses are minute compared to the energy transferred kinematically in the collision process, slightly broadening the recoil energy distributions and (b) the resulting E_R distributions are minimized by probing at small recoil angles where possible.

2.2.2 Surface Potential Losses

A planar surface potential affects the trajectory of a recoil atom as it travels through the surface plane, refracting the atom and causing some energy loss. The potential is generally approximated by the heat of sublimation (solid substrate) or by the binding energy of the recoiled atom to the surface (Rabalais 1988). The effect of surface potential energy loss is a decrease in E_R relative to the predicted value given by equation 2.1.4, and surface potential losses are small, of the order of 10 eV.

2.3 Dynamics of Elementary Collisions

2.3.1 Trajectory Calculations

An important facet of the experiment lies in obtaining the probabilities of scattering or recoiling particles into specific angles, i.e. into trajectories that eventually enter the detector in the experiment. To calculate these trajectories the equations of motion for all the particles involved in the collision must be solved. Solution of these equations requires the use of an interatomic potential to quantify the interactions between colliding pairs, and the calculations are generally carried out in the center-of-mass (CM) coordinate system. The calculations produce trajectories for the projectile, DR atom or scattered ion, and any other atoms that may be put into motion during the collision. The probability of particles either scattering or recoiling into a defined solid angle Ω is calculated by varying an impact parameter p in small increments over a wide range and calculation of the resulting trajectories. Further, the probability of scattering or recoiling into an element of solid angle $d\Omega$ is equal to the ratio of the

number of particles entering $d\Omega$ per unit time to the flux density (units of particles/time·area) of the projectiles. This probability is defined as the differential cross section $\sigma(\chi)$, where χ is the CM scattering angle, and has units of area. Detailed treatments of these calculations are provided elsewhere (Lehmann 1977), but these formalisms are beyond the scope of this work, and only the most important results are presented here.

2.3.2 Approximate Formalisms

The differential cross section in the CM frame is given by the expression (Rabalais 1988):

$$\sigma(\chi) = \frac{d\sigma}{d\Omega} = \frac{p(\chi)}{\sin \chi} \left| \frac{dp}{d\chi} \right| \quad 2.3.1$$

Transformation of this expression to the laboratory coordinate system gives

$$\sigma(\theta) = \sigma(\chi) \left[1 + \left(\frac{m_1}{m_2} \right)^2 + 2 \left(\frac{m_1}{m_2} \right) \cos \chi \right]^{\frac{3}{2}} \div \left| 1 + \left(\frac{m_1}{m_2} \right) \cos \chi \right| \quad 2.3.2$$

The direct recoil cross section $\sigma(\phi)$ can be obtained in terms of $\sigma(\chi)$ to be

$$\sigma(\phi) = 4 \sin \left(\frac{\chi}{2} \right) \sigma(\chi) \quad 2.3.3$$

An incident particle that approaches closely is subject to a potential field that deflects it into a new trajectory. The scattering integral, which gives the change in angle for a particle of mass m moving in a central-force field, depends on the

interatomic potential used and the distance of approach, and can be evaluated exactly only for potentials that can be expressed as elementary functions. As an example, a Coulomb potential $V(r) = (C/r)$ yields

$$\chi = \pi - \tan^{-1}\left(2p\frac{E}{C}\right) \quad 2.3.4$$

for the angle of deflection and

$$\sigma(\chi) = \frac{\left(\frac{C}{4E}\right)^2}{\sin^4\left(\frac{\chi}{2}\right)} \quad 2.3.5$$

for the differential cross section. Similarly, for an inverse-square potential ($V = C/r^2$),

$$\chi = \pi \left[1 - \left(1 + \frac{C}{p^2 E} \right)^{-1/2} \right] \quad 2.3.6$$

and

$$\sigma(\chi) = \frac{\pi^2 C}{E} \cdot \frac{\pi - \chi}{\chi^2 (2\pi - \chi)^2} \cdot \frac{1}{\sin \chi} \quad 2.3.7$$

In the small angle approximation, for inverse-power potentials of the type $V = C/r^n$ and $n > 0$, one can obtain an analytical expression:

$$\sigma(\chi) = \frac{1}{n} \left[\frac{C\pi^{1/2}}{E} \cdot \frac{\Gamma\left[\frac{(n+1)}{2}\right]}{\Gamma\left(\frac{n}{2}\right)} \right]^{2/n} \cdot \chi^{-2(1+1/n)} \quad 2.3.8$$

In equations 2.3.4-2.3.6, E represents the energy of relative motion, given by

$$E = E_0 m_2 / (m_1 + m_2) \quad 2.3.9$$

Equation 2.3.5 is called the Rutherford formula, and it provides accurate cross sections in the high energy (ca. > 50 keV) range, where atomic screening is negligible and interactions are closely approximated by Coulomb forces. At lower energies such as ours, the electrons have a screening effect on nuclear charges, reducing the amount of nuclear charge that actually affects the ion trajectories. Commonly, a screened-Coulomb form is used for the interatomic potential. The screening effect is significant in the energy range used, as the electrons effectively reduce the nuclear charge affecting the trajectories. The simplest form of the screened Coulomb potential can be expressed as (Mashkova 1985):

$$V(r) = (Z_1 Z_2 e^2 / r) \exp(-r/a) \quad 2.3.10$$

Here a is the screening length, expressed as

$$a = a_0 (Z_1^{2/3} + Z_2^{2/3})^{-1/2} \quad 2.3.11$$

in terms of a_0 , the Bohr radius ($a_0 = 0.529 \text{ \AA}$).

A simple and reasonably accurate version of the screened Coulomb is the Molière potential, an approximation to the Thomas-Fermi screening function (Mashkova 1985). This approximation allows for an absolute error of within 0.2% for

interatomic distances of $0 < r/a \leq 6$. The form of the Molière potential is (Rabalais 1988):

$$V(r) = (Z_1 Z_2 e^2 / r) \left[0.35 \exp(-0.3r/a) + 0.55 \exp(-1.2r/a) + 0.10 \exp(-6.0r/a) \right] \quad 2.3.12$$

Many different potential functions exist, and the results obtained when using different functions can differ widely from experimental values, and among themselves. An analytical function based on a combination of interatomic potentials and a large number of atom pairs has been developed by Ziegler, Biersack, and Littmark (ZBL). The resulting function, called a Universal Interatomic Potential, has the form (Rabalais 1988):

$$V(r) = (Z_1 Z_2 e^2 / r) \left[0.1818 \exp(-3.2x) + 0.5099 \exp(-0.9423x) + 0.2802 \exp(-0.4028x) + 0.02817 \exp(-0.2016x) \right] \quad 2.3.13$$

In this expression,

$$x = r/a_u \quad \text{and} \quad a_u = (0.8854) \cdot \frac{a_0}{Z_1^{0.23} + Z_2^{0.23}} \quad 2.3.14$$

This universal function provides reasonably good agreement with experimental measurements.

2.4 Examples of Cross Sections

Calculation of scattering and recoil cross sections is done via a simple computer program. A cross section calculation utilizes inputs for the masses of the projectile and target atoms, the desired interaction potential, and a range of impact parameter values. The output includes the θ , σ , and E_s for each scattered incident and ϕ , σ , and E_r for the recoil particle, evaluated at each increment of the impact parameter. Figure 2.4.1 gives examples of recoil cross sections as a function of recoil angle (ϕ) for several inert gas ions interacting with oxygen, calculated using the Molière potential. The $\sigma(\phi)$ increases with ϕ as expected, approaching infinity as $\phi \rightarrow 90^\circ$, the value at which $E_r \rightarrow 0$. Also demonstrated in figure 2.4.1 is that $\sigma(\phi)$ increases as the mass of the projectile increases

($\sigma(\phi)$ for He^+ is over an order of magnitude lower than Kr^+ for $\phi < 50^\circ$).

Another comparison is illustrated in Figure 2.4.2, which shows $\sigma(\phi)$ as a function of ϕ for several target atoms of various m_2 recoiled by 2.5 keV Ar^+ . An interesting feature of this comparison is that while the cross sections generally increase with the target mass, the hydrogen $\sigma(\phi)$ is unexpectedly high. The reason for the anomaly lies in the C/E dependence that arises in the numerical evaluation of the expression for $\sigma(\phi)$ in equation 2.3.8, C being a constant that depends on atomic number, and E , the energy of relative motion given by equation 2.3.9. The only mass dependence is within E , and since the E dependence appears in the denominator of the expression for $\sigma(\phi)$, the mass dependence is roughly proportional to $(m_1 + m_2)/m_2$, leading to the higher value of $\sigma(\phi)$ for a hydrogen target ($m_2 = 1$). TOF-SARS exploits

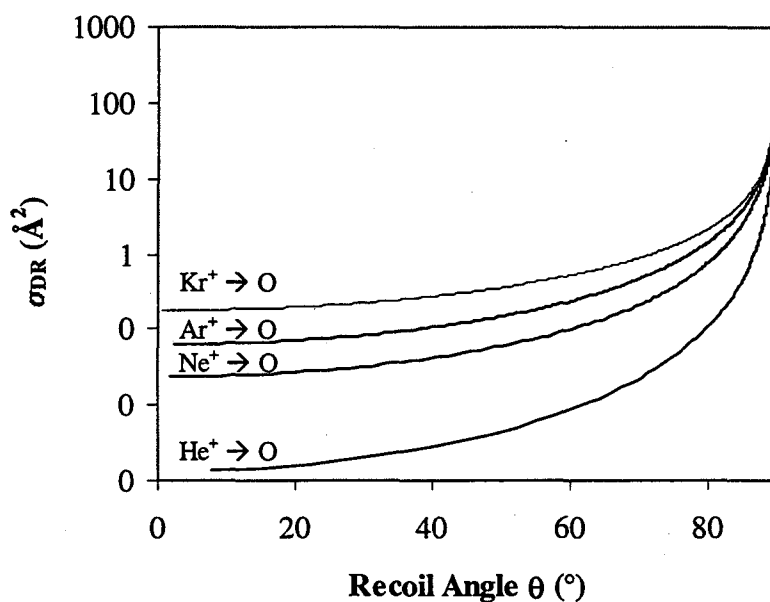


Figure 2.4.1 Recoil cross sections for oxygen as a function of projectile mass.

the large recoil cross section for hydrogen as an advantage, as hydrogen is difficult to detect in many other surface analysis experiments.

2.5 Separation of Scattering and Recoiling Particles

One of the important objectives of the experiment is to separate scattering signals from recoil signals in order to facilitate interpretation of spectra. In general, the flux of scattered particles is several times more intense than the recoil flux (scattering cross sections are larger), and often the weaker DR signal is obscured by the broader, more intense SS and MS peaks. For a TOF experiment such as ours, it is advantageous to have a large separation between the velocities of the scattered and recoiled particles in order to deconvolute spectral signals. As it turns out, we also benefit from the

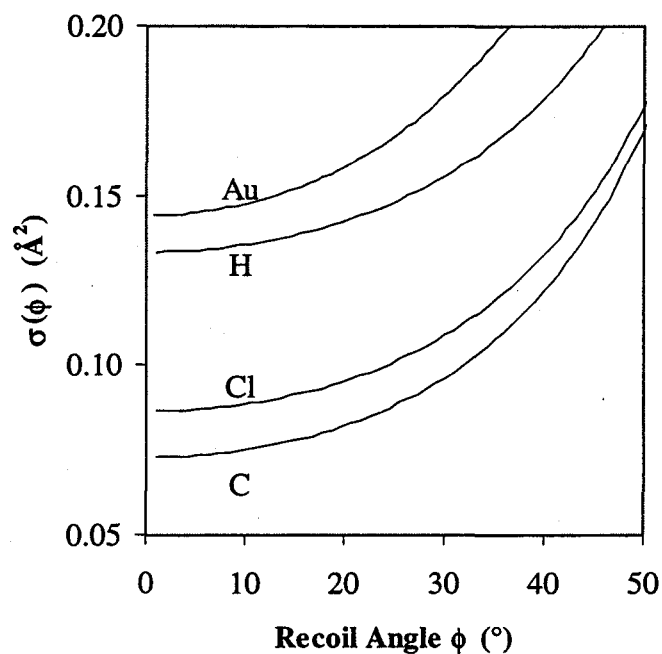


Figure 2.4.2 Recoil cross sections for 2.5 keV Ar^+ recoiling C, Cl, H, and Cu atoms.

generally small masses of target atoms probed- with proper choice of projectile mass, scattering signals are significantly reduced if seen at all. Target atom masses become more important in the scattering events as they increase, making separation of the SS and DR signals more difficult for samples containing heavier atoms such as transition elements, etc. The angles θ and ϕ are both fixed at 45° in our apparatus, but in more sophisticated instruments these parameters may be varied to take advantage of cross section and/or energy considerations in order to separate the recoil and scattering signals as completely as possible. The combined choice of m_1 and ϕ is a compromise- we seek the conditions that give the greatest TOF separation and DR intensities, and lowest SS intensity.

2.6 Trajectory Calculations

Calculation of scattering and recoil trajectories is commonly done for solid samples. The calculation involves solution of the equations of motion for the projectile and for all the target atoms that are set into motion either by primary or secondary energy transfer. Computer simulations are capable of accurately predicting the trajectories of incident and secondary particles and give insight into the nature of the surface structure. Particularly important are those involving *shadow cones*, in which the primary ions are deflected away from a region through interaction with a target, and *blocking cones*, in which a recoiled particle is excluded from certain trajectories as it exits the surface. The upper diagram gives an example of the shadow cone formed by parallel incident particles interacting with a surface atom; the blocking cone scenario is given in (b) of the figure, in which a recoiled atom encounters another surface atom. Trajectory calculations are crucial in understanding the long-range anisotropic surface structure of crystalline samples, particularly when imaging of scattered and recoiled particles is involved. However, where liquid surfaces are concerned, trajectory calculations are somewhat more

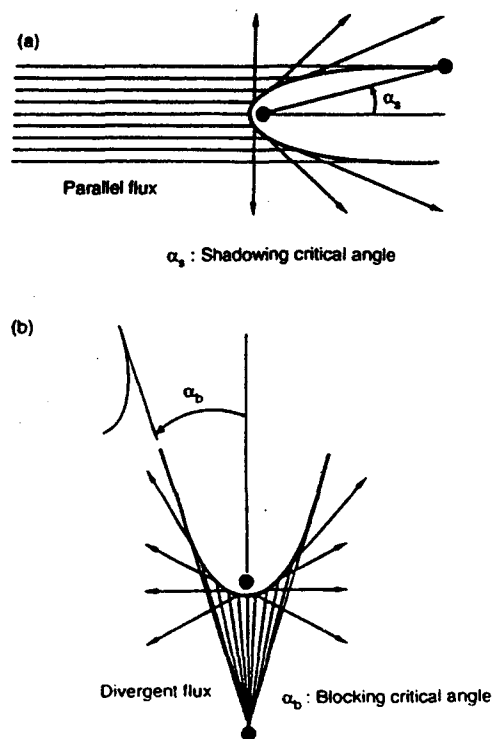


Figure 2.6.1 a. Example of a shadow cone simulation. b. Blocking cone simulation. Source: "Low Energy Ion-Surface Interactions", J. W. Rabalais, ed. Copyright John Wiley & Sons Limited. Reproduced with permission.

particle is excluded from certain trajectories as it exits the surface. The upper diagram gives an example of the shadow cone formed by parallel incident particles interacting with a surface atom; the blocking cone scenario is given in (b) of the figure, in which a recoiled atom encounters another surface atom. Trajectory calculations are crucial in understanding the long-range anisotropic surface structure of crystalline samples, particularly when imaging of scattered and recoiled particles is involved. However, where liquid surfaces are concerned, trajectory calculations are somewhat more

difficult to undertake and may not be as informative as for solids. Blocking and shadowing effects can be considered on a more localized basis, for example between neighboring atoms within a surface molecule, as a semi-quantitative approach.

3. Details of the TOF-SARS Liquid Surfaces Experiment

3.1 Vacuum System

3.1.1 Introduction

The vacuum system serves as the 'life-support system' for the entire experiment, and without it no other part of the apparatus can function. A diagram of the layout of the entire experimental apparatus is given by Figure 3.1.1. To provide further detail regarding the vacuum, Figure 3.1.2 illustrates the scheme of the vacuum pumping equipment. A powered table and rack provide the mechanical base and electrical wiring for the apparatus. The sample chamber, a multiple-CF port stainless steel vessel, had been custom manufactured for another experiment but fortunately had several of the correct dimensions for our needs. The additional required fittings were primarily purchased from commercial suppliers; some were modified after purchase, and a few were specially machined in the department.

Diffusion pumps provide the majority of the pumping for the apparatus. We chose to use diffusion pumps (DPs) as the main pumps in this system for several reasons, including their high pumping speeds, relatively low cost, ruggedness, durability, and availability. Diffusion pumps are somewhat prone to contamination of the system due to backstreaming of the fluid used. This problem was addressed in part by installing traps and/or baffles to minimize the amount of vapor that reaches the chamber. In the region of the detector, which must be kept cleaner, a turbomolecular

Figure 3.1.1 Schematic overview of the TOF-SARS apparatus.

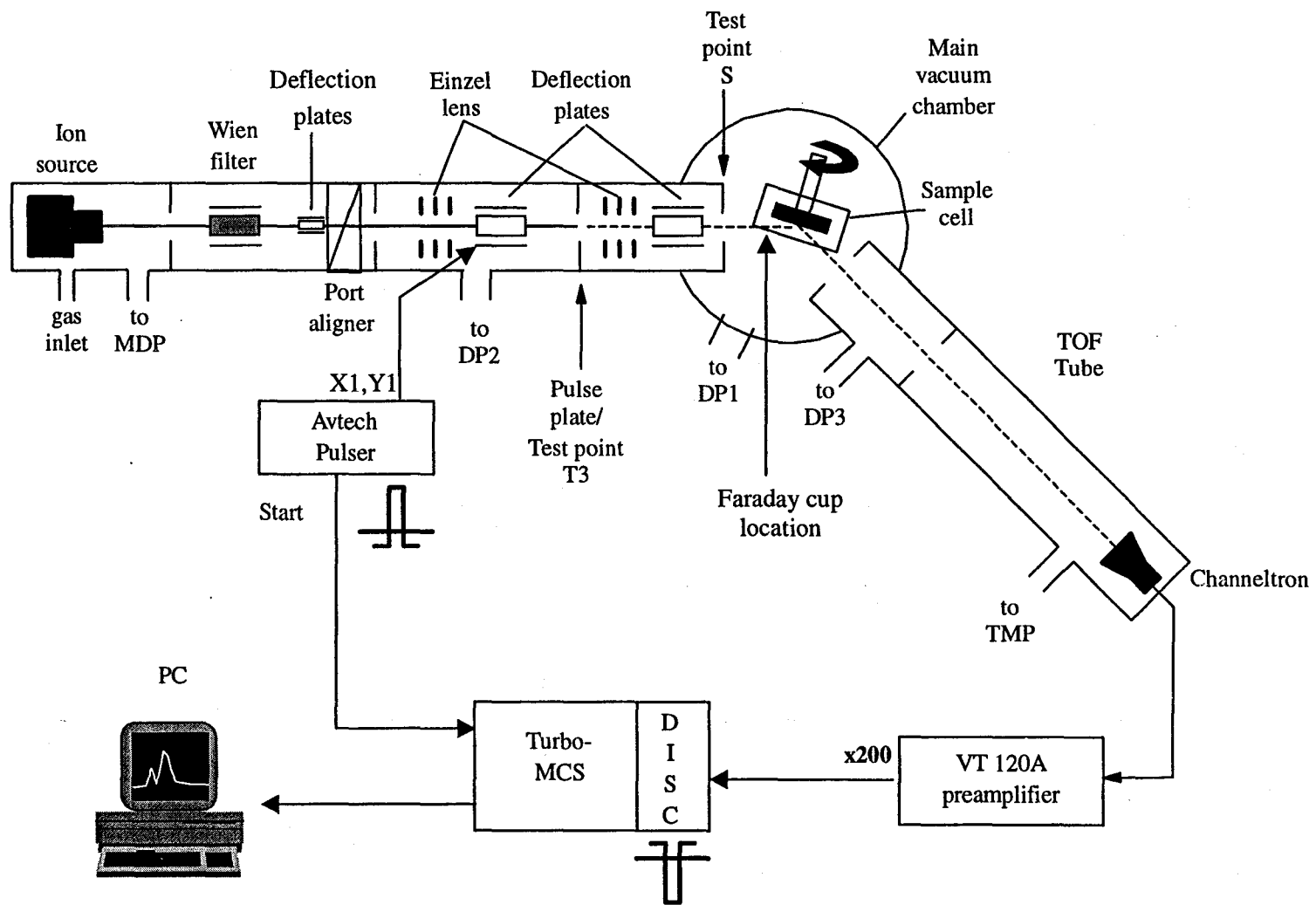


Figure 3.1.1

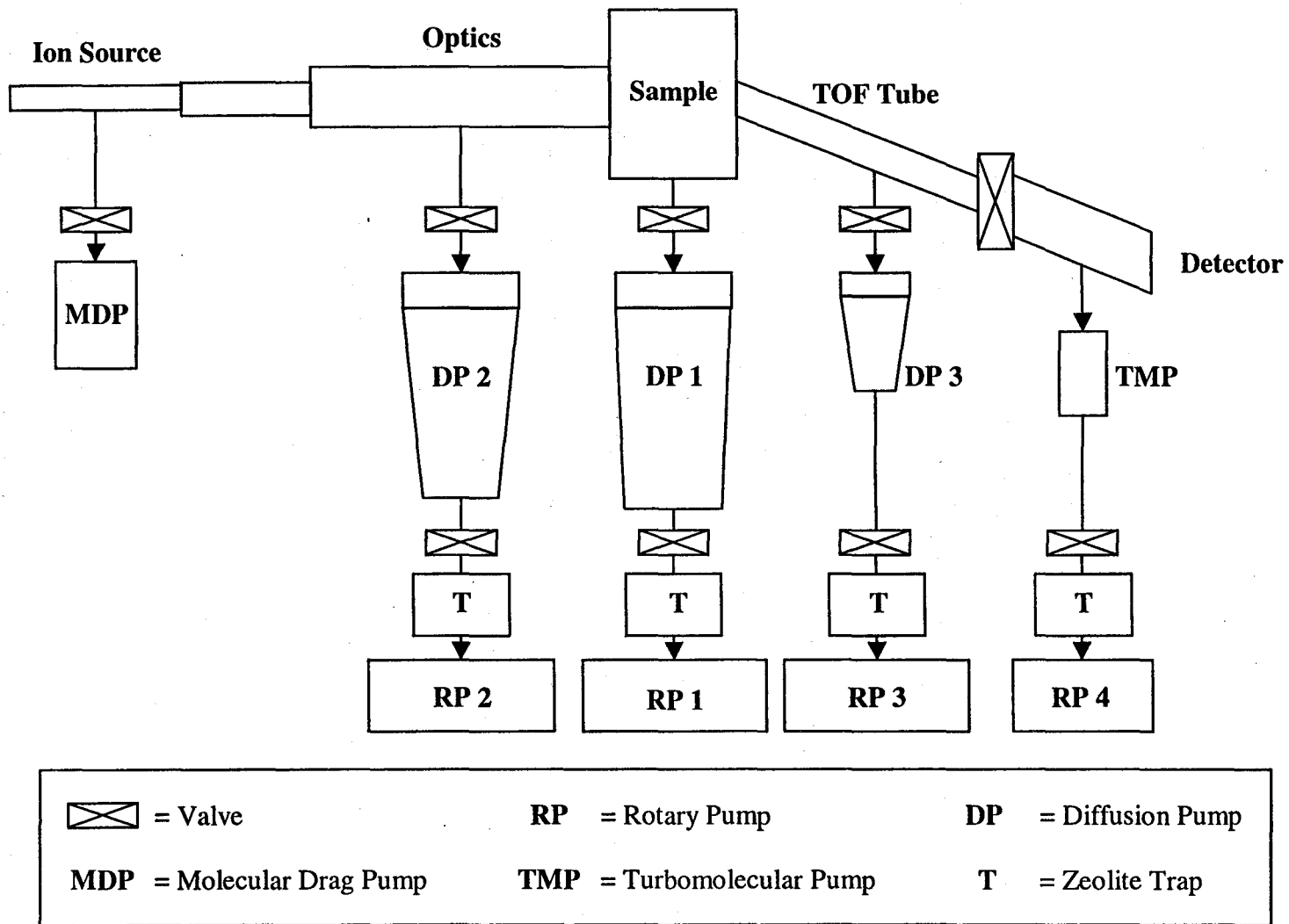


Fig. 3.1.2 Schematic diagram of the spectrometer vacuum system.

pump (TMP) was chosen to provide a better vacuum. The TMP has the advantage of running free of fluid and hence cleaner than diffusion pumps, but has the disadvantages of lower pumping speeds and higher cost. The ion source is evacuated by a molecular drag pump (MDP), a clean, oil-free pumping unit that operates reliably in the range of 10^{-6} torr.

Each of the aforementioned vacuum pumps requires a roughing, or backing pump. The pressure against which the pumps work must be reduced significantly from atmosphere for the pumps to operate efficiently. A pressure gradient between the inlet and outlet that is too large will greatly reduce the efficiency of the pump, and in some cases can cause physical damage to the pump. The mechanical pumps chosen for backing the DPs and TMP are all Alcatel rotary direct-drive pumps. They operate in the range of 10 mTorr and have several advantages over other pumps that are capable of obtaining this vacuum. One of the best arguments for using direct-drive pumps is their anti-suckback mechanism, which helps prevent oil from the backing pump from being sucked into the DP or TMP that it backs in the case of a power failure. In this way, gross contamination of the system and HV pumps is avoided. Additionally, direct drive pumps run much quieter than similar belt-drive pumps and require less maintenance.

3.1.2 Physical Resources

The main resources required for the operation of the vacuum system are a source of electrical power for each pump and/or controller and a source of cooling water for the diffusion pumps. The pumps require either 110 VAC or 220 VAC, in the

case of the largest DP which pumps on the main sample chamber. The circuitry of the room was modified by OSU physical plant services to include wall outlets capable of handling the current and voltage requirements for operation of the system. A total of nearly 7000 W of continuous power is needed in order to operate all of the vacuum pumps and the cooling system associated with them. The majority of the power was routed into the table and through to the rack, which greatly reduced the amount of external wiring.

The cooling water requirements for proper operation of the DPs were satisfied via two sources. Building cooling water provides the main source for the largest diffusion pump. A faucet located near the floor of the lab and on the same wall where the electrical outlets are was chosen and a 5/8" copper tubing line was installed to run water through the pump. The water drains to the nearest floor receptacle. A LCD-strip thermometer was applied to the tubing near the faucet in order to monitor the water temperature, as we were concerned that the water would get too warm during the summer months. Experience has shown that this water has never been outside the manufacturer-specified operating range of the pumps.

The two smaller DPs are cooled through the use of a Neslab CoolFlow model CFT-75 recirculating chiller. This device uses a closed loop to continuously provide cooling water and the temperature may be set via a thermostat control. Nominally 20°C is the chosen setting according to manufacturer specifications for the DPs. A large quantity of heat is removed from the system by the Coolflow chiller and is dispensed into the room housing the apparatus. This heat is consequently removed by air-conditioning, as it is essential to maintain a reasonable temperature in the lab, both

for the operation of the pumps and for the consistent performance of electronic components that control the experimental systems.

Finally, a vent is required to carry away exhaust from the vacuum system. Each of the mechanical roughing pump outlets is connected via plastic tubing to a 3 in. diameter PVC pipe which acts as an exhaust duct. This pipe is connected to a flexible reinforced vinyl hose and the exhaust is then removed in the same way as fumes would be from a fume hood.

3.1.3 Roughing Vacuum

Since the high vacuum pumps are not capable of operating against atmospheric pressure, the interior of the system must be partially evacuated, or rough pumped, to reduce the pressure to a suitable value. This nominal roughing pressure is on the order of 10^{-2} Torr, and is achieved via the aforementioned direct-drive mechanical pumps. The fittings used for the roughing lines are the Quick-Connect type, which make a vacuum seal through use of a rubber O-ring that is compressed between steel flanges by a special clamp. The roughing lines, or forelines, must pass from the mechanical pumps, which sit on the floor, to convenient connections on the system; this distance is a few feet in most cases. Reinforced PVC hose is the best choice for these lines as it can be cut to any length, allows some flexion, and is less expensive than rigid materials such as stainless steel. The lines are generally kept as short as possible and the largest convenient diameter of tubing is used in order to allow maximum pumping speed. In some cases the throughput is limited by small diameter tubing as part of the roughing lines or shutoff valves, but this is avoided wherever possible.

The roughing pumps serve a dual purpose: they must act to rough out the chamber and also to back the high vacuum pumps. For this reason the roughing lines are split into two branches, isolated from each other and from the vacuum chamber by shutoff valves, which allow the chamber to be roughed before starting the HV pumps and then isolated during HV pumping. In the case of the TMP which pumps on the detector, the roughing of the chamber takes place through the TMP itself. The four roughing pumps will be referred to from here forward as RP1, RP2, RP3, and RP4, corresponding respectively to the main chamber (1), ion optics chamber (2), time-of-flight tube (3), and detector chamber (4). Table 3.1 below compares some of the specifications of the roughing pumps.

Table 3.1 Rough Pump Specifications

	Model	Displacement (cfm)	Base Pressure (mTorr)	Fluid (l)
RP1	Alcatel 2033	27	25	3.6
RP2	Alcatel 2012A	11	20	0.8
RP3	Alcatel 2008A	7	5	1.0
RP4	Alcatel 2002A	1.4	10	0.35

Each of the four roughing lines incorporates a molecular sieve trap situated directly above the mechanical pump. The zeolite material of the sieve acts to prevent volatiles from the mechanical pump fluid from backstreaming into the diffusion pump. The sieve material additionally adsorbs water vapor, which over time results in decreased efficiency of the mechanical pumps. Desorption of volatiles from the sieve is achieved through baking of the traps for several hours using cartridge heaters inserted into a cylindrical hole through the center of each trap. The foreline traps are

constructed of a stainless steel body and a mesh compartment which contains the sieve; the traps may be opened for replacement of the adsorbent or for other cleaning. During baking, a considerable amount of water vapor exits the trap, and must be given consideration as the baking is normally done *in situ*. Water vapor leaving the trap and passing through the mechanical pump is compressed to the point of condensation during normal operation of the pump; this water remains in the pump fluid and lowers the ultimate pressure that the pump can achieve. This problem is mitigated through use of the gas ballast, a feature of the mechanical pumps, which allows air into the compression chamber via a leak-valve mechanism, and the additional air helps prevent compression of water vapor to liquid.

The outlet of each mechanical pump is oriented vertically, out of the top of the pump. This proved, in the case of the largest pump that roughs the main sample chamber, to be a poor design. Water vapor condenses in the exhaust line over time, and the condensate drips back into the pump, causing considerable corrosion of the pump's iron exhaust fitting. The extent of the corrosion not only reduces the diameter of the outlet, but also has caused rust particles to fall into the pump fluid. This is also undesirable, as solid particles in the fluid cause undue wear on the moving parts, decreasing the life of the pump. To avoid this corrosion as much as possible, the exhaust line leading directly from the pump has been wrapped with a resistive heating tape and warmed slightly to reduce condensation where water would drip back into the pump.

3.1.4 High Vacuum

As mentioned above, the main vacuum chamber is evacuated by a combination of molecular drag, diffusion, and turbomolecular pumps. The DP's handle the majority of the evacuation as they offer high pumping speeds, whereas the TMP and MDP are generally cleaner during operation, since they are essentially oil-free, requiring only lubrication for moving parts. Table 3.2 below illustrates some specifications of the high vacuum pumps.

Table 3.2 High/UHV Vacuum Pump Specifications

	Model	Speed (l/s)	Base Pressure (Torr)	Heater (W)
DP 1	Varian VHS-6	2400	10^{-9}	2200
DP 2	Varian VHS-4	1200	10^{-9}	1450
DP 3	Varian HS-2	285	10^{-8}	450
MDP	Hovac Dri-2	8	10^{-6}	N/A
TMP	BalzersTPH040	30	10^{-8}	N/A

3.1.4.1 Diffusion Pumps

Diffusion pumps handle about 80% of the duty of evacuating the high vacuum system. In addition to the high pumping speeds, high throughput, and low ultimate pressure, DPs are quite reliable and dependable over long periods of time at relatively low cost. They have no moving parts that can fail; additionally, they can withstand harsh chemical vapors and are virtually noise-free. Diffusion pumps have several disadvantages to consider as well. They must be kept within a suitable operating environment, as mentioned above- cooling water and roughing vacuum are critical to their normal operation. The fluid involved is expensive and susceptible to oxidation or

“cracking” if exposed to air while hot, and a breach of vacuum will cause distribution of the fluid over all internal surfaces, requiring lengthy and costly cleaning procedures. The pump fluid must be continuously boiled which requires considerable energy- that is, the running costs of the pump higher than most others. Backstreaming, that is, the migration of oil vapor from the pump into the chamber, occurs under normal operating conditions. Liquid N₂- cooled traps and/or baffles can be installed to minimize backstreaming, again increasing the cost of operation. Backstreaming is a major disadvantage of DPs in UHV applications, and indeed poses a problem for our experiment as well.

3.1.4.2 Molecular Drag Pump

The molecular drag pump in the present system has two purposes: it acts to differentially pump on the ion source as well as to evacuate the noble gas inlet line when the gas is changed. A gate valve in the roughing line isolates the main vacuum chamber from the pump as well as the gas line. It is capable of achieving base pressures in the low 10⁻⁶ Torr range at the exit of the gun. It should be noted that the Hovac DRI-2 MDP is packaged as a unit with a small rotary vane backing pump and the unit includes a set of safety features to protect the MDP itself from overpressure damage. The electronics of the unit sense when the forepressure is too great, and cuts off the power to the drag pump in that case. Other advantages of the MDP unit include clean, oil-free operation, and that it can be started at atmospheric pressure by a simple pushbutton switch. The main disadvantage is its low pumping speed.

3.1.4.3 Turbomolecular Pump

The TMP involves a series of rotor discs that are stacked and rotate at high speed on an axle, and the bottom of the rotors impart directed momentum to pumped gases in order to remove them. It should be noted that the TMP is more applicable to very clean ultra-high vacuum (UHV) systems; we approach the UHV regime (10^{-8} Torr) in the detector region only when experiments are not in progress; the normal pressure during experiments is in the 10^{-6} Torr range. The choice of the TMP was made primarily for its fluid-free operation, eliminating any backstreamed oil that could harm the detector; this factor outweighs the higher cost of the pump.

3.1.5 Differential Pumping

In order to maintain cleanliness, the main chamber, ion source, and detector regions of the instrument are physically isolated from each other as much as possible. This is done in order to limit contamination of the ion source and detector by evaporated sample material. A method referred to as differential pumping, not to be confused with the term diffusion pump, greatly facilitates this cleanliness. Differential pumping involves the separation of two adjacent volumes of the vacuum chamber by a small diameter aperture; a high-vacuum pump such as a diffusion pump simultaneously pumps each of the regions. The aperture limits the flow of gaseous molecules from one region to the other, and a rather large pressure gradient between the two regions can be achieved. For our purposes, large pressure gradients are not necessary as much as reduction of transfer of material between the regions; a factor of 10 to 100 is typical.

A very important consideration is the interaction of incident ions with molecules in the vapor phase as opposed to the liquid phase. For several reasons, interaction of ions and atoms that are part of the scattering/recoil process are undesirable. Those molecules in the vapor phase would have no preferred orientation; also their varying locations in space would give rise to a broader distribution of flight times in the spectra, adding to the background and decreasing resolution. Another concern is whether or not we can transport enough ions onto the liquid surface and scattered/recoiled particles away to the detector. Should the sample be very volatile, enough molecules would exist in the vapor phase at any given time that very few energetic particles would traverse through the sample chamber. In order to reduce vapor-phase interaction, samples are chosen with low vapor pressure as a key characteristic. Additionally, differential pumping is employed to minimize the amount of time that the particles spend in the sample region of the instrument. Again, a small aperture allows the focused beam to pass into the chamber while keeping the ion optics region "clean", relatively isolated from the sample chamber. The so-called entrance aperture, through which the ions enter the sample interaction chamber, is situated as close as conveniently possible to the liquid sample holder. This is intended to limit the distance that incident ions must pass through the vapor phase before impinging on the surface. This remedy should also apply to the particles exiting the interaction chamber, with a similar "exit aperture".

Our system, however, is handicapped as a result of the original manufacture of the chamber, and differential pumping is not an option for the exit from the main chamber. The flaw in question involves the vacuum port that connects the time-of-

flight tube to the sample chamber. Either the center of the port is not coplanar with the center of the entrance port or the entrance/exit flanges are not perfectly normal to the vertical axis of the chamber. Regardless, the end result is that scattered and recoiled particles cannot reach the detector when an exit aperture is put in place to for the purpose of differential pumping. The short-term solution to this problem is to exclude the exit aperture from the apparatus, thus sacrificing the differential pumping capability and the minimization of interaction with vapor. The good side of this is that the detector is still kept clean via the pneumatic gate valve that is included in the time-of-flight line. The gate valve is kept closed at all times other than during experiments, and the turbo pump maintains pressures in the mid 10^{-8} Torr range when the valve is closed. Ideally, the chamber construction would have the flanges normal to the vertical axis of the chamber. Future considerations include a new design for the chamber, involving a smaller volume as well as variation of the scattering/recoil angle.

3.1.6 Pressure Measurement

The measurement of the pressure of gas in the vacuum system is critical to the success of the experiment, and it poses significant challenges. Monitoring the pressure at various locations throughout the system is important for several reasons, including:

- Protection against overpressure for the diffusion and turbo pumps
- Maintenance of particle transport in the sample interaction chamber
- Cleanliness of the detector, increasing its lifetime
- Optimal ion gun operation and protection of filaments
- General maintenance of the vacuum pumps, both roughing and HV

- Leak checking

We employ three methods for the purpose of pressure measurement: thermocouple (TC) gauges for roughing vacuum, and both ionization gauges and a quadrupole mass spectrometer in the HV/UHV range. It should be noted that none of these methods provide absolute pressure measurement, in which the gauge is independent of the type of gas present and gives an “absolute” value of the total pressure. The gauges used here inherently respond somewhat differently to various gases, due to variances in thermodynamic properties such as ionization potential. We are satisfied with a close estimation of the total pressure as monitored by the TC and ionization gauges; this allows for the protection of system components and for suitable experimental conditions. The mass spectrometer is capable of qualitative and semi-quantitative partial pressure analysis of the gases present, but not absolute measurement. The mass spectrometer is a recent addition to the instrument, originally intended for use during helium leak-checking, but has proven additionally useful for monitoring the partial pressure of the noble gas used to generate ions.

3.1.6.1 Thermocouple Gauges

The thermocouple gauge operates in a range suitable for roughing vacuum requirements, from about $1000\text{-}10^{-3}$ Torr. The package is a fairly rugged and convenient steel tube that connects to the system via 1/8” National pipe thread (NPT). Teflon tape is always used to ensure a positive vacuum seal. The tube, depending on the type, has four or more pins on the head, and mates to a suitable controller via a

matching cable, made in our lab to meet the necessary specifications. The controller provides power and converts the return signal to a pressure in Torr or microns of mercury. The gauge tubes are susceptible to contamination by adsorbed materials including pump oil and liquid sample vapor, causing a false high pressure reading. This contamination is generally removed through cleaning with an organic solvent, e.g. several rinses with ethanol or acetone.

The TC gauge controller contains a millivoltmeter that converts the returning signal to a pressure reading. The thermocouple junction is very well understood, and the controller is calibrated to display total pressures based on the TC voltage produced. Again, the pressure reading is dependent on the type of gas present and it is non-linear over this range of pressures, but is sufficiently accurate in the operating range of $\sim 10^{-2}$ Torr. Many TC gauge controllers offer the convenience of a rear-panel output voltage that is proportional to the pressure reading. The controllers used most often in our apparatus are Varian Sen-Torr units, which provide a 0 to -20 mV output. This output is used in the DP control safety circuit discussed below.

3.1.6.2 Ionization Gauges

For HV to UHV total pressure measurements, Bayard-Alpert type ionization gauges are used. These gauges operate over a broad pressure range, typically $\sim 10^{-4}$ to 10^{-11} Torr, a broader range than many other gauges can offer. In exchange for this type of sensitivity, however, the gauge heads sacrifice some durability. A main component of the gauge is a high-temperature filament, which can react with ambient

gases- especially backstreamed diffusion pump fluid. Also, the physical makeup of the gauge is a fragile structure of fine wires, susceptible to damage by contact with other objects. The gauge heads are available in two packages, a glass envelope which is connected external to the vacuum chamber or a "nude" gauge which is just that- the gauge is mounted on a flange and is not enclosed. Both types are generally mounted on 2-3/4" Conflat flanges, and the electrical feedthroughs are made via metal-to-glass seals, whereas metal-to-ceramic seals are used in the nude type.

3.1.7 Diffusion Pump Control Unit

The diffusion pump control unit was specially designed and constructed for use in our experimental setupⁱ, customized for the specifications and requirements of the three diffusion pumps. The controller includes a detailed protection circuit (illustrated in Figures 3.1.3 and 3.1.4) to prevent operation of the diffusion pumps under undesirable conditions. Figure 3.1.3 shows the main power connections to the chassis of the box, while Figure 3.1.4 gives a detailed picture of the sensing and control related to overpressure shutoff. The circumstances to be avoided include overheating as result of insufficient cooling water; operation against overpressure, caused by failure of one or more roughing pumps, and exposure of the hot fluid to air, causing major contamination of the pump and the system as a whole. Another objective of the protection circuit involves power failures- the DPs should turn off automatically in case of a power outage, and should not immediately turn on again when power is restored. The controller has a manual reset button that must be depressed to reactivate the pumps after power failures. This elaborate circuit may be overkill for the day-to-

Figure 3.1.3 Schematic of the diffusion pump control circuit. Off = power interrupt; Temp = temperature switch; Flow = flow switch; On = set power switch; OD (1, 2, 3) = diffusion pump override; OV (1, 2, 3) = quenching valve override; PL (1, 2, 3) = pressure control lamp; SV (1, 2, 3) = solenoid valve; RE (1, 2, 3, 4) = SRE-202D mechanical relay. Original design, construction, and drawings by M. Tassotto. Reproduced with permission.

Figure 3.1.4 Detail of the sensing circuit for the diffusion pump control unit. TC (1, 2, 3) = thermocouple gauge output voltage; R1 = 10M Ω ; R2 = 1 M Ω ; T (1, 2, 3) = 2N2222A transistor; RE (5, 6, 7) = SRE-202D mechanical relay. Original design, construction, and drawings by M. Tassotto. Reproduced with permission.

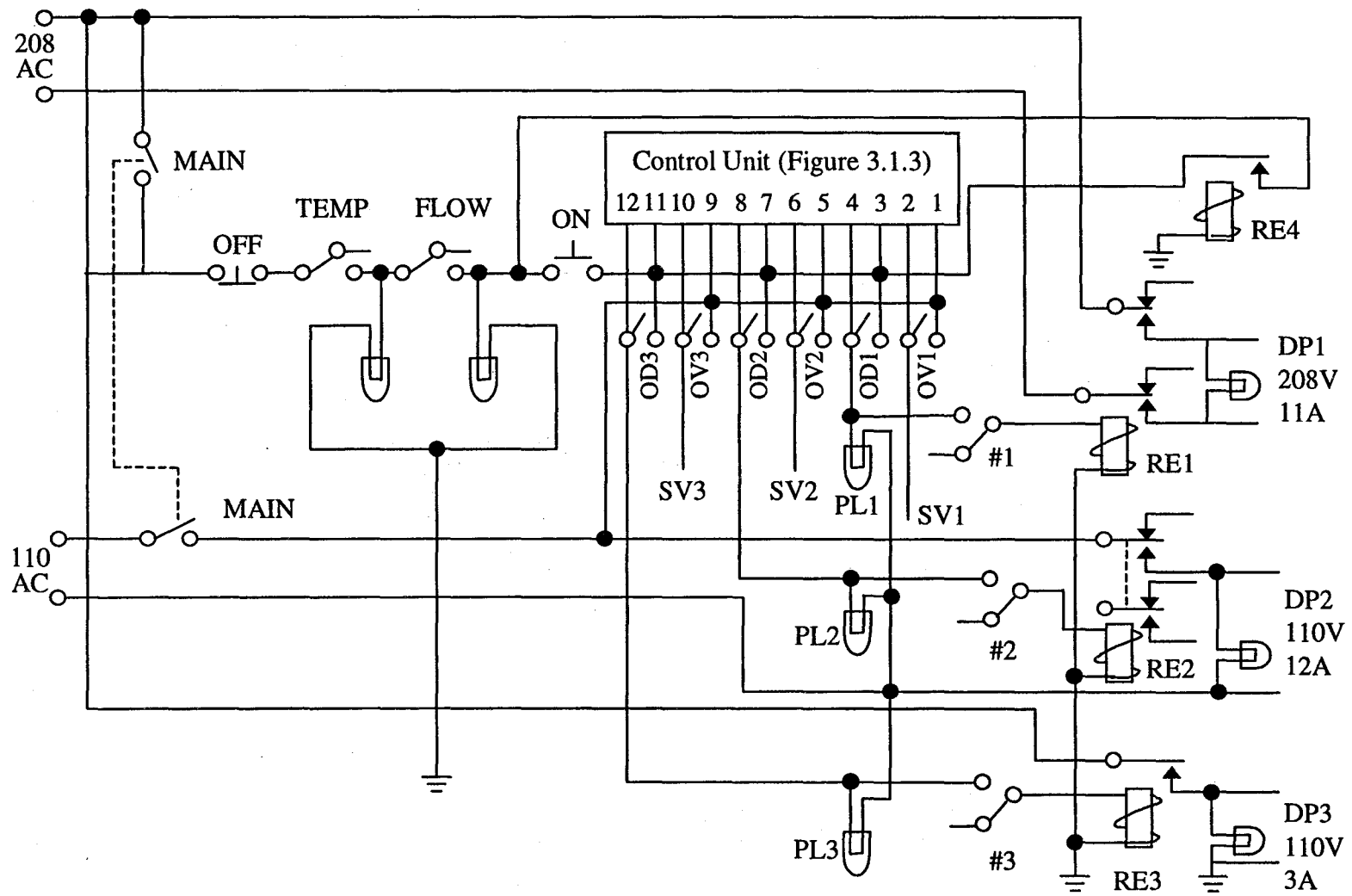


Figure 3.1.3

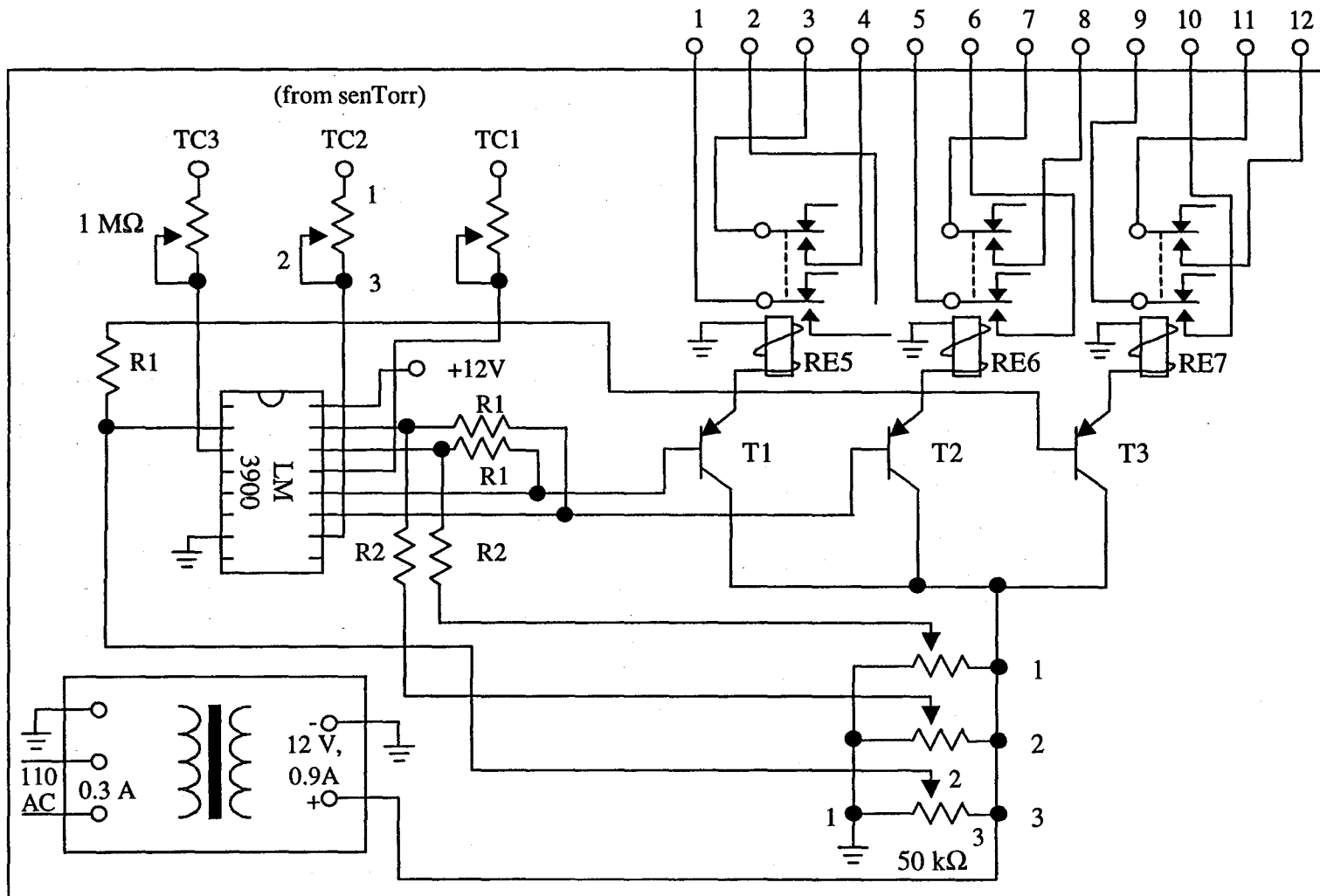


Figure 3.1.4

day operation of the system, but it has prevented any catastrophic failures of the pumps due to overheating or air exposure, saving countless hours of repair time.

3.2 Ion Source

Paramount to the success of the experiment is a reliable source of ions. The source in use is a hot cathode electron impact ion gun, typical for use with noble gases. The three guns we have used are all research-quality sputtering guns, capable of producing total ion currents of ~1

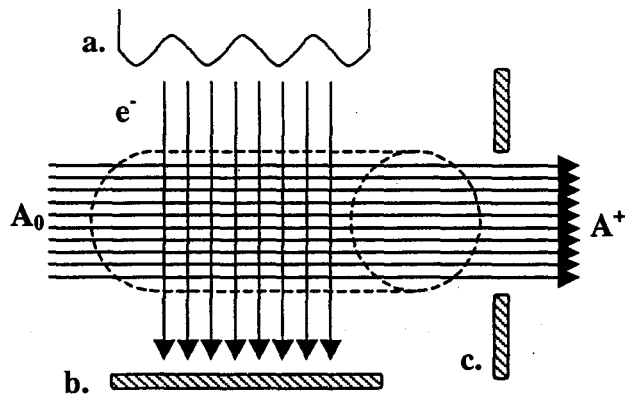


Figure 3.2.1 Electron impact ion source.

μA and beam energies of up to 3 kiloelectron volts. Although the designs of the guns vary, the basic principle is identical. A schematic diagram of an electron impact ion source is illustrated in Figure 3.2.1. In this scheme, the electrons are generated by a resistively heated filament (a.) and accelerated toward a biased grid (b.) to some ionizing kinetic energy, typically 70 eV. Some of the inert gas atoms (A_0) are struck by electrons and become ionized to A^+ ions. An extractor (c.) that is biased negatively relative to the ions accelerates the ions toward the gun exit, which leave through an aperture of a few mm in diameter. Additional electrostatic elements focus and/or deflect the ions as they travel through the gun.

The first ion gun used was a 3M MiniBeam I unit, and it provided service for the first three years of the project. Its several shortcomings included instabilities in the power supply and electrical shorts between the high-voltage elements of the optics within the gun. The second gun used, albeit for a brief time, was a Phi sputtering gun, model 04-191. This gun was a component previously used for surface preparation in an X-ray photoelectron spectroscope in our lab, and two different 04-191 guns were available for use. Of the two guns and compatible power supplies, one gun was in permanently disabled condition, and one power supply was not repairable, leaving one controller and one gun in working condition. When the working 04-191 gun was installed in the system, it showed some promise for future use, providing a reasonable total ion current. However, it was difficult to characterize the beam characteristics *in situ*, partly because the dimensions of our system were developed with the 3M Minibeam gun in mind, and the useful operating gun-target distance of the 04-191 was seemingly substantially different. During this lengthy characterization process the third and present ion gun arrived for use. The latest version of the gun is a specially constructed model, made by OCI Vacuum Microengineering. For a reasonable price, the OCI IG70 has proven to be quite reliable and capable for over one year, barring a modification that had to be performed by the manufacturer after we received the gun. The IG70 produces a total current of up to 1 μA , depending on the gas used.

3.3 Ion Optics

3.3.1 Introduction

The ion optics for this experiment serve the several purposes: to direct the charged particles toward the target surface, to select only the ions that are of the correct mass and energy, and to create pulses of these ions in order to collect time-of-flight information. A series of stainless steel plates and cylinders, serving as electrostatic deflectors and lenses respectively, are in place in the vacuum system between the gun and the sample. Figure 3.3.1a illustrates the construction of the optical components.

The main components of the optics are as follows:

- X-Y deflectors, which direct ions toward the target as they exit the gun;
- Wien filter, which helps ensure a monochromatic ion beam;
- “Lens 1”, actually a set of X-Y deflectors and an electrostatic lens in one unit. The main purpose of the deflectors here is to provide ion pulses.
- “Lens 2”, an identical X-Y deflector/lens unit to lens 1. The Lens 2 optics reoptimize the beam after the pulses are formed, but just before they strike the target.

It is crucial to the experiment that all of the optics work together; failure of any component will either prevent ion pulses from forming or not allow them to reach the target. We have been fortunate in that no major failures have occurred since the assembly of the optics, and modifications have been made only to the end of the ion gun arm closest to the gun.

To provide independently variable voltages to the discrete elements of the optics, we designed and constructed a custom supply. The Wien filter as well as all the components of Lens 1 and Lens 2 are powered by the supply at a substantially reduced cost compared to the purchase of commercially available high voltage supplies. This custom supply is discussed in greater detail in the following section.

3.3.1 Wien Filter

For our experiment, it is essential to ensure that the ions reaching the target are monochromatic, that is, having the same (known) kinetic energy. It is also important to select the proper mass and charge ions and allow only those to probe the surface. For example, an Ar^{2+} ion will acquire twice the kinetic energy of an Ar^+ in the same accelerating field, and the velocities will be different by a factor of $2^{-1/2}$. We wish to selectively allow the +1 ion of the chosen gas (Ar, Ne, or He) and remove from the beam both multiply charged ions and neutrals. Higher-charge state ions are deflected out of the beam through the use of a Wien filter (WF), which employs crossed electric and magnetic fields to separate ions according to their ratios of mass to charge (M/E). Neutrals are excluded by means of a slight off-axis bend in the line; ions are deflected back into the proper axis, but neutrals are unaffected by the deflecting field and continue to travel away from the experimental axis. The Wien filter construction is shown in figure 3.3.1b. The filter consists of an applied electric field between two horizontal plates spaced 6.5 mm apart, 49 mm in length and 28 mm wide, as well as a magnetic field of 1200 Gauss provided by Varian Alnico permanent magnets. The regions preceding and following the WF plates is shielded by 4.5-mm tubes of a foil

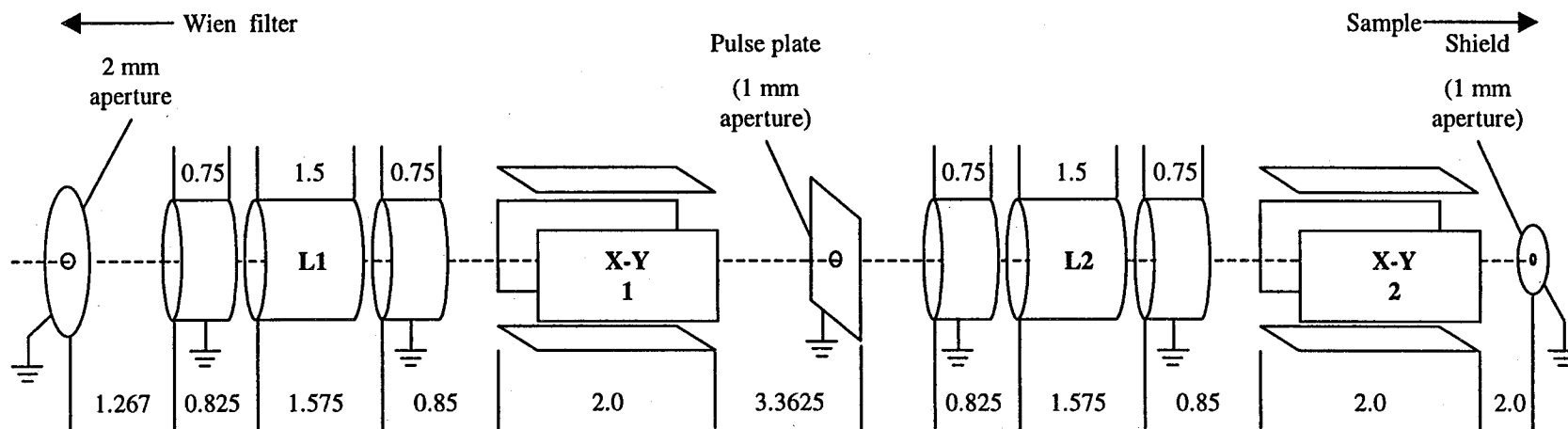
material (Co-Netic®, Magnetic Shield Corp.) designed to minimize stray magnetic fields. The purpose of the Co-Netic shielding tubes is to ensure that ions experience the magnetic field only while they are moving between the plates. This should in principle improve the total beam current at the target and help to better define the beam.

The principle of the Wien filter involves a counteraction of crossed fields. The magnet is placed such that the field (B-field) is horizontal and normal to the beam axis, with north to south oriented from right to left, looking from the gun toward the target. This exerts an upward vertical force on the ions as they pass through the filter, and the trajectories of ions having different M/E will be affected to different extents. The overall effect of the B-field is that all charged particles in the beam are “bent” upward out of the original axis, and different ions are separated from one another, e.g. Ne^{2+} will be bent further upward than Ne^+ . The gas used for ion production is very pure (>99.99%) but trace amounts of atmospheric gases will always remain in vacuum; the WF helps to remove any ionized molecules of O_2 , N_2 , CO_2 , etc. that may be present in the beam as well. Once the “raw” ion beam has been separated into its various M/E components, the electric field (E-field) acts to deflect the desired component downward, back into the beam axis. With a fixed B-field, the E-field can be varied over a range of DC voltages to select the correct M/E ion. The voltage required ranges from ca. +200 VDC for 3 keV Ar^+ ions to ca. +800 VDC for He^+ .

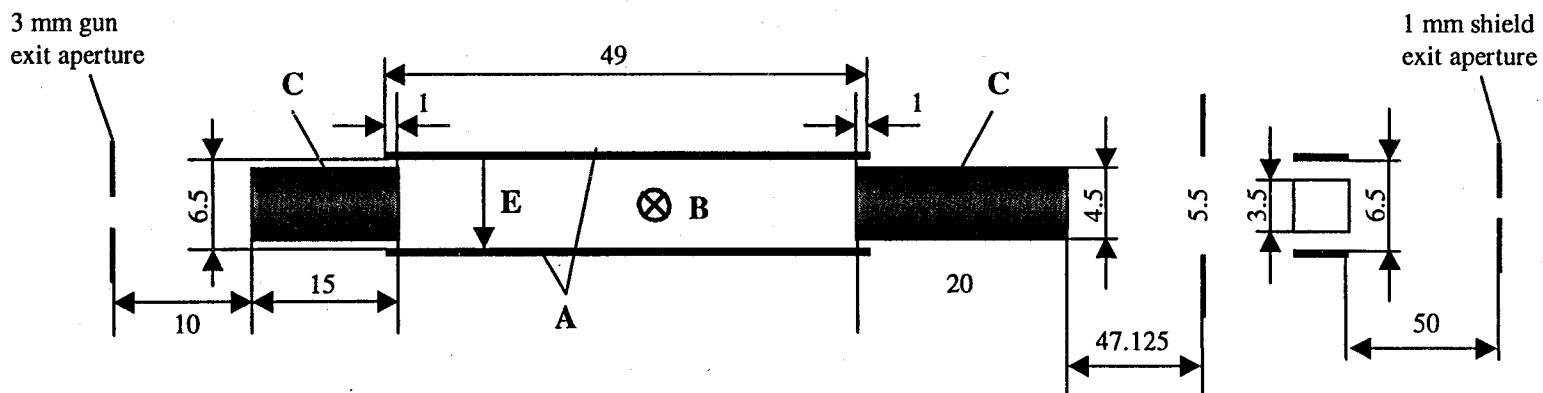
The Wien filter is physically situated inside a 2.75” conflat tee fitting that adds 5 inches in length to the ion gun arm. The electrical feedthrough for the filter also acts as a mechanical support- the entire assembly is suspended vertically from the

Figure 3.3.1 a. Expanded side view of the electrostatic lensing and deflection elements. All dimensions in inches unless otherwise noted. Additional dimensions: L1, L2 OD = 0.75 in., ID = 0.675 in.; deflection plates are 2.0x0.75x0.10 in. thick.

b. Side view of the Wien filter apparatus. A. Deflection plates are 49x28x1 mm thick. B. Horizontal 1200 Gauss magnetic field ζ to beam direction. C. Co-Netic® magnetic shielding tubes. E. Direction of electrical field. Original design, construction, and drawings by M. Tassotto. Reproduced with permission.



a. Lens and deflection elements



b. Wien filter

Figure 3.3.1

feedthrough pin by a thin steel rod attached via a large barrel connector. The positive (upper) plate is isolated from the grounded (lower) plate by shielded ceramic rods. A copper wire connects the lower plate to the chassis of the entire instrument, ensuring a good ground connection.

3.3.2 X-Y Deflectors

Both the 3M gun and the PHI gun are equipped with X-Y deflection plates near the exit of the gun. These deflectors help to account for minor misalignment in the mounting of the gun, and are also of great importance in removing neutrals from the ion beam; this will be discussed below. The X-Y deflectors both here and further downstream are supplied with a DC voltage necessary to steer the beam toward the target. In most cases, where the beam velocity is primarily toward the target, the necessary potential is very low, on the order of $\nabla 20$ V. In cases where a larger-angle deflection is required, the potential needed also increases, but usually is within a range of $\nabla 100$ V. The potential required depends on several factors, including the mass and velocity of the ion, the length of the plate to which the deflecting potential is applied, and the spacing between the plates. The latter is important because the deflection plates are always in parallel pairs, and one of the plates in each pair is held at ground while a potential is applied to the opposite plate. The field that the ion experiences differs, then, as the spacing between the parallel plates changes.

The X-Y deflectors that have been added to the ion optics for the OCI gun are taken from the exit of the 3M gun, as it is no longer used. The geometry of these previously existing deflectors required no significant modification other than a

mounting bracket. The beam raster control of the 3M supply is used in conjunction with the deflector plates, providing voltages from $\sqrt{220}$ VDC. The plates themselves are $\frac{1}{4}$ " long by $\frac{3}{16}$ " wide and are located immediately following the Wien filter, and essentially in the center of the positioner described below. As the deflectors are in the middle of the positioner, they remain very close to the beam axis independent of the angular position of the gun.

The electrical feedthrough for the X-Y deflectors is part of a four-way cross fitting that originally included the gas inlet for the 3M Minibeam gun. This piece was reused as a matter of convenience- the four-pin electrical feedthrough matches the cable pinout of the raster control and no cable modification was needed. The gas inlet port, a Cajon-type fitting, is blanked off.

3.3.3 Tilt Positioner

Another important component of the optics, albeit passive in nature, is the tilt positioner. A Huntington VF-175 angular tilt positioner allows the gun to be positioned off-axis relative to the intended beam axis, from zero to ten degrees away. Ideally the off-axis positioning of the gun will force neutral particles that may lie within the beam to miss the initial aperture that defines the beam. The desired charged particles are steered toward the aperture via the aforementioned deflection plates.

The angular tilt positioner is necessarily connected to the preceding 2.75" conflat tee (containing the Wien filter) by a union that allows two "tapped" flanges to mate, while adding a minimum length to the apparatus. Tapped flanges are analogous to female pipe fittings, and the connecting bolts can only enter the flange from one

side. Normal (untapped, or “through”) flanges can be bolted from either side, but the tilt positioner logistically requires tapped holes on either end. A Kimball Physics fitting called a close coupler allows this connection, and each adds 0.75 inches to the total length, a small sacrifice when the conventional method of connection would add two inches. The close coupler immediately following the tilt positioner is mounted on a 2.75”-6.00” reducing flange that contains the Lens 1 assembly.

3.3.4 Lens One Assembly

The lens one (L1) assembly, as mentioned above, contains both an Einzel electrostatic lens and a set of X-Y deflection plates that act as the pulsing mechanism. The entire assembly hangs from the other side of the 6.00” reducing flange mentioned above. The hardware used for these optics, Kimball Physics eV Parts[®], is designed and manufactured solely for the purpose of fabricating electron and ion optics. Precision-engineered, standardized components fit together within an interlocking system that assembles stainless steel cylinders and plates into lenses and deflectors with insulating ceramic rods. The entire assembly is held rigidly in place with tension springs and snap rings.

The Einzel lens consists of three stainless steel tubes in succession, concentric and parallel to the beam. The middle tube 1.5” long, is held at a large positive potential, forcing the cations in the beam toward the center of the tube, and the tubes before and after are held at ground. The three tubes are closely spaced so that the grounded tubes effectively shield the ions in the beam from stray electric fields

emanating from the positive lens element. The typical DC voltage applied to the lens is on the order of 2.5 kilovolts.

The X-Y deflection plates here are much larger than the previous deflectors, each being 2.0 inches long and 0.75 inches wide. As a result, the voltage required is quite low, typically 0-20 VDC. The deflector plates are designated as X1+ (right), X1- (left), Y1+ (top) and Y1- (bottom). Electrical potential is applied to only one of the parallel plates in each +/- pair at a time, and the plate is selected by means of a single-pole selector switch on the front panel of the power supply. When a potential is applied to one plate, the opposite parallel plate is grounded.

The Lens 1 X-Y deflectors serve a special additional purpose, that of pulsing the ion beam. Up to this point in the beam line, the beam is continuous; since the time-of-flight experiment requires a distinct "time zero" or start time, the beam must be chopped into small packets, or pulses of ions. This is accomplished most effectively by optimizing the beam current, then deflecting the beam vertically so that it misses a small aperture (pulsing aperture), and finally applying short voltage pulses to sweep the beam across the aperture, thus allowing short pulses of ions through and toward the target. The scheme of the pulsing involves two voltage pulses, one in the vertical direction and one in the horizontal; the result is a cyclic path that begins and ends directly above or below the pulsing aperture. In practice, the beam is first optimized to obtain the maximum continuous beam current, next the pulsing scheme is set, and finally the beam is reoptimized to gain the maximum pulsed beam current at the target. The pulsing aperture is a 1 mm diameter hole centered on a stainless plate located 3.36

inches after the pulse plates. The pulsing aperture plate is mounted on the near side of a double sided 6.00 inch ConFlat flange.

3.3.5 Lens Two Assembly

The lens two assembly is identical in construction and capability to the Lens 1 assembly. It contains an electrostatic lens element for further focusing of the beam after the pulsing takes place, and X-Y deflection plates to steer the beam through the final aperture (previously referred to as the entrance aperture) prior to interaction with the target. It is mounted on the opposite side of the 6.00-inch double-sided flange mentioned above. The Lens 2 optics do not serve any purpose related to pulsing the beam, but are rather to better optimize the beam current at the target in both the continuous beam and pulsed modes.

3.4 Optics Power Supply

3.4.1 Introduction

The ion optics each require a stable source of power, and each must be varied independently of the others. To this end, we have constructed a custom power supply that provides DC voltages to the elements of Lens 1, Lens 2, and the Wien filter. A custom supply solves the problems associated with finding commercially available supplies that match the necessary specifications, and do so at a substantially lower cost. The home-constructed supply provides a total of nine outputs, variable from 0-5

Figure 3.4.1 Ion optics power supply circuit. A. LM 317T voltage regulator; B. AHV 5 kV module; C. AHV 1 kV module; R1. 247 Ω ; R2. 10 M Ω ; R3. 100 k Ω ; C1. 0.1 μ F; P1. 5 k Ω potentiometer; P2. 1 M Ω potentiometer; M. DP 654 panel meter. Circuit development and original drawing by J. Swirczynski. Reproduced with permission.

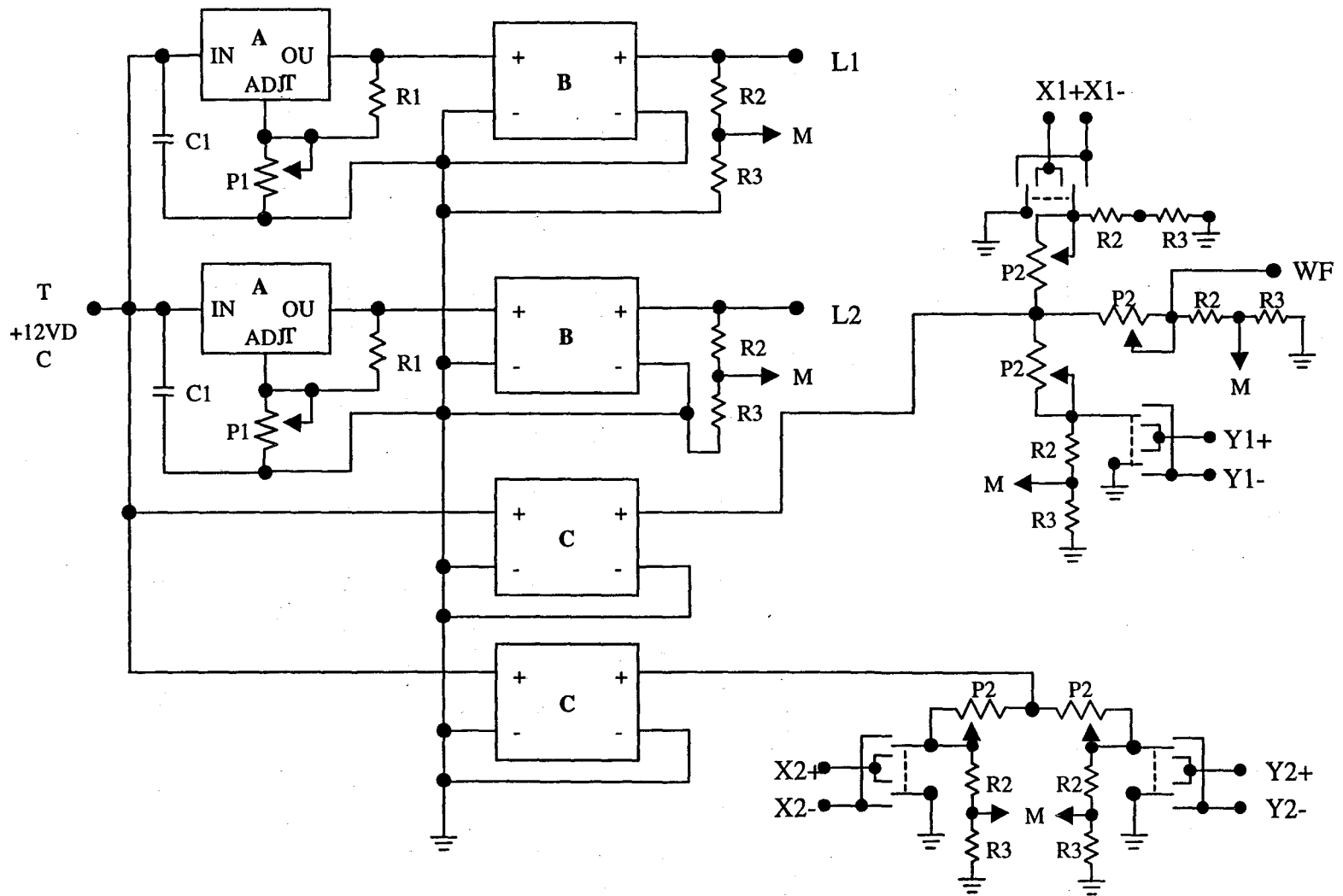


Figure 3.4.1

kilovolts for the lenses, 0-500 volts for the Wien filter, and 0- ± 200 volts for each X-Y deflection plate. Multi-output commercial supplies can cost in excess of \$1000 per output, and nine outputs would not normally be available in a single unit. We have conveniently placed all nine outputs into a single rack-mounted chassis for a materials cost of less than \$1000, a very reasonable expense. Figure 3.4.1 details the circuit used for the Einzel lens elements and the deflector plate voltages respectively.

3.4.2 Principle of Operation

The ion optics power supply consists of three solid-state high voltage (HV) modules that convert a low-voltage (to +12 VDC) input to HV. The output of each module is very nearly linearly proportional to the input. The supply employs 5 kV modules for the electrostatic lenses, and 1 kV modules for the Wien filter and deflection plates. These solid state modules provide output voltages that are proportional to the input. The output of each 5kV module is regulated by varying the input by means of a 5 k Ω potentiometer that divides the +12 V supply. In the case of the 1 kV modules that power the deflectors and Wien filter, the module input voltage is held constant, providing a fixed output voltage that is then adjusted by potentiometers incorporated into voltage dividers. The post-adjustment output voltages are appropriately divided (by 100 or 1000) and sent to a digital panel meter via a multi-position selector switch so that each of the applied potentials may be independently monitored.

3.5 Ion Current Measurement

3.5.1 Introduction

Measurement of the ion beam current at several points along the beam line, up to and including the target region, is of utmost importance to the success of the experiment. The beam must be optimized and focused onto the target for the maximum pulsed current and consequent enhancement of the signal-to-noise (S/N) ratio. The greater the S/N ratio, the shorter the acquisition time for each TOF spectrum; this only improves the quality of the data. The beam current fluctuates over time, generally dropping slightly over a period of hours, likely due to slight power supply instabilities along the optics line. It stands to reason, then, that faster data acquisition will allow easier comparisons between spectra, as a result of the reduced differences in beam current from spectrum to spectrum.

3.5.2 Electrometers

The current is measured by means of digital electrometers that can operate in the range of picoamps (pA) to microamps (μ A). Electrometers used for the purpose are Keithley models 480 and 614, the latter also functional as an electrometer or voltmeter if desired. Connections to the various current measurement test points are made via copper wires connected by barrel connectors, and BNC vacuum feedthroughs allow external connection to the ammeters. In order to facilitate switching between test points, a small box consisting of four BNC inputs and a single output has been implemented. Four toggle switches, one for each input, allow selection of any of the

test points individually or simultaneously, and each test point is grounded when not selected. When summed together all test points give a relative measure of the total beam current.

3.5.3 Test Points

The test points in the beam line necessarily cannot obstruct the beam's path; an alternative would be to employ one or more Faraday cups that could be moved in and out of the path via motion feedthroughs. This option would add length to the path, undesirable as the dimensions of the ion optics would require some modification; additional cost would also be incurred. Instead, we have opted to employ some of the existing elements of the optics in addition to a Faraday cup near the target. If an aperture plate in the beam path is electrically isolated, it can be monitored for whatever ion current it intercepts. Stainless steel lead wires spot-welded to the plates that act as the initial aperture following the Wien filter and the pulse aperture allow monitoring of ion current at those points. Additionally, the last aperture the ions pass through before entering the sample chamber is isolated and a copper lead wire is attached for the purpose of current measurement. This point will be referred to as the shield as it is part of the cylindrical differential pumping hardware and it essentially "shields" the Lens 2 apparatus from the chamber, keeping it relatively. The shield is a stainless disc with a 1mm aperture, and it is electrically isolated via a nylon washer.

A movable Faraday cup is employed to measure ion current immediately in front of the target area. The main principle of the cup is to "trap" any electrons that might be ejected and escape, which leads to a false high current reading in the case of

positively charged impinging particles. The cup is ideally a small-diameter cylinder whose length is several times the diameter, and the thickness of the walls is kept to a minimum. The smaller the diameter, the greater the sensitivity in locating and focusing the ion beam; the deeper the cup, the fewer escaping electrons.

The Faraday cup design has undergone several revisions throughout the course of this work, with the latest design being most effective and easy to use. Initially, the cup was approximately $\frac{1}{4}$ " in diameter and a similar depth, and it was mounted on the face of the liquid sample cell. This location proved inconvenient, as each current measurement required that the entire cell be translated in three dimensions to align the cup with the beam, a non-trivial operation. The design currently incorporates a linear motion translator independent of the sample cell, allowing *in situ* current measurement without moving the cell. The translator is mounted on a 2.75" conflat flange that is horizontally coplanar with the beam axis. This is extremely convenient and has enhanced the quality of the experiment, as the beam current can be easily measured at any time before, during, or after a spectrum or set of spectra without disturbing the sample cell position. The Faraday cup design itself has been modified to enhance sensitivity and accuracy. The length is increased to greater than $\frac{1}{2}$ ", and the diameter is reduced to $\frac{1}{8}$ ".

3.6 Sample Delivery

3.6.1 Sample Cell

3.6.1.1 Introduction

Experiments in vacuum that involve liquid samples pose unusual challenges to the design of the instrument. It is obvious that the problem of evaporation must be mitigated as much as possible; loss of sample is a primary concern, but the evaporated material that remains in the vapor phase can severely hinder the experiment. The remedy for evaporation, in our case, is minimizing the area exposed to vacuum, and maintaining “cool” sample temperatures of ca. 20° C when possible. The design of the cell keeps the majority of the exposed area contained within the reservoir compartment, away from the vacuum. An area of a few square centimeters is left exposed.

Another challenge that must be overcome is the variation of the incident beam angle. It is obvious that liquid surfaces naturally assume a horizontal surface due to gravity; if a pool of sample were used, with a horizontal surface, the entire vacuum assembly housing the ion gun and optics would have to move vertically to alter the incident angle. This would prove quite difficult considering that the vacuum connections are rigid by design, as well as the proposition of realignment and optimization of the beam with each change of the incident angle. It is more reasonable to rotate the target surface about an axis normal to the incident beam axis, and this can be done via a rotary motion manipulator, provided that the sample surface is vertical. The sample cell then must include a vertical liquid surface in its design.

solution is to continuously create a new surface in some way. The design we have adopted is a rotating wheel that is partially submersed in a reservoir of the liquid sample. Fortunately for us, many low-vapor pressure liquids are highly viscous and have no trouble wetting a metal substrate such as the stainless steel disc used, making the vertical surface relatively easy to produce.

The sample cell is based closely on a design originally developed for use in a molecular beam scattering (MBS) study of low-vapor pressure liquids. Figure 3.6.1 represents a view of the front face of the liquid sample cell. In the MBS study, viscous, highly hydrogen-bonded samples such as glycerol ($C_3H_8O_3$) were probed by means of a low-energy molecular beam at steep incident angles. The cell design used was replicated almost exactly here, but in practice it was soon found that modifications were necessary in order to perform our studies. The most significant design improvement involved widening the opening of the cell to a slot in order to allow incident and exit trajectories at the glancing incident angles necessary for this experiment; the MBS experiment employed steeper angles and thus a smaller interaction area.

3.6.1 Design and Operation

The wheel is made of stainless steel and rotates at ca. 0.5 Hz, creating a fresh, macroscopically flat liquid surface. An electric motor (120 VAC) provides the power for rotating the drive shaft, and the motor is part of the cell but isolated from the sample. In vacuum, overheating of the motor is a concern as normal radiative cooling is not efficient. To remove the generated heat, an MGW-Lauda RC3 recirculating

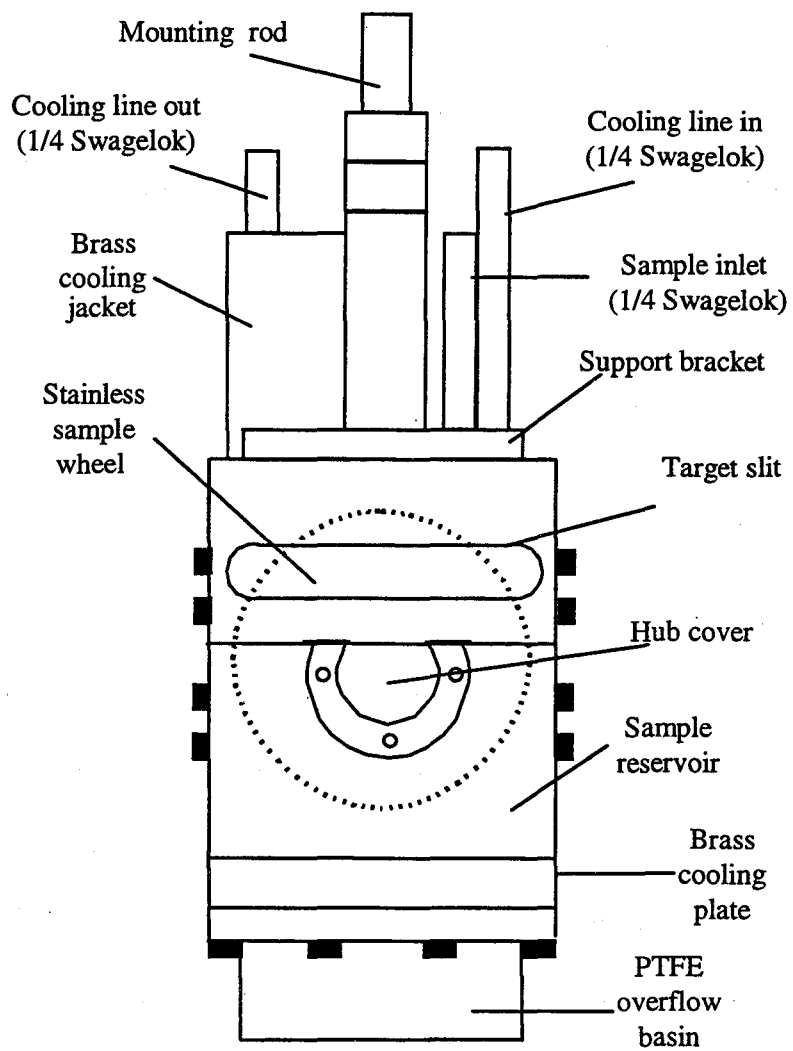


Figure 3.6.1 Frontal view of liquid sample cell Approximate scale 1.125:1.

heater/chiller passes water through a brass cooling jacket that surrounds the motor casing. The cell originally was designed to supply additional sample *in vacuo* as evaporation depleted the supply, but it was found that if the evaporation is significant enough to cause a rapid drop in the volume of liquid contained, the experiment cannot be performed satisfactorily due to pumping speed limitations. Additionally, the original liquid level sensing device involved electro-optical sensors in contact with the sample in which the wetted parts were actually soluble in many of our samples and had to be abandoned. At present, a visual confirmation that liquid is present on the wheel is performed during each experiment and the liquid is replaced as needed. A system involving an optical interruption mechanism has been designed but not yet implemented; the difference in the new scheme is that the electronic parts would not be wetted by the sample.

The cell is divided horizontally just above the wheel axle and the top and bottom separate for cleaning and filling. The bottom compartment consists of the sample reservoir, PTFE overflow basin, and a brass heat-exchanging plate that regulates the sample temperature. The liquid film thickness is limited to ~0.2 mm by a steel scraping blade adjusted to the appropriate spacing from the wheel. A semi-exploded view of the bottom half of the cell, including the drive shaft, wheel, scraper, and reservoir is depicted in Figure 3.6.2. The upper half of the cell contains the gear that drives the wheel axle, the electric motor and its cooling jacket (external to the sample reservoir), and a horizontal slot that allows the beam to interact with the surface of the wheel. The original design placed the liquid level sensors in the top compartment, but the current version uses a blank plate in their place. The entire cell is

mounted on an inverted U-shaped bracket that attaches to the support rod of the rotary manipulator.

3.6.2 Manipulator and Feedthroughs

The sample cell requires a number of feedthrough connections for liquids, power, and signals. In order for the cell to be easily removed from the chamber, the connections are self-contained in a single unit atop the chamber. The manipulator and feedthroughs are mounted on a 6.25" long extender that has two additional 2.75" conflat ports, one horizontal and one at 45° above horizontal. The liquid feedthrough has three connections- two for the motor/sample cooling water supply and return, and the third is presently blanked off as it is not needed. The liquid feedthrough is mounted on the 45° port while the horizontal port is reserved for an electric feedthrough used primarily for thermocouple connections.

The manipulator itself (Vacuum Generators) has rotary, X-Y-Z translation, and tilt modes of motion. For our purposes, the translation and tilt are set to give proper positioning and alignment of the target area in three dimensions, and they are left alone under normal circumstances. The rotary motion is the only one of the three that is used regularly, for variation of the incident beam angle. The manipulator has six electrically isolated posts available as electric feedthroughs but three of them are permanently occupied by the motor connections. The additional connections are available for thermocouples and have previously been used for beam current measurement and for resistive heating of solid samples.

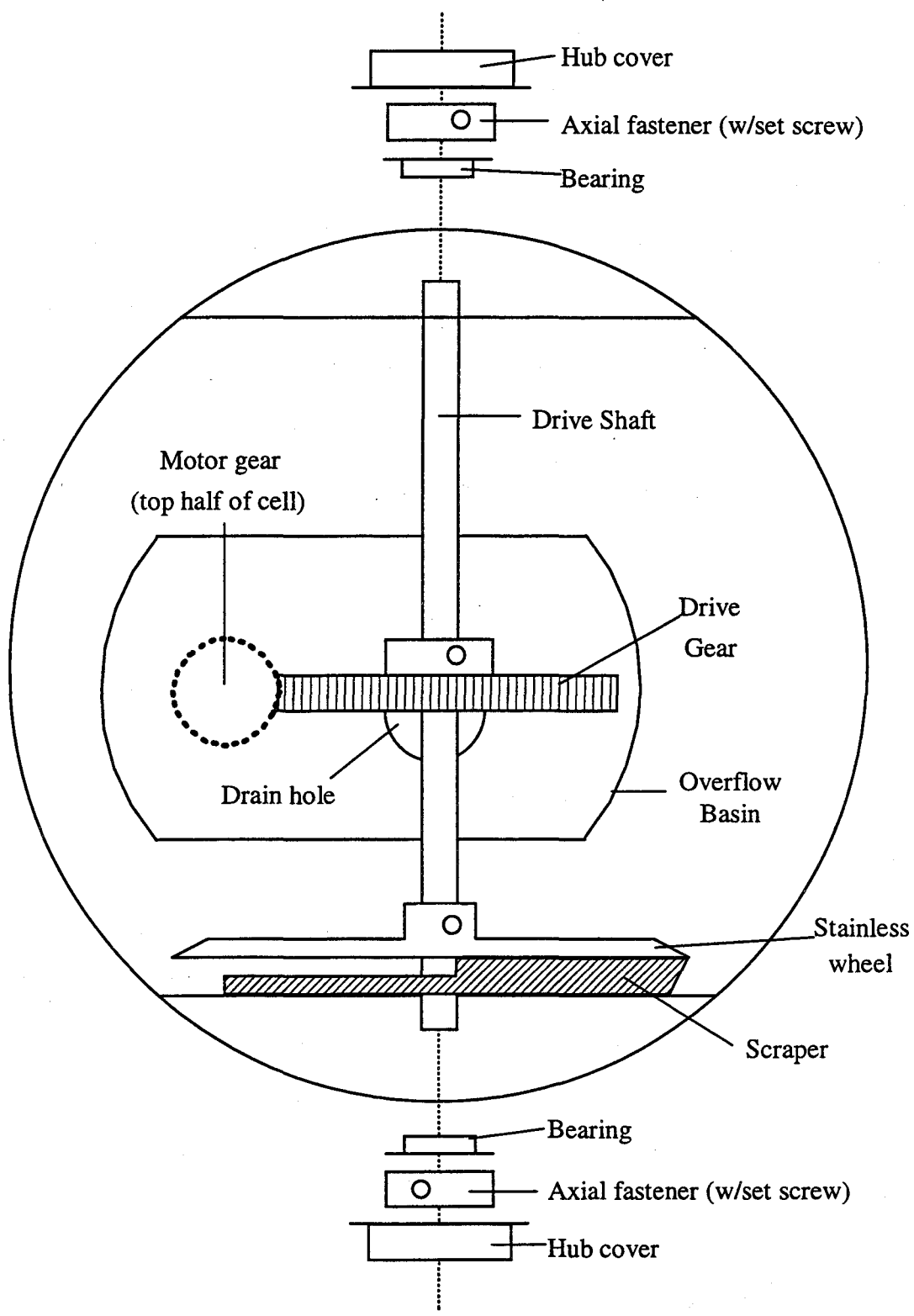


Figure 3.6.2 Overhead semi-exploded view of the bottom half of the liquid sample cell.

3.7 Detection

The detection of particles that leave the surface is extremely important to the success of the experiment. A sensitive channeltron electron multiplier (Detector Technologies 407-EIC) is effective for detection of both neutrals and ions that have some minimum velocity, on the order of $10^5 \text{ cm}\cdot\text{sec}^{-1}$. The multiplier has a gain of about 10^7 , that is, for each particle that causes a cascade of secondary electrons, the charge pulse generated is approximately 10^7 electrons. A fast preamplifier (EG&G Ortec VT120A) receives this output and converts it to a fast voltage pulse which is in turn received by a multichannel scaler (EG&G Ortec Turbo-MCS), which in turn registers and stores the events. The MCS is synchronized to start counting with each pulse of ions, and generates a histogram of counts (scatter/recoil events detected) versus time-of-flight of the particles. The MCS is interfaced to a personal computer that stores the histogram for later analysis using manufacturer-provided software.

The channeltron (Detector Technologies 407EIC) is a continuous dynode multiplier, which implies that the electrons cascade continuously along its entire length, rather than in distinct stages as most photomultiplier tubes operate. A low-work function metallic oxide film on a glass substrate provides the necessary amplification of electrons when sufficient potential difference is applied. The detector must be biased such that the back end is positive relative to the front end (cone). This can be accomplished in at least two ways: with the front end grounded, the back can be held at positive HV; alternatively the front can be held at a negative bias and the back grounded. We have chosen to ground the front end and bias the back positively so that any incoming ions are not subjected to an electric field. Figure 3.7.1 schematically

illustrates the connections to the channeltron. The dashed line represents a grounded steel enclosure that provides shielding from stray radiation. Particles of sufficient velocity are detected as they slam into the conical face of the tube, generating a cascade of electrons.

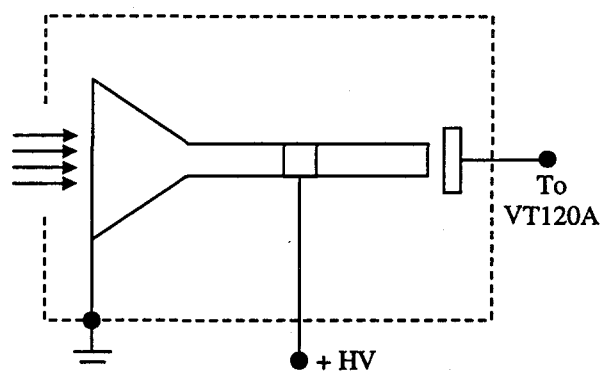


Figure 3.7.1 Schematic diagram of channeltron operation.

The electron packets corresponding to each detected event are accelerated through the detector tube, collected by a conductive plate (collector) as they exit, and sent to the fast preamplifier via a BNC electrical feedthrough. The MCS unit is designed to work with an Ortec VT-120A fast preamp, and it has a built-in discriminator that sets a threshold voltage for signals from the preamp allowing rejection of “dark current”. We have determined experimentally that a discriminator setting of ca. -1.6 V gives the best signal while excluding noise.

3.8 Procedure

3.8.1 Sample Introduction

When a new sample is to be introduced, the sample cell must be removed, disassembled, and thoroughly cleaned to avoid contamination of the new sample. After filling with new sample, the scraper blade is adjusted to an appropriate distance from the wheel, so that the film is uniform, and of convenient thickness. In practice,

the best film thickness depends on the viscosity of the sample: a low viscosity film requires a thinner film, as a thick film causes excess liquid to run off the wheel and it drips through the front opening of the cell.

The pumpdown time is generally several hours to overnight should there be dissolved gases or other volatiles (e.g. H₂O) in the sample. This is especially true of the ionic liquids we have studied thus far, as they often contain a trace amount of water contamination after the synthesis. In the case of a very low vapor-pressure sample such as an ionic liquid, the sample may be heated under high vacuum in the spectrometer by passing warm water through the cooling line in order to drive off the volatile portion. This warming has facilitated the outgassing process greatly when done over a period of several hours at ca. 40° C.

3.8.2 Pumpdown

The pressure must be sufficiently low before an experiment can begin. Initialization of the vacuum system must occur in a systematic way; for example, operation of the diffusion pumps depends on the roughing vacuum as well as the right cooling conditions. A sequence of events must occur properly in order to achieve pumping, satisfying the requirements that allow the DP Control Unit to power the diffusion pumps. Experiments are not begun if the chamber pressure stays above $\sim 10^{-5}$ Torr or if the ion gun region is above $\sim 10^{-6}$ Torr as either of these readings indicates a problem with the either the sample or the vacuum.

3.8.3 Ion Gun Initialization

Special care is taken when first using the ion gun at the start of an experiment, after a new liquid sample has been introduced. If the system has not been pumping for more than several hours it is generally good practice to bake the gun at $\sim 150^{\circ}\text{C}$ by means of resistive heating tape for a few hours. Experience with the OCI IG70 gun shows that the best performance occurs when the filament is slowly warmed rather than ramped quickly up to its operating current. In practice, the filament current is increased in increments of $\sim 0.5\text{ A}$ spaced ~ 15 minutes apart to ensure even heating, and the gun's performance improves when this procedure is followed. A small electric fan is placed near the filament portion of the gun in order to cool the exterior per manufacturer recommendation. In general the ion beam current is maximized when the filament current is $\sim 2.8\text{ A}$, though the maximum setting is $> 3\text{ A}$.

3.8.4 Sample Temperature Regulation

The sample is equilibrated to the desired temperature for ca. 30 minutes before an experiment commences. The MGW-Lauda RC3 chiller is set to the desired temperature and the water pump turned on. For most of the experiments, the temperature selected was in the range of $20^{\circ}\text{--}22^{\circ}\text{C}$, and was not crucial to the experiment; the primary concern was to reduce the amount of evaporation. The sample temperature was a concern for some later experiments, and a thermocouple was subsequently installed for the purpose of monitoring the temperature. The RC3 unit is

kept continuously in operation for the duration of the experiment, so the temperature is essentially kept constant throughout.

3.8.5 Creation of Liquid Surface

The primary considerations here are to verify that the sample wheel turns and that a liquid film is created on the wheel. A visual determination prior to each experiment confirms both of these quantities, thanks to a conveniently positioned 2.75" glass viewport on the main chamber. With a flashlight beam, it is easy to see whether the wheel turns when the motor is turned on via the external control. Presently there are no liquid level sensors, so determination of the presence of a liquid film is more difficult, but is done in similar fashion. The cell must be positioned so that reflection of light from the wheel indicates whether a liquid film exists, and the wheel must be turning at the time of the determination.

3.8.6 Ion Beam Optimization

The discussion here will involve only the OCI IG70 ion gun. Procedures for the previously used guns are very similar. Once the ion gun filament current has been sufficiently increased, the beam can be optimized. The procedure first involves optimization of the continuous beam current into the Faraday cup near the sample, and then optimization of the pulsed current in the cup. Details of the procedure are fairly extensive, and will be avoided here; the interested reader may refer to Appendix A.

3.8.7 Detection Optimization

After the pulsed ion beam is optimized, the Turbo-MCS unit is powered first, as the accompanying software must register that the instrument is present and working. The MCS unit is designed to supply +12 V to the VT-120 preamp. The detector bias is nominally set to +2.3 kV (Ortec 556), this being the minimum voltage necessary to provide a reasonable gain to obtain a good signal-to-noise ratio.

The MCS can be used as a pseudo-Faraday cup in order to perform a final optimization of the signal-to-noise ratio (S/N). Experience has shown that the optimal (maximum) pulsed ion current does not always produce the greatest S/N. In order to do this final optimization, the MCS is run in a continuous¹ counting mode, wherein the acquisition parameters are set to provide a real-time relative measure of the S/N ratio. The details are not of great importance here, but the technique allows the user to make last-minute final adjustments to the ion optics to maximize the S/N, improving the data quality. Generally the optics upstream from the pulse plate (WF, L1, X1, Y1) are left alone and L2/X2/Y2 are fine tuned. After this optimization, the MCS settings are returned to those necessary to generate a TOF spectrum.

¹ Work performed by Michael Tassotto.

4. Initial Testing of the TOF-SARS Spectrometer and Early Results

4.1 Introduction

The previous chapter discussed in detail the important components of the TOF-SARS spectrometer constructed here, as well as how they work together to generate time-of-flight spectra. This chapter presents some of the initial results obtained using the spectrometer. It should be noted that a great deal of detail regarding the “debugging” of the system is omitted; this does not imply that the instrument immediately performed well at the throw of a switch. Once the vacuum system had been proven effective, many individual tests were performed to characterize the operation of the ion gun, ion optics, sample cell, detector, and acquisition electronics. Below are some of the initial spectra acquired, with comments regarding their importance in understanding the technique but without detailed quantitative analyses of the investigated surfaces.

4.2 Solid Surfaces

As a simple diagnostic of the capability of the spectrometer to acquire TOF scattering and recoil spectra, it was decided that some simple solid surfaces should be investigated. Ideally, pure samples containing atoms of widely varying mass would clearly demonstrate the ability of the spectrometer to differentiate between surface atoms. The readily available samples fitting this criterion included gold foil, copper foil, polytetrafluoroethylene (PTFE), which would introduce fluorine and/or carbon, and

graphite. The graphite sample was prepared differently than the other samples, by using the adhesive tape to remove a thin layer of graphite from a pyrolytic graphite monochromator (Union Carbide) and no further preparation was undertaken. All were macroscopically flat and were cleaned ultrasonically in detergent solution followed by washing and rinsing with acetone. The samples were handled with care to maintain cleanliness prior to introduction into the

spectrometer, but on introduction no special means of preparing the surface was available (a high-current ion gun is generally available for sputtering solid surfaces). This phase of the testing was somewhat of an afterthought, as the vacuum apparatus was designed to handle the needs of liquid experiments and not the ultrahigh vacuum and other

requirements for solid analysis. A very simple sample holder was designed for use with the existing XYZ/rotary motion feedthrough, and the setup used in order to introduce and study the four chosen solid samples in succession is schematically illustrated in Figure 4.2.1. The Z translation allowed each of the solid samples to be aligned with the incident beam one at a time. Variation of the incident angle was accomplished via the rotary motion manipulator. Samples were mounted to an electrically grounded stainless steel plate via carbon conductive adhesive tape (Structure Probe Inc.), a double-sided tape impregnated with graphite particulates to enhance electrical conductivity. The

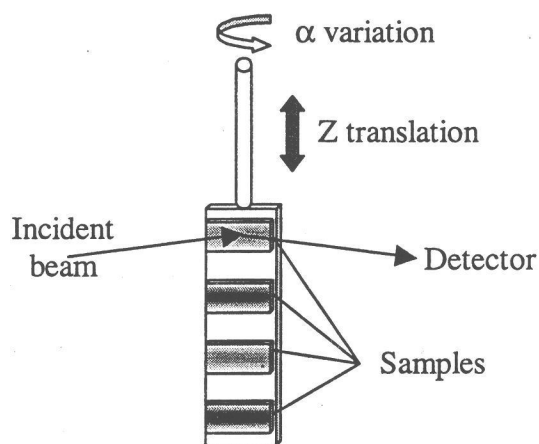


Figure 4.2.1 Schematic of the solid sample mounting apparatus.

samples were electrically conductive with the exception of the PTFE to avoid charging of the surface. As it would turn out, the problem of surface charging was of secondary concern.

Time-of-flight spectra of all of the samples were obtained using an incident beam of 3.0 keV Ar^+ ions. Resulting spectra are displayed in Figure 4.2.2, and the data has not been filtered or modified in any way other than the addition of a scalar quantity to offset the curves for easier viewing and truncation at $\text{TOF} = 20 \mu\text{s}$ to expand the region of interest. During this testing it was not a priority to obtain spectra over a range of incident angles, a useful experiment to be described later. The goal here was to investigate the character of recoil signals from liquid surfaces and in so doing to obtain the maximum signal possible. It was not until a later time that the rotary motion was calibrated in angular increments, so the incident angle here can only be approximated to $\sim 16^\circ$, a value that normally gives the maximum recoil signal.

Some observations regarding this set of experimental data are immediately obvious. Aside from the generally poor signal to noise ratio of the scans, the spectra appear qualitatively much too similar to have originated from such diverse surfaces. The recoil and possible single scattering signals generated from these surfaces should display more dramatic differences in flight times. A listing of the predicted flight times for signals based on the atoms expected from these samples and the observed signals is given in Table 4.1. The recoil signals in the spectra have been labeled as H (DR) and C (DR), with peak maxima near 6.3 and 8.2 μs respectively. Initially it was not known what caused these signals, though adsorbed H_2O , a common contaminant on surfaces

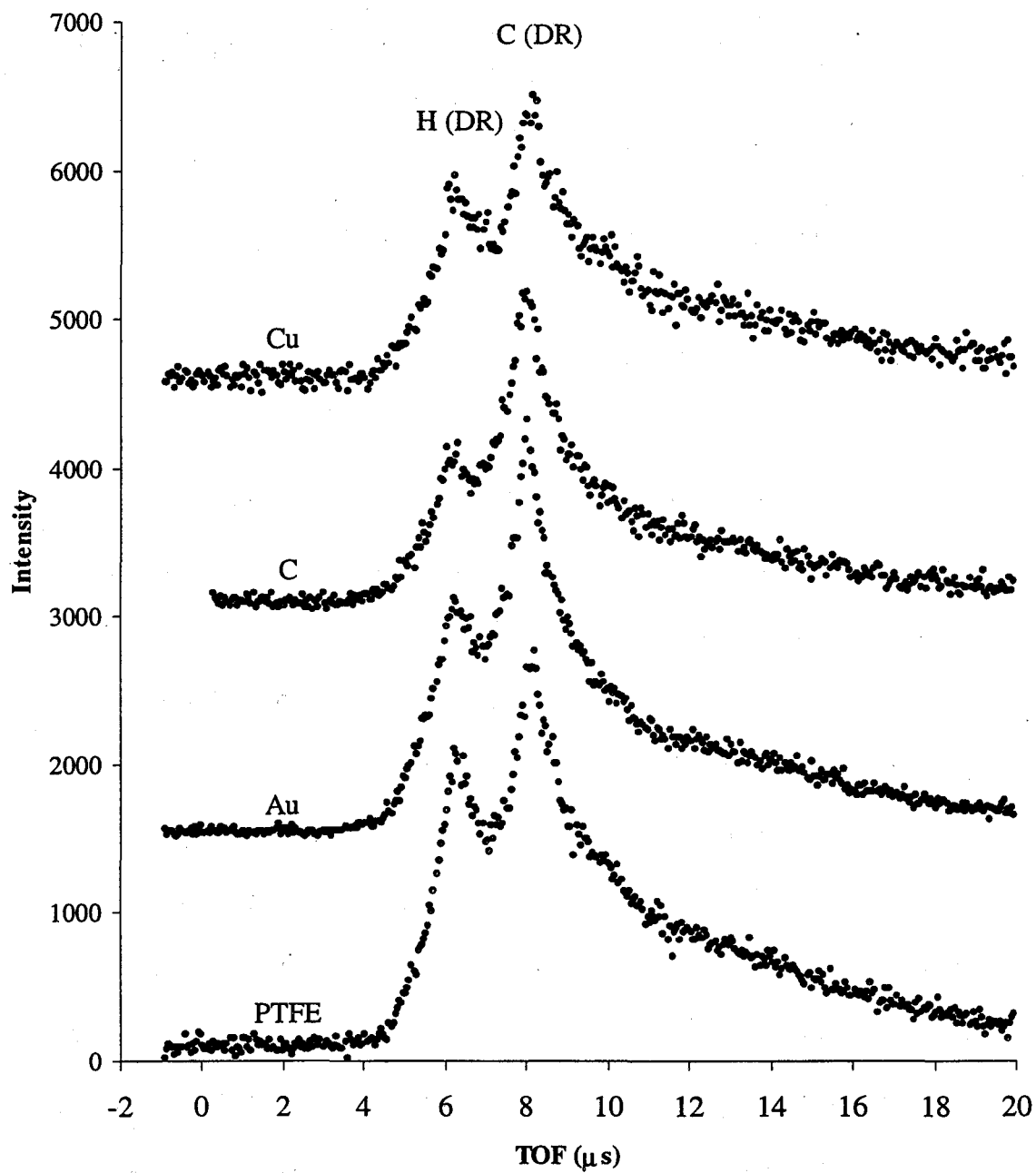


Figure 4.2.2 TOF spectra of solid surfaces obtained using 3.0 keV Ar^+ incident ions. Cu = copper; C = graphite; Au = gold; PTFE = polytetrafluoroethylene. Approximate $\alpha = 16^\circ$.

Table 4.1 TOFs for 3.0 keV Ar⁺ events.

Surface	Atom (event)	Predicted TOF, μs	Observed TOF, μs
Copper	Cu (DR)	16.52	6.25, 8.3
Graphite	C (DR)	8.29	6.3, 8.1
Gold	Au (DR)	37.82	6.3, 8.0
	Au (SS)	9.57	
PTFE	C (DR)	8.29	6.3, 8.1
	F (DR)	9.41	
	O (DR)	8.93	Not observed

that have been exposed to air, was a possibility. If this were true, a signal for oxygen recoils (8.93 μs) should have been distinguishable from the observed signal near 8.1 μs . Table 4.1 also includes the predicted flight time for O atoms for comparison purposes.

An additional observation is that the intensity ratios of the two signals appear, at least qualitatively, to change between the different samples while the positions of the peaks remain relatively constant. For example, in all of the spectra the maximum intensity of the later peak is higher than for the earlier peak, but this effect is more pronounced in the graphite and gold spectra than the PTFE spectrum. This interesting result may arise from either of two possible scenarios, neither of which can be proven based on the data at hand. The nearly identical peak positions suggest that the same two physical events are occurring in all of the trials. However, as will be demonstrated in later chapters, the experimental intensity ratios vary as a function of the incident angle, the result of slight alteration of the ion penetration depth. Varying the incident angle by a small but unknown amount between trials may have produced this effect, but it is somewhat unlikely that these small variances would result in the marked change. Another plausible scenario is that the signals arise from some adsorbed molecule,

whether water or some hydrocarbon-like contaminant, which exhibits some preferred orientation on the surface, resulting in a slightly different ratio of accessible atoms. In either case, it would appear that the two signals match closely with the predicted flight times of H recoils ($6.3 \mu\text{s}$) and C recoils ($\sim 8.2 \mu\text{s}$), but the source of these atoms remained a mystery at this point.

In an attempt to remove the surface adsorbate, a rudimentary heating device was installed on the rear of the sample mounting device. A resistively heated filament was manufactured by stretching a tight coil of tungsten wire between two electrically isolated posts mounted behind the steel plate, placing it ~ 1 cm behind the samples and oriented parallel to the plate to heat the samples as evenly as possible. A K-type thermocouple was installed near the uppermost sample to gauge the temperature during heating. Passing a current of ~ 1.5 volts through the filament was sufficient to register a temperature of 115°C after ca. 20 min. of heating, and the reading was quite stable considering the simplicity of the control.

The graphite sample was investigated at room temperature (24°C) and during the

final stage of heating at 115°C for several hours. Figure 4.2.3 illustrates the comparison between the spectra acquired at the low temperature and after heating. This treatment should have been sufficient to remove much of the supposed physisorbed H_2O

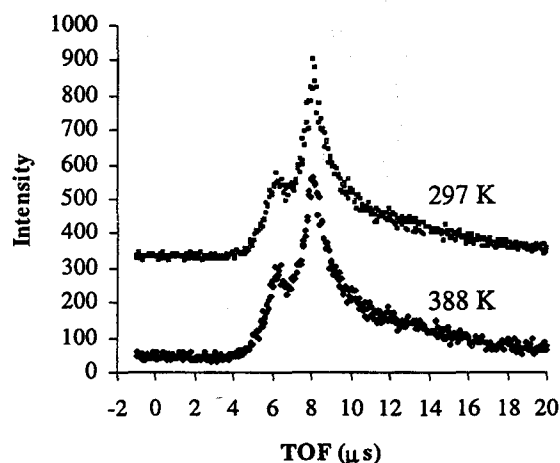


Figure 4.2.3 3 keV Ar^+ TOF spectra of contaminated graphite, before (297 K) and during (388 K) heating.

(adsorbed on the surface by weak van der Waals forces). However, the spectrum obtained after heating showed no marked difference from the original low-temperature spectrum. It now appeared that the contaminant was not water but some less volatile hydrocarbon-like material, and the most likely source was the diffusion pump fluid, 1,1,5,5-tetraphenyl-1,3,3,5-tetramethyltrisiloxane, or TTTS ($C_{28}H_{32}Si_3O_2$), illustrated in Figure 4.2.4. In this molecule the trisiloxane Si-O-Si-O-Si backbone is likely somewhat obscured by the bulky phenyl groups on the surface. The main vacuum chamber is located directly above DP1, the largest of the diffusion pumps, and at the time no special precautions were taken to minimize backstreaming of the pump fluid vapor. It appeared that TTTS vapor was condensing on the sample surfaces as well as other surfaces in the chamber.

A final test was performed on the graphite sample in order to determine whether TTTS was indeed the adsorbate.

X-ray photoelectron spectroscopy (XPS) is available in this laboratory and it is capable of detecting all elements except H, and probes to a depth of several atomic layers. A scan of the graphite sample was taken immediately following its removal from the TOF-SARS spectrometer¹. The data analysis utilizes software routines written specifically for background subtraction and quantifying the amounts of each element present. Though no spectral output is available, the XPS study was able to identify three elements with the following atomic

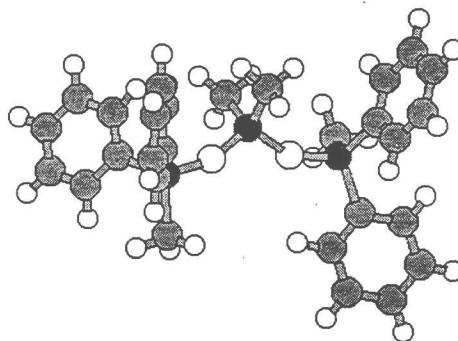


Figure 4.2.4 Space-filling model of TTTS.

percent compositions: oxygen, 5.25%; carbon, 89.76%, and silicon, 5.00%. Atom identification is certainly consistent with the formula of TTTS, and although not exact, the percent composition is reasonable in the order of magnitude. Based on the stoichiometry of the TTTS formula, the atomic composition is 6.1% oxygen, 84.8% carbon, and 9.1% silicon. The difference between experiment and stoichiometric compositions is typical of the accuracy of the XPS technique, and analysis beyond this extent was deemed unnecessary. A liquid spectrum of TTTS was not pursued as the fluid is very difficult to remove from most surfaces, and filling the cell would risk future contamination of samples. Silicon atoms would arise from no other source than TTTS and this could be the only contaminant found on all samples independently. The conclusion drawn from this phase of the testing was that although the spectrometer was functioning properly within the framework of collecting TOF recoil and scattering data, the current apparatus was unsuitable for investigation of solid surfaces. From here the investigation of liquid surfaces was commenced.

4.3. First Observations of a Liquid Surface

A sample that would reliably behave in vacuum for surface study was needed. Based on earlier molecular beam scattering studies (Saecker, Govoni et al. 1991; Saecker and Nathanson 1993), glycerol ($C_3H_8O_3$) was a very good first choice among low-vapor pressure liquids. Further detail regarding this molecule will be discussed in much greater detail in a later chapter. The spectrometer had been characterized to a point where it was certain that reasonable time-of-flight scattering and recoil spectra

¹ Performed by Michael Tassotto.

were being generated in a reproducible manner. More attention to the details of incident angle measurement and beam optimization would be necessary before attempting quantitative work, but at this point the purpose was to simply generate a spectrum originating from a liquid surface.

After filling with the appropriate amount of glycerol, the liquid sample cell was installed in place of the solid sample holder. After thorough degassing (overnight) in the spectrometer, the ion beam was optimized for 3 keV Ar⁺ ions, and time-of-flight spectra were obtained from both the stationary stainless steel sample wheel, rather fortuitously, and from the surface of liquid glycerol. In the first spectrum the wheel motor had not been turned on, and the resulting

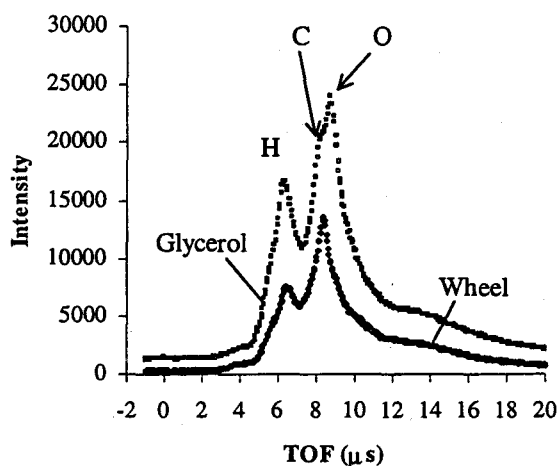


Figure 4.3.1 3.0 keV Ar⁺ TOF-SARS spectra from glycerol and the stainless sample wheel.

spectrum was nearly identical to the previously acquired spectra from solids. Turning the wheel gave a similar spectrum but with an added feature, an additional signal centered near 8.9 μs closely following the C (DR) signal. The effect was reproducible; if the wheel had not been turned in some time, generating a fresh liquid surface, the spectrum would appear to match the TTTS spectrum of Figure 4.2.2. Figure 4.3.1 illustrates the observed difference between the two spectra. Both of these spectra were acquired by summing 12.6 million passes over the time-of-flight window, resulting in the low noise level visible in the spectra. The incident angle α is not accurately known

but it is the same in each of the spectra. The low-intensity shoulder near 4 μs can be attributed to surface recoils, H atoms that recoil and then undergo scattering from surface C or O atoms. The shoulder at longer flight times ($\sim 14 \mu\text{s}$) is not fully understood but may result either from multiple scattering of argon from the surface or recoiled atoms that originate from the second atomic layer of the surface.

It was also possible to obtain time-of-flight data using helium ions as projectiles. The ion beam was later optimized to give a suitable current for investigation using 2.5 keV He^+ ions. It was not expected that the resolving power of helium ions would prove useful, as the probability for scattering from C and O atoms is much greater than for recoils, resulting in very low recoil intensities. Additionally, the flight times predicted for He scattering from C and O are very close together, and do not allow resolution of the signals. Figure 4.3.2 illustrates the spectrum obtained from glycerol by summing 5 million passes over a 40 μs flight time window. Table 4.2 lists the predicted flight times for the important physical events occurring under 2.5 keV He^+ ion bombardment.

The data in Figure 4.3.2 has been truncated to expand the region of interest, and the region from about 7 μs on has been scaled by a factor of 20 to make visible the very low intensity C and O

recoil signals. This spectrum has been included as an example of the type of data that

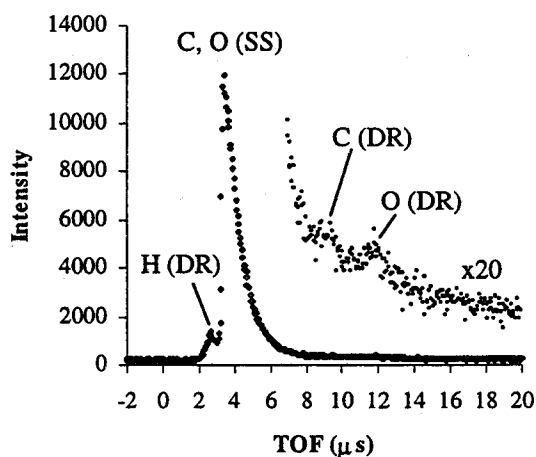


Figure 4.3.2 2.5 keV He^+ TOF-SARS spectrum of glycerol. The long flight times are expanded by 20x.

can be expected from helium ion bombardment, but it demonstrates the fact that helium data will not be very useful for quantitative work. Helium bombardment is more useful for solid studies of solid oxides, for example, where large mass differences between atoms in the target are found.

Table 4.2 TOFS for 2.5 keV He⁺ events.

Atom (event)	Predicted TOF, μs	Observed TOF, μs
H (DR)	2.76	2.65
C (DR)	8.84	8.9 \pm 0.5
O (DR)	11.05	11.8 \pm 0.5
C (SS)	3.45	Unresolved
O (SS)	3.37	Unresolved

4.4 Conclusion

This set of experiments was a breakthrough in the overall success of this technique in terms of the capability of the apparatus in generating TOF scattering and recoiling data from liquids. It was initially proven that the spectrometer could acquire TOF spectra from solid surfaces contaminated with a polysiloxane. The next experiment involved the introduction of a liquid sample, which was a challenge in the context of operating in vacuum, as well as being the first of the liquids to be investigated by TOF-SARS. The comparison of the spectrum from the stationary stainless steel sample wheel with the spectrum of the wheel while it was turning and coated with a film of glycerol convincingly demonstrated that we can in fact investigate liquid surfaces through the TOF-SARS technique.

5. First Observation of Liquid Surface Molecular Orientation: “Heads” or “Tails”

5.1 Introduction

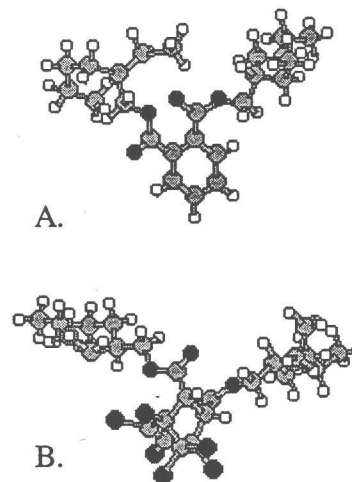
In the work up to this point it has been shown that the time-of-flight scattering technique developed here is capable of identifying atoms at the outermost layers of liquid surfaces. In the case of molecular liquids, it should be possible to measure the atomic composition of the surface and from this information to deduce the orientation of these molecules. In building the base of knowledge necessary to perform such analysis, it was first decided to choose two systems quite similar in structure and yet set apart by some distinctive feature, in this case two molecules having fairly distinct “head” and “tail” features were chosen and compared.

The two most suitable compounds for this study were a complementary pair of di-esters: bis(2-ethylhexyl) phthalate, commonly referred to as dioctyl phthalate (DOP), and bis(2-ethylhexyl) chlorendate (BEHC). Both are used as plasticizers in the polymer industry, DOP being the more widely recognized. DOP has recently received some negative attention as a pollutant and toxin, particularly for its use in polyvinyl chloride containers for food and medical storage applications (Jaeger and Rubin 1997). The interesting structural features of these two molecules are a carbon ring “head” and two adjacent ester tails, which add long hydrocarbon chains. In the case of DOP, the head is a phenyl group, whereas the BEHC molecule contains a 2,2,1-bicyclic structure that is extensively substituted with six chlorine atoms. Table 5.1 details some of the bulk properties of each of the compounds.

Table 5.1 Bulk Properties of DOP and BEHC.

	DOP (99%)	BEHC (95%)
Formula	C ₂₄ H ₃₈ O ₄	C ₂₅ H ₃₆ O ₄ Cl ₆
Mass (AMU)	390.6	613.3
Density (g/cm ³)	0.981	1.240
Melting point (°C)	-50	-
Boiling Point (°C)	384	233/0.3 torr
Vapor pressure (torr)	-	-

The structures of the DOP and BEHC molecules are displayed as ball-and-cylinder models in Figure 5.1.1. Reasonable, semi-relaxed conformations for the ethyl-substituted C₆ ester tail chains have been chosen, although no rigorous modeling of the conformation has been performed. The geometries were optimized using semi-empirical methods within the Hyperchem™ software that was used to construct these models. There is no reason to believe that these chains would be either extremely extended or tightly coiled in the liquid phase. The ester chains are identical in the two compounds, but the heads are strikingly different; DOP exhibits a C to H stoichiometry of 1:1 in the phenyl group, where BEHC has a Cl to C ratio of 0.85. It is expected that this difference can be exploited in determination of the average surface molecular orientations of these molecules.

**Figure 5.1.1** Ball-and-cylinder representations of the DOP (A.) and BEHC (B.) molecules.

5.2 Experimental

Diethyl phthalate and bis(2-ethylhexyl) chlorendate were obtained from Aldrich and employed as received. The 95% purity of the BEHC is assumed to result from incomplete chlorination of the bridgehead structure, and should not have a profound effect on the overall surface composition. Prior to investigation of a sample by the TOF-SARS technique, 50 to 55 ml of the sample was dispensed into the liquid sample cell, which was placed in the spectrometer and degassed for at least 12 hours by vacuum pumping. Sets of TOF-SARS spectra were obtained over a range of incident angles (α) for various incident singularly charged ions, varying the mass and kinetic energy of the projectiles when appropriate.

The TOF-SARS data collected was somewhat limited by equipment malfunctions, and the best available set of data for both compounds was obtained using 3.0 keV Ar^+ projectiles. At a later time additional data was obtained for BEHC and this is included in Appendix B, but the discussion here will focus on the 3 keV Ar^+ experiments. A range of incident angles α from 8° to 25° was used for data acquisition. The scattering and recoil detection angle is fixed at $\theta = \phi = 45^\circ$.

5.3 Results

A comparison of normalized TOF spectra for DOP and BEHC taken using 3.0 keV Ar^+ projectiles at incident angle $\alpha = 8^\circ$ is given in Figure 5.3.1. The DOP spectrum has been normalized to the maximum intensity of the BEHC data, but only a small adjustment was necessary as nearly identical beam currents were used. The

small peak labeled P was used to calibrate the zero flight time. The DOP spectrum shown by the solid line exhibits two large peaks near 6.6 and 8.5 μs flight times. According to the predicted flight times for recoiled atoms, these times identify closely with those for recoiled H and C atoms, respectively. Table 5.2 lists the predicted and observed flight times for the associated events in both the DOP and BEHC spectra. No other identifying features are present in the DOP spectrum. Though not resolved, a small oxygen recoil peak may be present in the spectrum (predicted at 8.93 μs), possibly obscured by the large C (DR) signal. (DR) signal.

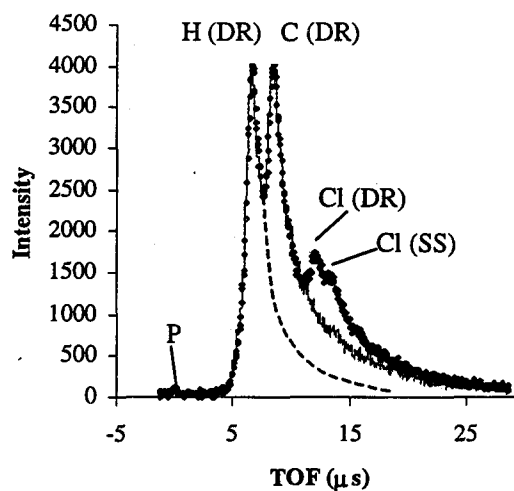


Figure 5.3.1 TOF-SARS spectra using 3 keV Ar^+ ions from DOP (\bullet) and BEHC ($-$). The background function used to determine intensity ratios is also shown.

The 3.0 keV Ar^+ spectrum in Figure 5.3.1 shows the nearly identical characteristic H (DR) and C (DR) peaks in the same positions as the DOP spectrum. Again, no O (DR) signal can be resolved. Superimposed on the long-TOF tails in the spectrum are two additional low-intensity features. The peak at 12.1 μs is close to the expected flight time of recoiling chlorine atoms. Closely following this signal is a similar feature that does not correspond to any reasonable recoiled atom, rather it matches well with the expected flight time of argon ions that undergo single scattering from Cl atoms, allowed in the context of the critical angle (Equation 2.1.3).

Table 5.2 TOFs for 3.0 keV Ar⁺ events.

Atom (event)	Predicted TOF, μs	Observed TOF, μs	
		DOP	BEHC
H (DR)	6.54	6.56	6.66
C (DR)	8.61	8.51	8.51
O (DR)	8.93	-	-
Cl (DR)	12.04	-	12.1
Cl (SS)	13.68	-	13.6

TOF-SARS spectra were also acquired using 2.5 keV Ne⁺ ions, and Figure 5.3.2 illustrates a spectrum obtained at $\alpha = 8^\circ$ under these conditions. The presence of chlorine is confirmed by the recoil signal appearing as a small bump near 13.8 μs . Although the overall shape of this spectrum closely resembles that of the Ar⁺ scans, the peak assignments are slightly different as a result of the mass-dependent energy transfer between projectile and target. Here the sharp maximum near 8.4 μs is attributed to Ne single scattering from Cl atoms, rather than C (DR), and it appears closely behind the expected C (DR) signal (7.92 μs) such that the two signals are not resolved. Table 5.3 details the predicted and observed flight times for 2.5 keV Ne⁺-induced scattering and recoil events.

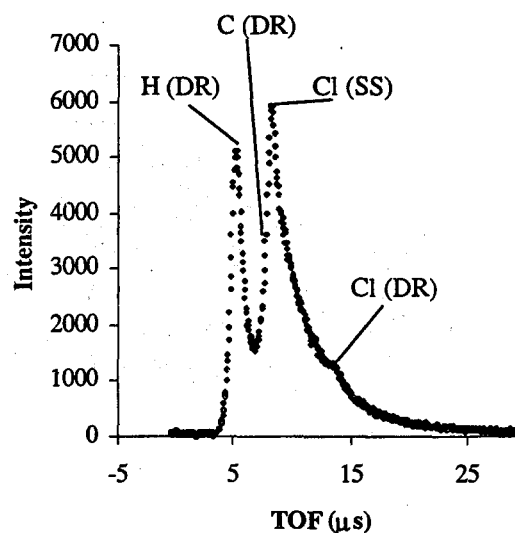
**Figure 5.3.2** TOF-SARS spectrum of BEHC using 2.5 keV Ne⁺ ions.

Table 5.3 TOFS for 2.5 keV Ar⁺ events.

Atom (event)	Predicted TOF, μs	Observed TOF, μs
H (DR)	5.21	5.21
C (DR)	7.92	7.8 \pm 0.1
O (DR)	8.90	-
Cl (DR)	13.70	13.8 \pm .01
Cl (SS)	8.36	8.36

TOF-SARS data for BEHC were additionally collected as a function of incident ion energy using argon ions. The spectra were supportive of the conclusion that some chlorine atoms are accessible on the surface of BEHC in addition to H and C.

Examples of the spectra obtained using 2.5, 2.0, and 1.5 keV Ar⁺ projectiles at $\alpha = 8^\circ$ are plotted on the same time scale in Figure 5.3.3 for qualitative comparison. The intensities have been scaled to the peak maximum of the 2.0 keV spectrum. The peak shifts to longer flight times are consistent with the square-root relationship between kinetic energy and velocity. Variation of the

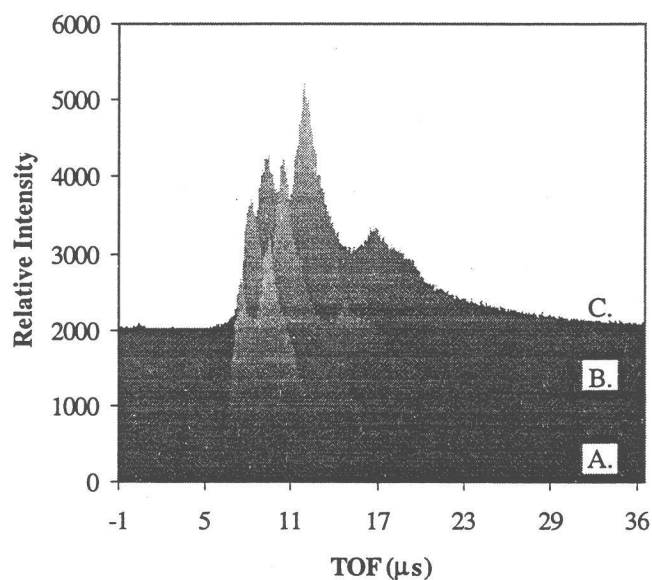


Figure 5.3.3 TOF-SARS spectra of BEHC as a function of energy. $\alpha = 8^\circ$; Ar⁺ ions plotted on the same TOF scale. A. 2.5 keV. B. 2.0 keV. C. 1.5 keV.

incident angle caused a small decrease in the H (DR) intensity relative to the C (DR) peak, and this effect will be discussed later.

5.4 Discussion

5.4.1 Experimental Intensities

The overall appearance of the DOP and BEHC spectra in Figure 5.3.1 in the C (DR) and O (DR) regions are quite similar. The major difference is the appearance of

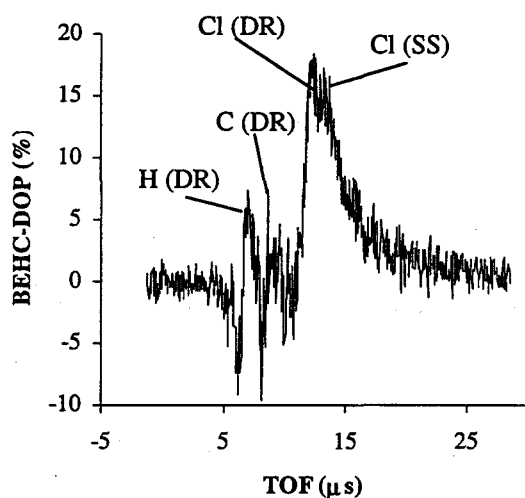


Figure 5.3.4 Difference spectrum (BEHC-DOP) based on the data in Fig. 5.3.1. Expressed as a percent of the DOP intensity maximum.

signals arising from Cl recoils and Ar scattered from Cl on the long-TOF tail of the BEHC spectrum. To illustrate this more clearly, Figure 5.3.4 is a difference spectrum between the normalized DOP and BEHC spectra displayed as a percentage of the BEHC maximum intensity. In the H and C regions the difference plot shows very little systematic difference, but in the Cl

recoil and scattering peaks region the difference is significant. Based on this observation, it is very likely that both molecules are adopting a similar orientation at the liquid surface. The clear appearance of signals originating from surface Cl atoms in the BEHC spectra implies the accessibility of at least part of the Cl-substituted ring to incident ions. Concurrently, the presence of a relatively large H (DR) signal in the

BEHC spectra excludes the H-deficient Cl-containing ring from populating the surface in an orientation having the ester tails dangling below the surface, in which case the H (DR) signal would be very small. Considering DOP, if its preferred orientation were exclusively 'head up', with the phenyl most exposed, the low H/C stoichiometry of the head would mean that the H (DR) intensity would have to be considerably lower relative to the C (DR) peak observed. The conclusion is drawn that both DOP and BEHC cannot have a 'head up' orientation.

5.4.2 Surface Atomic Ratios

Experimental intensity ratios were obtained from the TOF-SARS experiments by measuring the spectral intensity at the peak maximum. In the case of the H (DR) signal, the intensity was directly measured from the peak maximum to zero. For each later peak, the long TOF tail of previous peaks contributes to the total intensity and must be accounted for in some way. Without full understanding of the functional form, a reasonable *ad hoc* background was drawn in to represent the H tail before measuring the C (DR) intensity, shown in Figure 5.3.1 as a dashed line. Likewise, the Cl (DR) intensity was measured after removing a suitable background based on the DOP spectrum. The appropriate intensity ratios obtained from the spectra in Figure 5.3.1 are included in the upper portion of Table 5.4.

It is necessary to convert spectral intensity ratios to surface atomic ratios in order to extract quantitative information regarding the surface composition, through corrections for differences in cross sections and detector efficiencies for different atoms. The absolute spectral intensity of atom I_i depends on the total ion flux F , the

density n_i of that atom in the surface, the recoil cross section σ_i , and the detector response ϵ_i , according to

$$I_i = Fn_i\sigma_i\epsilon_i \quad 5.5.1$$

To obtain the number density the expression is solved for n_i . If ratios are taken e.g. atom i /atom j , the ion flux drops out of the expression, and the resulting expression is

$$\frac{n_i}{n_j} = \frac{I_i}{I_j} \cdot \frac{\sigma_j}{\sigma_i} \cdot \frac{\epsilon_j}{\epsilon_i} \quad 5.5.2$$

In this way the surface atomic ratios can be determined from measured spectral intensities, calculated cross sections, and the detector response. The detector response is dependent on the atomic number Z and velocity of the incident particle according to

$$\epsilon_i = \alpha(v - v_0)Z^n \quad 5.5.3$$

where $v_0 = 5.5 \times 10^4$ m/s (Dietz and Sheffield 1975) and $n \approx 0.8$. The critical velocity v_0 is nearly independent of the particle mass, and incident particles with velocities below this value are not capable of producing secondary electrons. The issue of mass dependence of detector efficiency is not well documented among ion-scattering researchers; most have not addressed this directly while some authors have assessed a value of $Z^{0.4}$ (Chen, Shi et al. 1986), taken from an early study by Burrous et al (Burrous, Lieber et al. 1967). However, a survey of several electron multiplier sensitivity investigations (Watson 1999) suggests that 0.4 is too low and the correct value is likely much closer to unity, making 0.8 a more reasonable value. The uncertainty in this value is considered in the error estimates for atomic surface ratio

calculations. Taking ratios eliminates the need for knowing the exact value of α as it cancels. The recoil cross sections σ_{DR} for H, C, and Cl were calculated using the Molière potential for 3.0 keV Ar^+ ions and a 45° recoil angle. In this calculation the screening length parameter (Mashkova 1985) was set to 1.0, and the resulting σ values were $\sigma_H = 0.215 \text{ \AA}^2$, $\sigma_C = 0.120 \text{ \AA}^2$, and $\sigma_{Cl} = 0.141 \text{ \AA}^2$. Using Equation 5.5.2, surface atomic ratios were calculated based on the spectra obtained for DOP and BEHC and these values are listed in the latter part of Table 5.4.

Table 5.4 Experimental intensity ratios and derived atomic ratios for DOP and BEHC.

	DOP	BEHC
Intensity (± 0.04)		
I_H/I_C	1.17	1.19
I_{Cl}/I_C	0	0.25
Atomic (± 0.1)		
n_H/n_C	1.8	1.9
n_{Cl}/n_C	0	0.2

Based on the earlier discussion the 'head-up' orientation of DOP and BEHC can be eliminated as a possibility. Figure 5.4.1 offers some possible models for orientations of the BEHC molecule that would expose different portions of the chlorinated ring and both ester tails (A., C.) or a single tail (B.). The images shown in D. through F. of Figure 5.4.1 are surface orientations for DOP that include 'head-down' (D.) and one (E.) or both (F.) tails exposed. Assuming that our TOF signals originate in the top 5 \AA of the surface, accounting for a reasonable degree of surface corrugation, Figure 5.4.1 includes the expected stoichiometric ratios corresponding to the atomic ratios in Table 5.3. The ratios as presented include a range of values to account for differences in the way that the accessible atoms may be counted.

Shadowing and blocking effects are also taken into account in the counting of atoms. Though understood much more completely for solids (Rabalais 1990; Rabalais 1991), these effects likely also play a considerable role in the observation of surface composition of liquids. For crystalline solids, recoil intensities that appear or disappear at specific incident angles can reveal information regarding interatomic distances. In non-crystalline solids and liquids the higher disorder obscures these effects; however, shadowing and blocking effects can qualitatively assist in assigning which surface atoms are accessible. For example, a 3 keV Ar⁺ ion colliding with an H atom may recoil that atom, but the Ar trajectory changes very little. In this case, the shadowing and blocking effects of H atoms are negligible; however, a carbon (or heavier atom) can significantly shadow atoms behind it and/or is more likely to be blocked during exit. Shadowing and blocking effects within the long ester tails of both molecules should be small due to the flexible nature of the chains and the averaging effect of the technique. The fairly rigid seven-membered ring in BEHC is more likely to exhibit shadowing and blocking, as the large Cl atoms will effectively shadow/block C atoms lying behind or below chlorine atoms.

The H/C ratios for DOP orientations with one or both tails and the ring exposed (Fig. 5.4.1 E., F.) produce H/C ratios from 1.4 to 1.6, too low for the experimentally observed value of 1.8. In order to assume a stoichiometric H/C ratio near the experimental value of 1.8, the DOP molecules must be 'head down' as shown in D, although the options involving one or both tails at the surface are difficult to distinguish from one another.

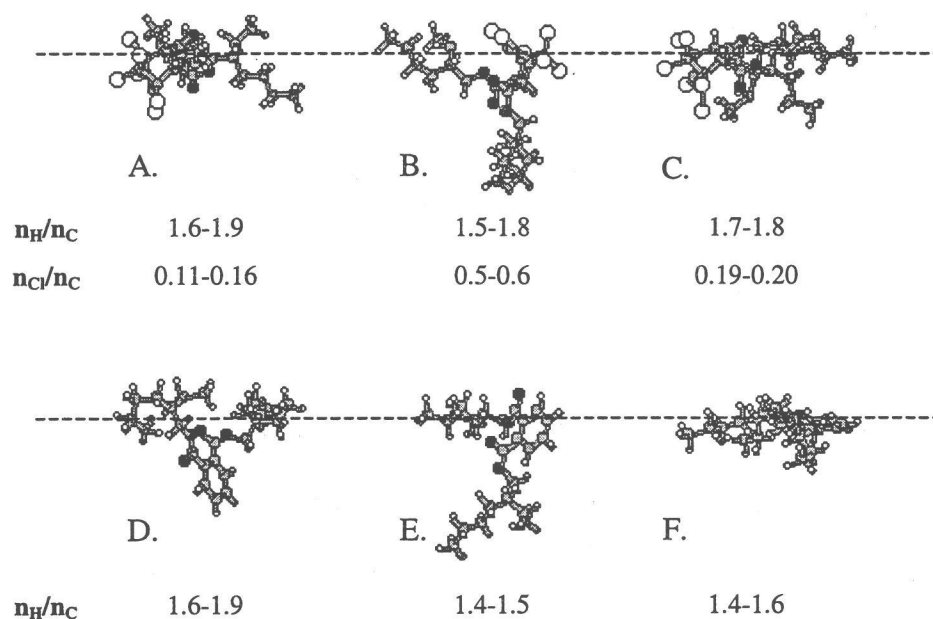


Figure 5.4.1 Possible surface orientations of BEHC (A.-C.) and DOP (D.-F.). Chlorine atoms in BEHC are white; all oxygens are black.

For BEHC, orientations similar to the one shown in Fig. 5.4.1 B., with the majority of the ring exposed, have Cl/C stoichiometries too high (0.5-0.6) in comparison to the experimental value of 0.2. On the other hand, an orientation resembling the one in A. of Fig. 5.4.1, which submerges most of the ring, has a Cl/C ratio of 0.11-0.16 that is lower than the experimental ratio. The remaining possibilities, including the orientation shown in 5.4.1 C. of the figure, that involve two to three chlorines at the surface, provide the correct Cl/C ratio of ~0.2. More than one orientation giving this stoichiometry is possible, if a part of the Cl-substituted head is rotated into the surface and at least one of the tails is predominantly accessible.

The ring structure of BEHC contains only two H atoms and the ring C atoms are extensively shadowed and blocked by Cl atoms, limiting the effect of ring orientation on the H/C ratio. It is estimated that the H/C ratio varies little with orientation (1.6-1.9) and covers a range that includes the experimental value of ~1.9;

thus we cannot determine which part of the ring is exposed. Based on this result it is difficult to say definitively whether one or both tails are in the surface, but it is clear that only part of the 'head' of BEHC is exposed at the surface.

5.5 Conclusion

TOF-SARS was applied to a pair of low-vapor pressure compounds, dioctyl phthalate (DOP) and bis(2-ethylhexyl) chloroendate (BEHC), in order to determine whether there is preferred surface orientation of surface molecules. Comparison of TOF-SARS spectra of both compounds under similar experimental conditions revealed very similar relative amounts of H and C accessible at the surface, suggesting that a common orientation may be favored. The BEHC spectrum had additional features attributed to recoiled Cl and Ar scattering from Cl atoms in the ring, evidence that the chlorinated head is at least partly exposed. A comparison of the estimated surface stoichiometry of the BEHC and DOP molecules in various reasonable orientations and the experimentally determined C/H surface atomic ratio (1.6-1.9) was made. An orientation that exposes one or both tails at the surface is favored, with the ring 'head' partially exposed so that 2-3 of the 6 Cl atoms present are accessible. In DOP, exposure of the head at the surface results in H/C ratios low enough to rule out orientations that expose a large portion of the head. An orientation favoring both tails exposed at the surface with very little of the phenyl 'head' exposed is most likely.

This study marks the first step toward understanding how the TOF-SARS technique can be used to help determine molecular orientations. As a first attempt, it has shown its ability to differentiate between surface atoms of different mass. A better

method of estimating stoichiometric atomic ratios on the surface for different molecular orientations would be a great help, as the counting of accessible atoms by hand is tedious. However, a sensible conclusion was possible in this case where two molecules under study had considerably different 'head-tails' architecture.

6. TOF-SARS Investigation of the Liquid Glycerol Surface

6.1 Introduction

The organic compound glycerol, commonly referred to as glycerine, was first extracted from olive oil in 1779 and dubbed “the sweet principle of fats” by Dr. Karl Wilhelm Scheele. (Laboratories 1939) At the time it was not suspected that glycerol ($C_3H_8O_3$) would gain the overall recognition that it has, and according to a 1939 publication by the Glycerine Producers Association, “...there is no other individual organic compound enjoying as wide a diversity of markets.” (Laboratories 1939) While this may no longer be true, it is certain that glycerol and its derivatives have found their way into many industrial processes and products, including a wide variety of soaps and detergents, solvents, polymers, plasticizers, and explosives, the most famous being nitroglycerine.

Glycerol has enjoyed particular attention due to its interesting liquid- and solution-phase bulk properties, which include high viscosity and boiling point, low toxicity, and good solvent ability due in part to its exceptional hydrogen bonding ability. It has gained more recent scientific attention as a model for H-bonding systems in molecular dynamics simulations (Benjamin, Wilson et al. 1994; Benjamin, Wilson et al. 1995), as well as in molecular beam scattering (MBS) studies regarding trapping and desorption mechanisms on liquid surfaces (Saecker and Nathanson 1993). The Benjamin surface simulations suggest that a CH or CH_2 group is slightly more likely to be found at the surface than an oxygen atom, and this has been generally accepted to be true in the MBS studies. However, the simulation done measures a density profile to a

depth of about 4 Å, and the experiment done here is more surface-specific than that, sensitive to the top 2 Å. Sum frequency generation (SFG) applied to glycerol/water mixtures has suggested that glycerol is enriched relative to the bulk at all concentrations, and no free OH groups are seen in neat glycerol (Baldelli, Schnitzer et al. 1997). This SFG study concludes that the surface glycerol molecules assume a nearly constant orientation over all mole fractions, approximately perpendicular to the surface plane but is inconclusive on this point. A follow-up study involving deuterated glycerol ($\text{CHOH}-(\text{CD}_2\text{OH})_2$) is underway to identify the surface orientation of the molecules; the early indication is that the molecular backbone is tilted at some angle less than 45° relative to the surface normal [Shultz, 1999 #200]. Currently the bulk condensed phases of glycerol have been simulated in considerable detail, in order to gain greater insight into possible H-bonding conformations and intra- and intermolecular spacings in the bulk (Chelli, Procacci et al. 1999; Chelli, Procacci et al. 1999). It is the objective of this work to provide more direct experimental evidence regarding the molecular orientation and accessible atoms at the surface of liquid glycerol.

6.2 Bulk Chemistry of Glycerol

Glycerol is available in several grades, ranging from low-purity industrial grades to the pharmaceutical/food grade at the upper end. The sample for this work was assayed at 99.5+% pure, and was used as supplied by the manufacturer. Table 6.1 lists some of the bulk properties of the compound. The material itself is colorless and odorless.

Table 6.1 Bulk properties of glycerol

Formula	$C_3H_8O_3$
Mass (AMU)	92.09
Density (g/cm^3)	1.26
Melting point ($^{\circ}C$)	18
Boiling Point ($^{\circ}C$)	290
Vapor pressure (torr)	9.6×10^{-3}
Viscosity (cp)	1400
Surface tension (dynes/cm)	63 ($20^{\circ}C$)

6.3 Experimental

Glycerol (99.5%, EM Scientific) was used as supplied. Approximately 55 ml of the glycerol sample was placed in the reservoir of the sample cell, which was then introduced into the vacuum chamber. The sample was degassed under high vacuum in the TOF spectrometer for >12 hours in order to remove any volatile impurities. TOF-SARS data was obtained using Ar^+ (Matheson high purity), and Ne^+ (Airco, 25% helium mixture) ions in the energy range of 1.5 to 2.5 keV and at incidence angles of $\alpha = 8^{\circ}$ to 36° in increments of 4° . The laboratory scattering and recoil angles were fixed at a value of 45° .

6.4 Results

6.4.1 Argon

A composite of the spectra acquired with 2.5 keV Ar^+ ions over the entire a range of $\alpha = 8^{\circ}$ to 36° is illustrated by Figure 6.4.1. In the figure a scalar quantity has

been added to all but the 36° spectrum in order to clearly separate the scans. The small peak labeled P visible in most scans has been used to calibrate “time zero”. Notable features of the spectra include a well-defined H (DR) signal centered near $7.3 \mu\text{s}$ and a feature resulting from two poorly resolved signals from about 9.5 to $10 \mu\text{s}$. Based on the atoms present, this feature can only be due to carbon DR and oxygen DR, but the two signals cannot be resolved. In the intermediate alpha spectra there is an additional broad feature attributed to multiple scattering effects and it is of little use in analysis of the data. A shallow inflection on the leading edge of the H (DR) peak is likely due to the surface recoil phenomenon for H atoms. Table 6.1 details the predicted DR flight times for signals arising from the atoms present glycerol for 2.5 keV Ar^+ incident ions.

Table 6.2 TOFs for 2.5 keV Ar^+ events.

Atom (event)	Predicted TOF, μs	Observed TOF, μs
H (DR)	7.16	7.3
C (DR)	9.08	~9.5
O (DR)	9.78	9.9

A small time difference between predicted and observed TOF values is likely due to a small error (ca. $\pm 0.1 \text{ keV}$) in the measured ion kinetic energy that was discovered after completion of the data acquisition. This has no bearing on the assignment of spectral features, which are difficult to resolve in any case. In an effort to better resolve the carbon and oxygen direct recoil signals it was decided to move on to investigation by means of neon ion projectiles.

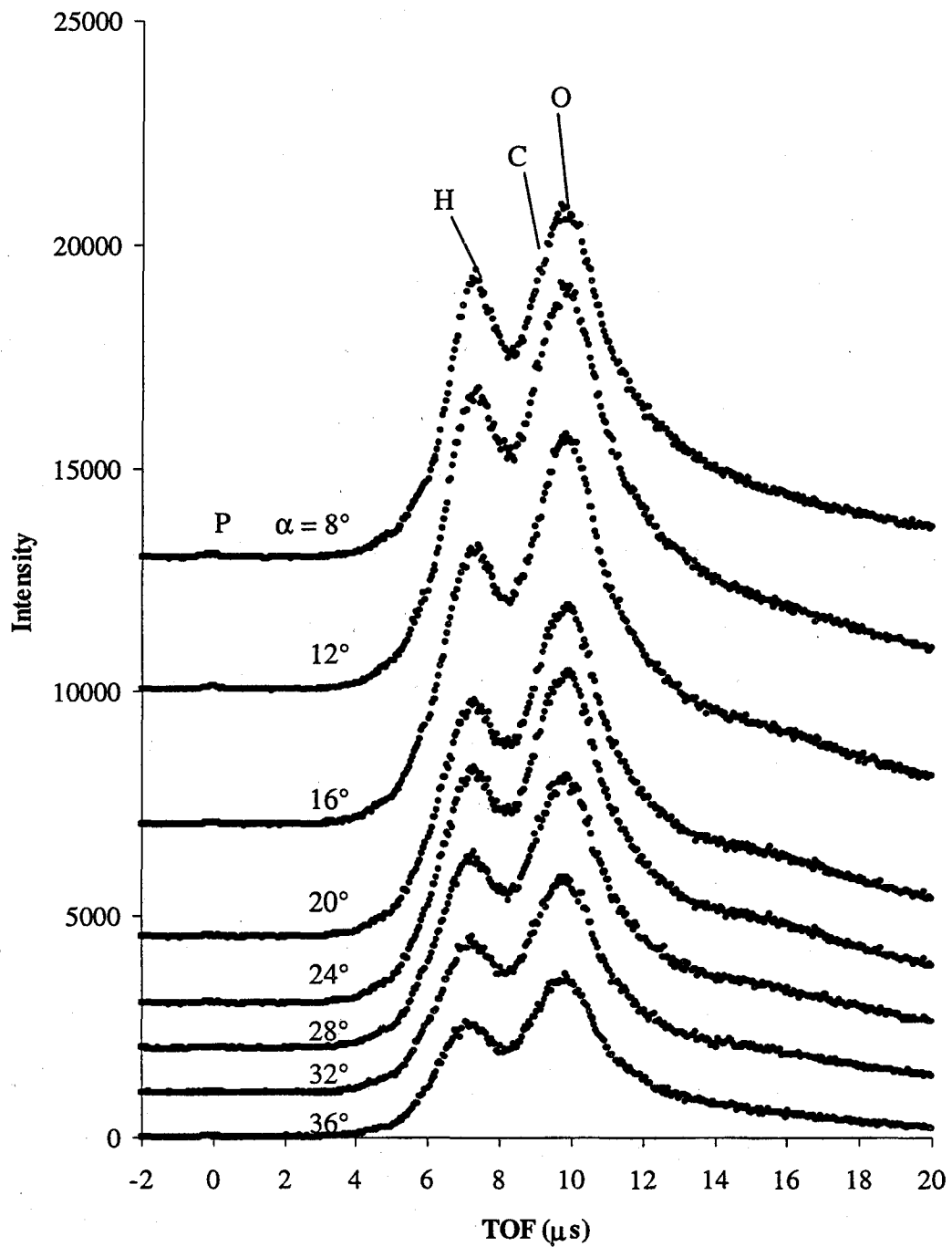


Fig. 6.4.1 Composite of TOF-SARS spectra obtained from glycerol using 2.5 keV Ar^+ ions. P = photon peak.

6.4.2 Neon

Spectra were obtained using Ne^+ ions over the same range of α values, at energies of 2.5 and 2.0 keV. Although spectra at 1.5 keV were desirable the ion beam current was insufficient at this energy. Figure 6.4.2 illustrates the composite of all spectra acquired using 2.5 keV Ne^+ TOF projectiles. The photon peak visible in several of the scans was again used to calibrate the flight times. The signals for H (DR) and C (DR) are well resolved and the O (DR) peak is somewhat more clearly separated from the C peak. Although neon single scattering from oxygen is expected near 11.8 μs , it is not observed but may contribute to the tail. On the long flight time side of the O (DR) peak is a less obvious feature- a broad, low-intensity signal that can be attributed to multiple scattering of the incident ions, and this will be discussed further. Anomalies in the incident beam optimization during some of the scans resulted in lower total peak intensities than expected, and in Figure 6.4.2 the 8° and 28° alpha scans have been scaled by factors of 2.5 and 4 respectively. This does not impede the analysis since only ratios of peak intensities within individual spectra are considered; absolute intensities are not important. The relative intensities of recoil peaks in the Ne^+ spectra are considerably different than those for Ar^+ , due to considerably different recoil cross sections when using projectiles of different masses. Table 6.3 lists the predicted and observed values for the important collision events. In an attempt to better separate the TOFs, the Ne^+ energy was lowered to 2.0 keV. Resulting spectra over the same α range are illustrated in Figure 6.4.3. The time resolution is improved, with expected flight times for the C (DR) and O (DR) signals separated by $>1 \mu\text{s}$. An unexpected low intensity feature near 3.2 μs is visible in several of the scans. This signal may result

from improper optimization of the ion beam, particularly the Wien filter that separates ions of different mass and energy out of the beam. The neon source gas included 25% helium, so a small number of helium ions may have been present in the beam during acquisition; this could give rise to H (DR) by He^+ (3.09 μs) and single scattering of He^+ from carbon (3.86 μs). Where this feature is seen, the peak intensity represents less than 10% of the hydrogen recoil intensity. Table 6.4 details the predicted vs. observed positions of each TOF event. Comparison with a model or simulation of some reasonable orientations should then reveal an estimate of the molecular orientation, if any exists. It is possible that all orientational order in small molecules is washed out through molecular tumbling; however this should not be the case with a highly hydrogen-bonding system such as glycerol. The following sections give greater detail regarding the procedures employed for extracting orientational information from the experimental data.

6.5 Discussion

6.5.1 Spectral Intensity Ratios

In each of the sets of spectra, changes in the peak intensity ratios are observed as α is varied over the entire range. It is also obvious that the overall intensities change throughout the range of α values selected. The overall intensity reaches a local maximum between incident angles of 8° and 16° , and decreases continuously as α increases. This effect is not completely understood, but is related to the competing

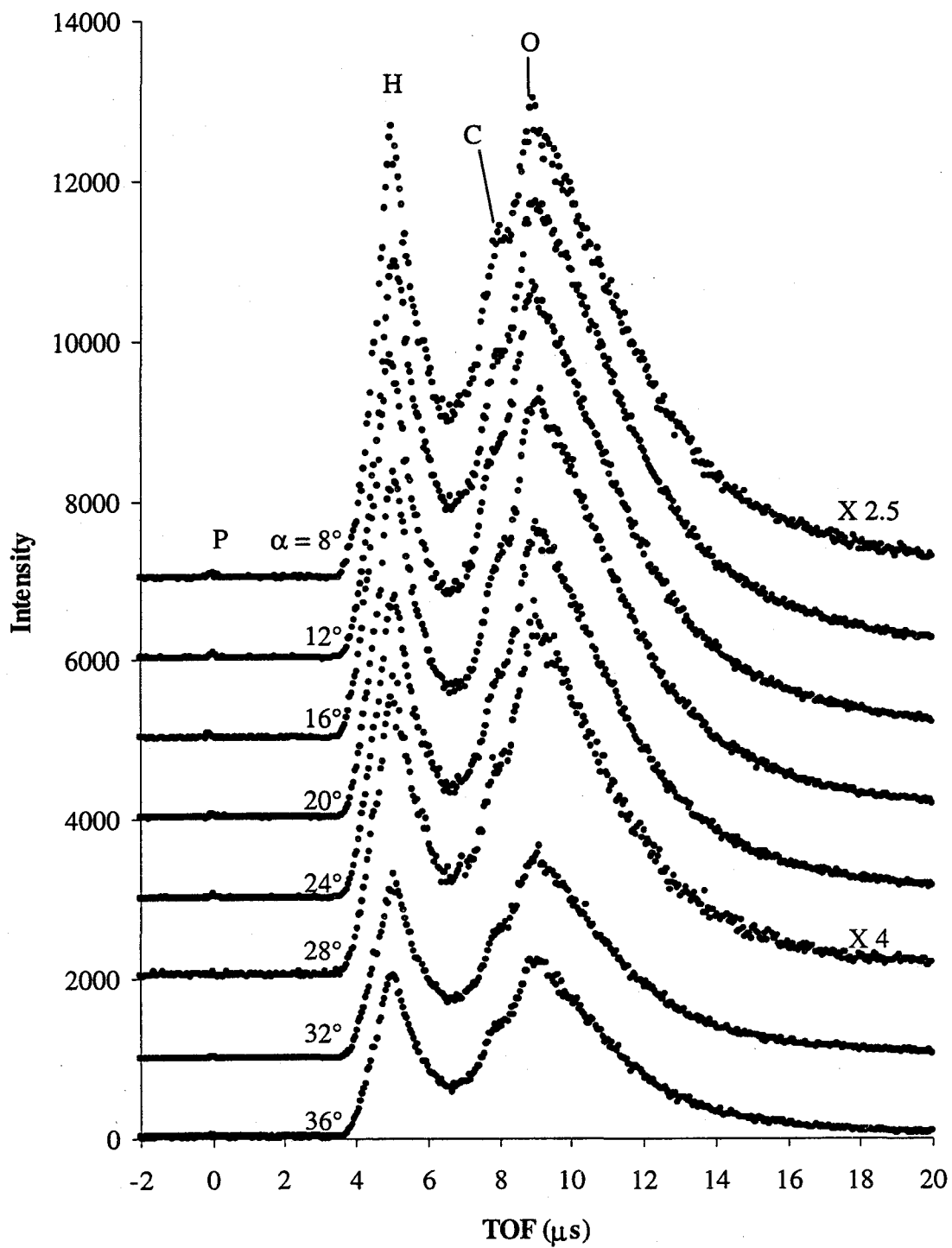


Fig. 6.4.2 Composite of TOF-SARS spectra obtained from glycerol using 2.5 keV Ne^+ ions. P = photon peak.

Table 6.3 TOFs for 2.5 keV Ne⁺ events.

Atom (event)	Predicted TOF, μs	Observed TOF, μs
H (DR)	5.21	5.1
C (DR)	7.92	8.03
O (DR)	8.90	8.93
O (SS)	11.81	Not resolved

factors of shadowing and blocking of the incident and exiting particles. Taking ratios of intensities within individual spectra makes consideration of the overall intensity unnecessary.

Intensity measurements are complicated by a lack of knowledge of the true functional form of the long tails associated with each peak in the TOF spectrum. Recent work in this lab indicates that the tails provide some information regarding the depth at which these signals originate. Recoils that originate deeper in the surface lose additional energy through collisions as they exit the surface; those ions that travel deeper into the surface before generating a recoil will also lose energy, resulting in slower recoils. We can be certain that the recoil signals which arrive very close to the predicted flight times have originated in the outermost molecular layer—approximately the top 2 Å, and have undergone very little energy loss. The spectral intensities at these peak maxima are therefore proportional to the surface atomic concentrations; so intensity measurements are taken at the peak maxima. In order to account for the presence of the long tails on each peak, spectral intensities were deconvoluted and hence measured using the software package Peakfit™ 4.0 (Jandel). It should be noted that although Peakfit has algorithms to automatically fit spectra, it does so without regard for maintaining individual peak shapes or widths. As a result constraints on the

amount of variation allowed during automatic fitting were necessary, to the extent that the auto-fitting became ineffective. Additionally, the Peakfit program has a number of functions available as choices for fitting individual peaks, but no single function represented the shape of recoil signals accurately. A Gaussian-modified Gaussian (GMG) function was chosen as a reasonable shape for the surface recoil peaks, having the form

$$y = \frac{a_0}{\sqrt{2\pi}\sqrt{a_3^2 + a_2^2}} \exp\left(-\frac{1}{2} \frac{(x - a_1)^2}{a_3^2 + a_2^2}\right) \left[1 + \operatorname{erf}\left(\frac{a_3(x - a_1)}{\sqrt{2}a_2\sqrt{a_3^2 + a_2^2}}\right)\right] \quad 6.1$$

The closest match among the available functions is an exponentially modified Gaussian (EMG), which varies four parameters: the peak position, area, width, and an asymmetry parameter. The EMG function has the form

$$y = \frac{a_0}{2a_3} \exp\left(\frac{a_2^2}{2a_3^2} + \frac{a_1 - x}{a_3}\right) \left[1 + \operatorname{erf}\left(\frac{x - a_1}{\sqrt{2}a_2} - \frac{a_2}{\sqrt{2}a_3}\right)\right] \quad 6.2$$

In the formula a_0 represents the peak area, a_1 the position, a_2 the width at half maximum and a_3 the asymmetry. It was found that the EMG function could reasonably represent either the sharp peak maximum near the predicted TOF or the long tail portion of the peak, but not both simultaneously, and a better approach was necessary. The Peakfit™ software allows the user to define unique functions. After the experience of using EMG-type functions, it was decided that a reasonable custom function could be formulated by summing two EMG functions together, one that reasonably fit the sharp peak maximum and one to represent the long tail portion. To

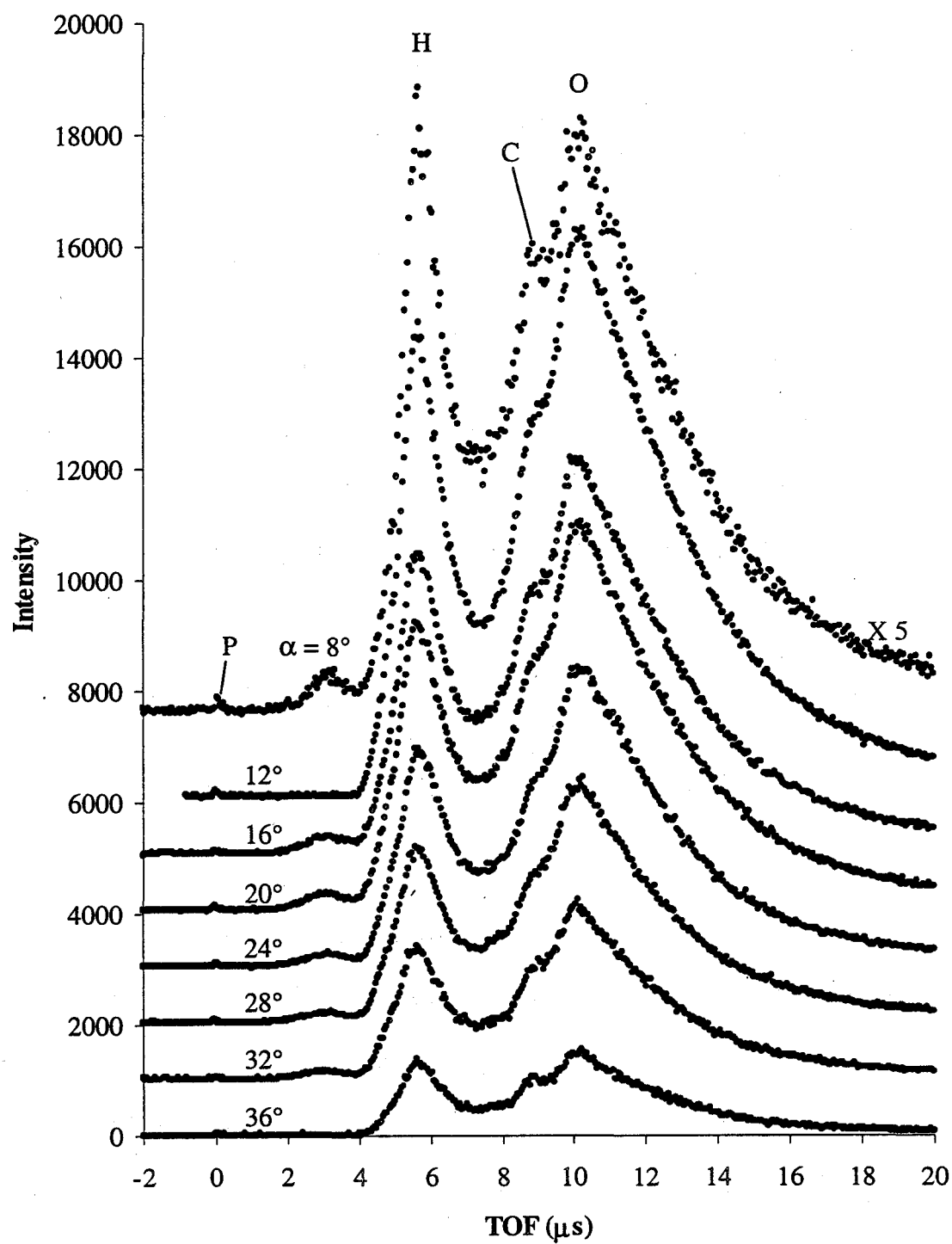


Fig. 6.4.3 Composite of TOF-SARS spectra obtained from glycerol using 2.0 keV Ne^+ ions. P = photon peak.

Table 6.4 TOFs for 2.0 keV Ne⁺ events.

Atom (event)	Predicted TOF, μs	Observed TOF, μs
H (DR)	5.83	5.7
C (DR)	8.85	9.0
O (DR)	9.95	10.1
O (SS)	13.28	Not observed

simplify the fit, the parameters of the tail EMG function were forced to scaled quantities of the parameters in the peak EMG fit, limiting the number of fitted parameters to four. This new function was formulated using the hydrogen DR peak as a model, and the C and O DR peak functions were constrained to have very similar widths and asymmetries during fitting. The user-defined function has the form

$$y = \frac{a_0}{2a_3} \exp\left(\frac{a_2^2}{2a_3^2} + \frac{a_1 - x}{a_3}\right) \left[1 + \operatorname{erf}\left(\frac{x - a_1}{\sqrt{2}a_2} - \frac{a_2}{\sqrt{2}a_3}\right)\right] + \frac{0.63a_0}{13.8a_3} \exp\left(\frac{(1.69a_2)^2}{(13.8a_3)^2} + \frac{1.16a_1 - x}{6.9a_3}\right) \left[1 + \operatorname{erf}\left(\frac{x - 0.63a_1}{2.39a_2} - \frac{1.69a_2}{9.76a_3}\right)\right] \quad 6.3$$

Unfortunately using this approach all but requires that the spectra be fit by hand, rather than the automatic algorithms Peakfit™ contains, and as a result the fits are not nearly perfect. This method allows a reasonable and reproducible means for deconvoluting the overlapping signals in the spectra, with particular emphasis on the most important regions, i.e. at the peak maxima, within reasonable error limits of roughly $\pm 10\%$. The set of data taken using 2.5 keV Ne⁺ incident ions at various alpha values was chosen the best set in consistency and quality and as such these spectra were deconvoluted using this method. Samples of the results obtained through both fitting methods for

incident angle $\alpha=8^\circ$ are shown in Figures 6.5.1 and 6.5.2. Where the shapes of the signals corresponding to directly recoiled atoms are reasonably well understood, the same cannot be said for the broad feature that gives rise to the gentle slope on the high TOF side of the O (DR) signal. This feature is best described as multiple scattering (MS) of neon, a process that often leads to a broad low-intensity feature at longer flight times. We do not intend to use this feature for spectral intensity measurements, yet it must be accounted for in some way, as it may overlap with the oxygen or even carbon recoil signals. In order to further understand the significance of the multiple scattering feature, the entire set of spectra was fitted in two different ways. In the first method, the MS contribution to the tail was essentially ignored, and only the recoil signals were fit, with particular attention to the position and intensity of each peak's maximum. This method proved to be simple to perform, but the MS contribution to the form of the tail was considerable and it should not be completely neglected. The second method involved a full fit of the spectrum, accounting for the surface recoil signal, H, C, and O recoils, and an exponentially modified Gaussian function that reasonably fit the multiple scattering feature, allowing measurement of the important spectral intensities. The Peakfit output includes peak amplitude at the maximum, and these values were used in calculating spectral intensity ratios. Table 6.5 compares the spectral intensity ratios for the two fitting methods for 8° and 36° alpha values, and Figure 6.5.3 illustrates the variation in these ratios as α varies for both methods. Obviously, determination of any two of the ratios allows calculation of the third, but since it is useful to focus on different atoms for various illustrative purposes, all ratios will be included in the discussion.

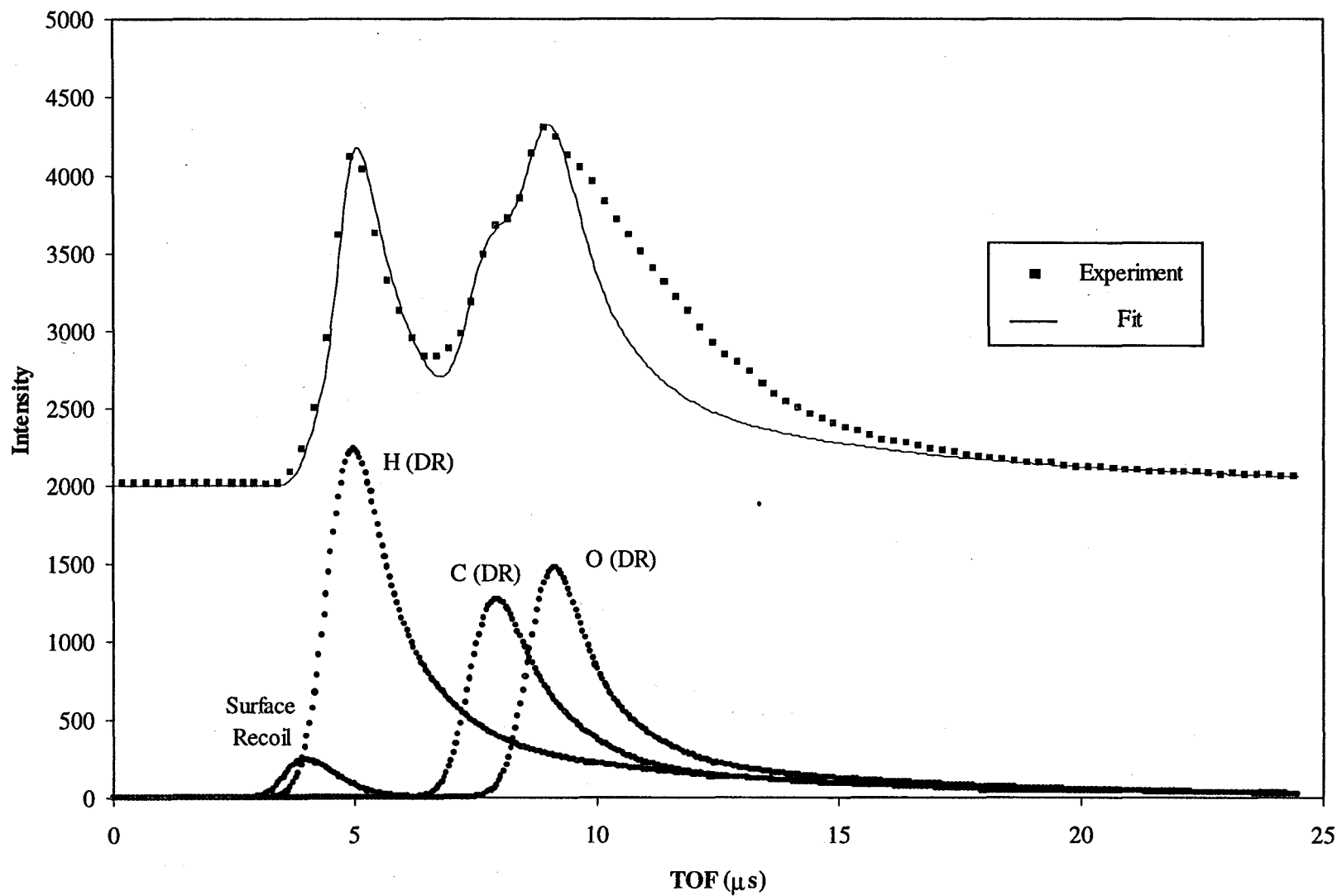


Figure 6.5.1 Deconvolution of peaks for 2.5 keV Ne^+ on glycerol, neglecting the multiple scattering tail contribution.

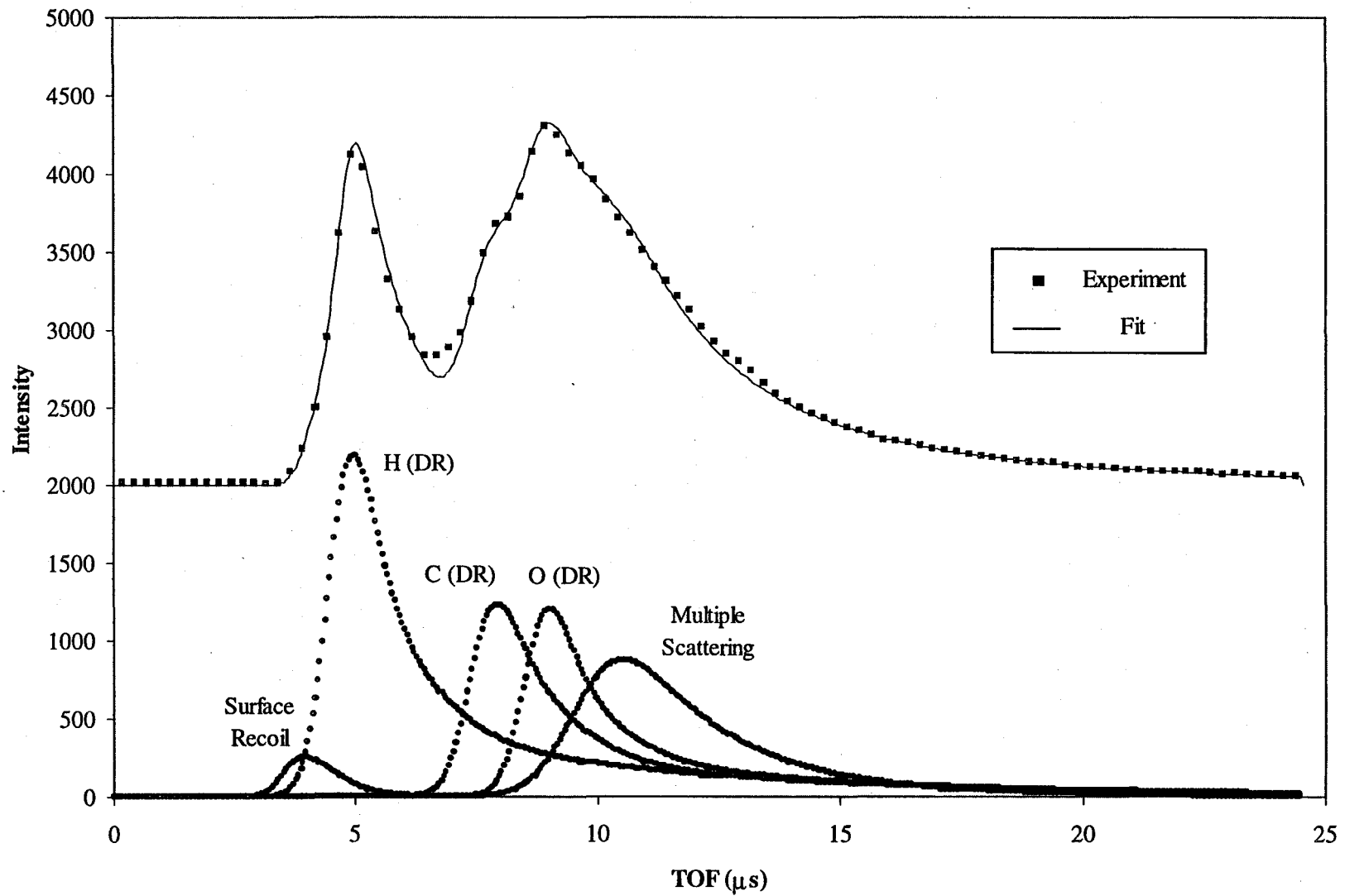


Figure 6.5.2 Deconvolution of peaks for 2.5 keV Ne^+ on glycerol, including the multiple scattering tail contribution.

An error estimate has been included in each value based on uncertainty in the deconvolutions. As could be expected, the greatest effect is seen in the oxygen recoil intensities, since the leading edge of the MS peak overlaps to some extent, lowering the H/O and C/O ratios; the H/C ratio is essentially unaffected. The first set of intensity ratios serves as a lower-limit scenario, i.e. the case in which the oxygen recoil signal is least accurately measured. Although the ratios observed are not grossly different, the intensity ratios obtained when the MS peak was included in the fit are considered to be the most reliable, and will be applied exclusively from here forward. Qualitatively, the ratios as a function of α are reasonable. The carbon and oxygen signals are of comparable intensity ($C/O \lesssim 1$), and the H/C and H/O ratios exhibit some structure, displaying local minima corresponding to the optimal geometries for C and O atoms to both recoil and exit the surface. Additionally the ratios fall within reasonable expectations based on the stoichiometry of the molecule.

6.5.2 Surface Atomic Ratios

The spectral intensity ratios obtained experimentally for glycerol were converted to surface atomic ratios in the manner described in the previous chapter. Figure 6.5.4 graphically illustrates the variation in surface atomic ratios as a function of incident angle α for both fitting methods used. These plots are similar in character to the measured intensity ratio plots, but the magnitudes of the H/C and H/O ratios are greater by about one unit after correction, due in large part to the unusually high cross section for hydrogen. The C/O ratio is an important consideration at this point.

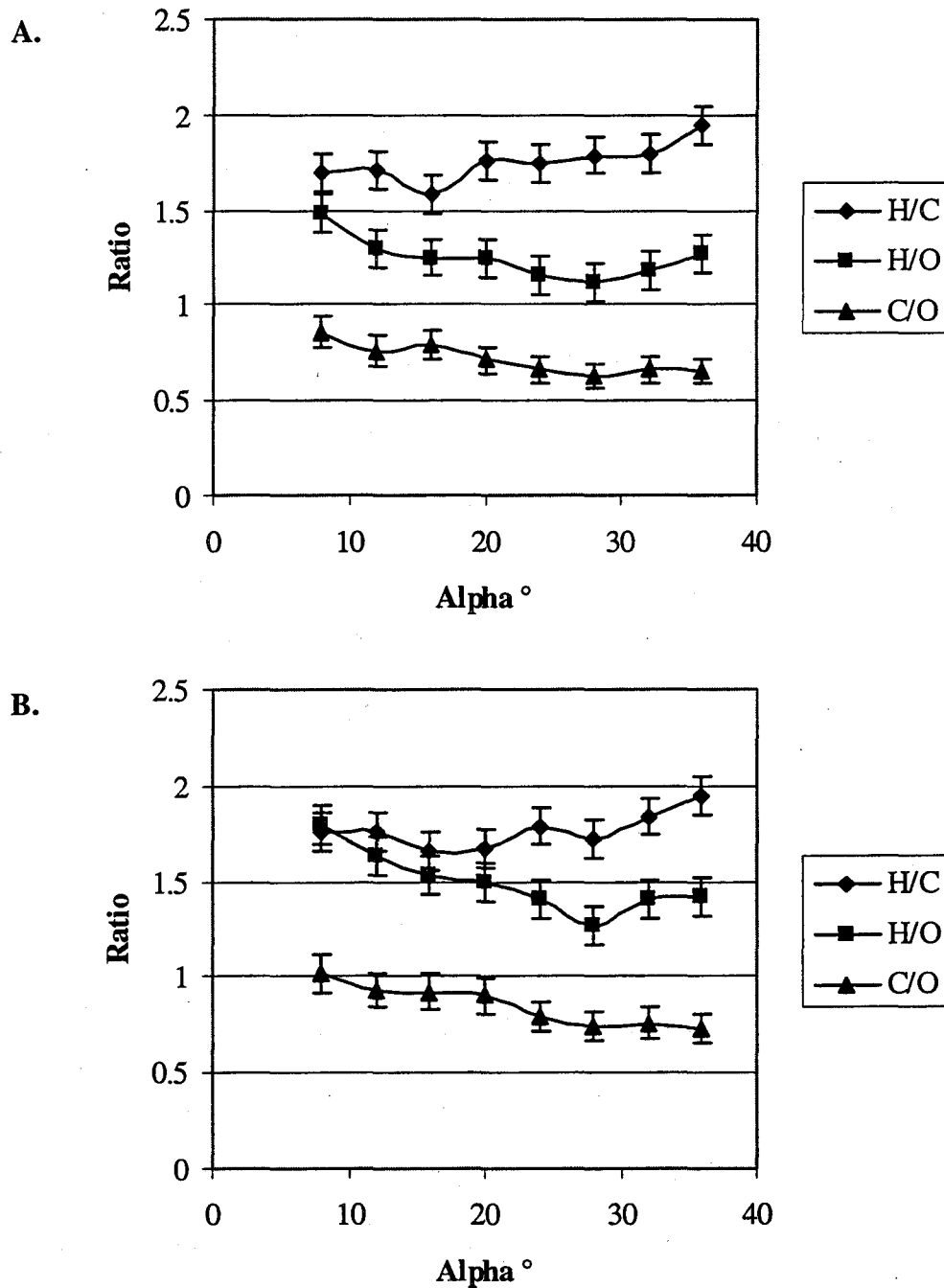


Figure 6.5.3 Experimental intensity ratios as a function of incident angle α for 2.5 keV Ne^+ incident ions. A. MS tail excluded from fit; B. MS tail included in fit.

Table 6.5 Spectral intensity ratios for glycerol (2.5 keV Ne⁺ data)

	Without MS peak fit			With MS peak fit		
α°	H/C	H/O	C/O	H/C	H/O	C/O
8	1.7-1.9	1.4-1.6	0.7-0.9	1.7-1.9	1.8-1.9	0.9-1.0
36	1.9-2.1	1.2-1.4	0.6-0.8	2.0-2.1	1.3-1.5	0.7-0.9

It is an indicator that carries more weight than the H/C or H/O ratios, for the reason that both the mass-dependent cross sections and detector responses for these two closely matched atoms are quite similar. As a result, even a gross error in the actual value of the detector responses, for example, is largely eliminated since ratios are considered rather than absolute quantities. The notion that the C/O ratio is approximately unity will be a very useful diagnostic tool in assigning the molecular orientation of glycerol at the surface.

6.5.3 Molecular Orientation Simulations

In order to determine the molecular orientation of glycerol molecules at the liquid surface, it is necessary to compare the experimental results with some reasonable possible molecular orientations and choose the most closely matching pair. The method employed here involves a computer simulation of the number of accessible atoms per molecule at the surface, as counted in a reproducible fashion. A "Line-of-Sight" simulation code (abbreviated LOS) is in development in this laboratoryⁱ for the purpose of calculating the number of atoms in a molecule that could be "seen" by incident ions for a given molecular orientation. A companion program (Rotate) allows

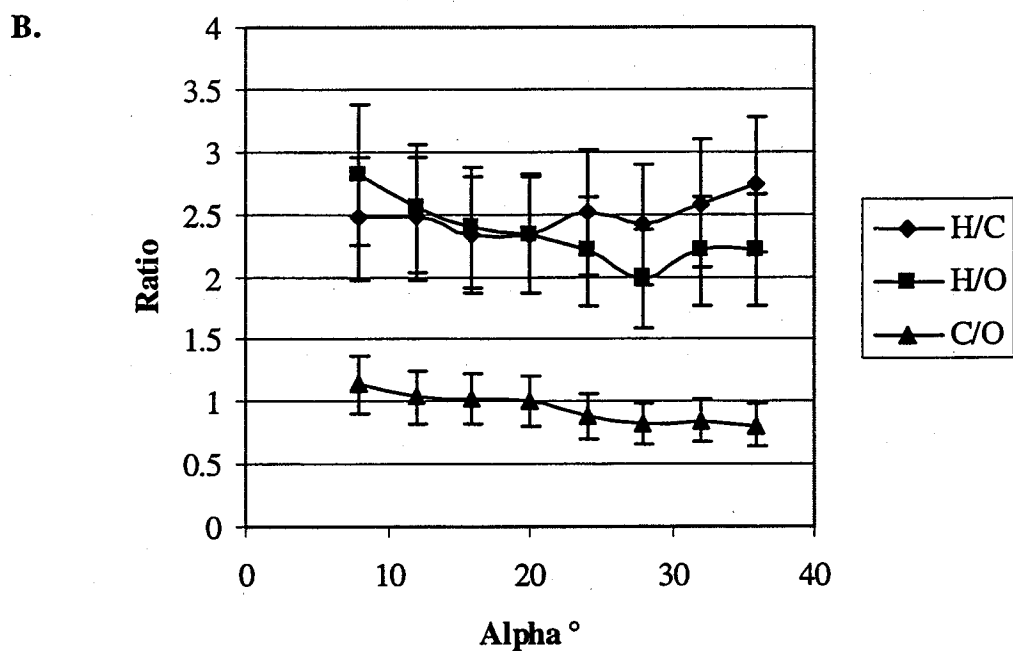
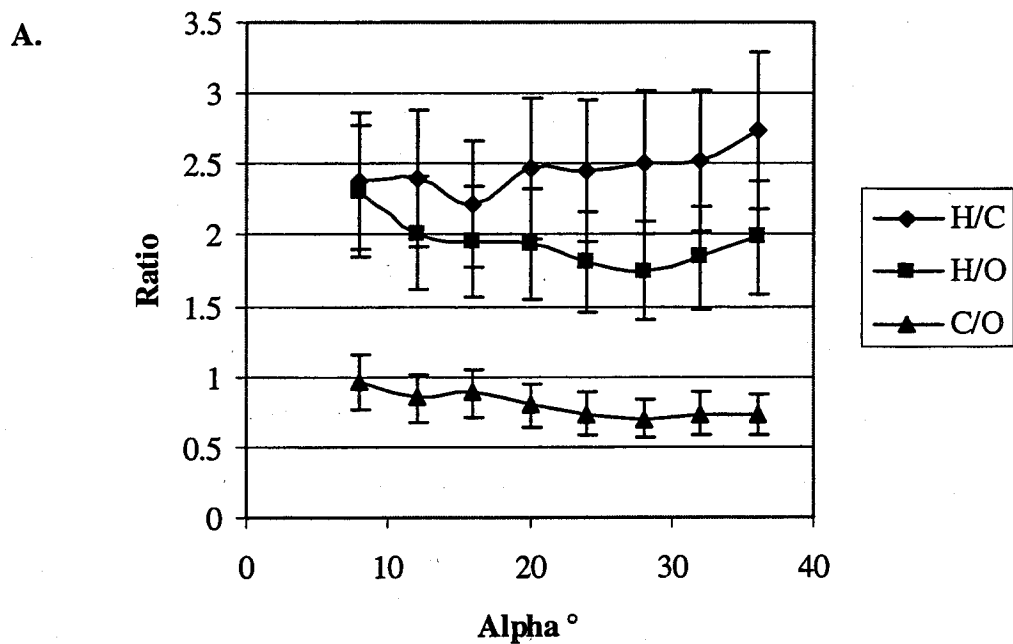


Figure 6.5.4 Corrected atomic ratios as a function of incident angle α for 2.5 keV Ne^+ incident ions.

A. MS tail excluded from fit;

B. MS tail included in fit.

for rotation of the molecule into different orientations in three dimensions. The Rotate program accepts an input file based on interatomic dimensions generated using the molecular modeling program Hyperchem™, generating a text-format output file compatible with the LOS program. The LOS simulation uses the molecular dimensions of the input file to draw an overlapping spheres representation of the molecule in the appropriate orientation, and begins to tabulate the accessible atoms over a range of azimuthal angles for a chosen incident angle α . This approach accounts for a mean intermolecular distance as well as small random vertical motions within the surface, in addition to the incident angle desired; all of these affect the probe depth and the amount of blocking of recoiled atoms as they attempt to exit the surface. The LOS simulation efficiently randomizes the direction of incidence by calculating the accessible atoms at a number of azimuthal steps, through a 360° rotation. This consideration is important because a molecule may have a dramatically different profile and/or cross sectional area when approached from different directions. The LOS output is a brief text file that gives statistical details regarding the number of atoms of each type that were encountered, the number that would actually escape the surface, and atomic ratios taken from the number of each type of atom encountered. In some orientations, especially at extreme high and low alpha values, the LOS program simulates complete blocking of a certain type of atom, usually carbon. As LOS calculates ratios of the accessible atoms, division by zero is then encountered, which would lead to infinite H/C ratios, for example. The current version of the LOS program returns the result of a division by zero as the number zero, which is a

physically nonsensical result. To avoid ambiguity in those results, the LOS simulation plots that follow have been truncated where division by zero occurred.

A model of the glycerol molecule was developed using Hyperchem™ and the geometry was allowed to optimize using the Fletcher-Reeves conjugate gradient algorithm. The goal of this exercise was to generate a reasonable structure that a glycerol molecule may assume based on intramolecular considerations. It is true that more rigorous calculations of the molecule may be more accurate in detailing liquid-phase molecular conformations, but are beyond the scope of this study. The molecular conformer chosen for first investigation was that of $\alpha\alpha$ -glycerol in the notation of Bastiansen (Bastiansen 1949). Figure 6.5.5 A. is a ball-and-stick rendering of $\alpha\alpha$ -glycerol; it should be noted that although this representation is shown here for ease of viewing, space-filling models were used in the calculations. The $\alpha\alpha$ conformer is the most stable in the liquid phase of glycerol, maximizing the amount of intramolecular hydrogen bonding and accounting for ~50% of the conformations found (Chelli, Procacci et al. 1999). Although it cannot be expected that this study could accurately differentiate between conformers, it would be interesting to also investigate a less favorable bulk conformer, with the idea in mind that the surface may behave differently than the bulk, e.g. intermolecular H-bonding may play a greater role. For this comparison the $\beta\gamma$ conformer was chosen, a conformer that may enhance intermolecular bonding at the surface (Figure 6.5.5 B.). $\beta\gamma$ -glycerol is not found to a great extent in the liquid phase, but within this study of the surface it is not significantly different from the $\alpha\gamma$ conformer, which is abundant (Chelli, Procacci et al. 1999). The difference between the two involves rotation about the C-O bond that is

deepest within the surface and is most often it is too deep within the surface to be encountered. For the purposes of this study it was chosen as a significantly different conformer than the most favorable bulk conformer with hopes of differentiating the two. One could in fact perform a large number of LOS simulations to further quantify the molecular orientation and conformation of glycerol at the surface, but the preliminary nature of this work limits the scope to an attempt to determine the gross molecular orientation.

Several possible orientations of the molecule were chosen for LOS simulation. Each orientation was simulated using a mean intermolecular distance of 5\AA , suggested by the bulk intermolecular radial distribution function $d(r)$ (Chelli, Procacci et al. 1999), over a range of incident angles matching the experimental conditions. Orientations simulated included carbon backbones parallel and perpendicular to the surface, as well as four variations involving 45° tilts away from the Z-axis in the X and Y directions. The resulting LOS outputs were tabulated, plotted and compared with the experimentally determined atomic ratios, and are detailed below. The experimental values for the C/O ratio have been added to each of the LOS plots for the purpose of direct comparison with this important indicator. For these comparisons only the experimental atomic ratios obtained using the full spectral deconvolution method are used.

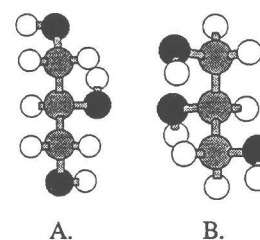


Figure 6.5.5 A. $\alpha\alpha$ -glycerol. B. $\beta\gamma$ -glycerol.

6.5.3.1 Horizontal Backbone "Out-of-Plane"

Eight orientations having a horizontal carbon backbone relative to the surface were investigated, two pairs with the carbons out of the surface plane and two pairs with the carbons in the plane. Defining the surface plane as the XY plane, the first pair of orientations has the carbon atoms all in the XZ plane and the long axis of the backbone parallel to the Y-axis (Figure 6.5.6.). The difference between the A1 and A2 orientations is a 180° rotation about the X-axis. The corresponding $\beta\gamma$ -pair is shown in Figure 6.5.7.

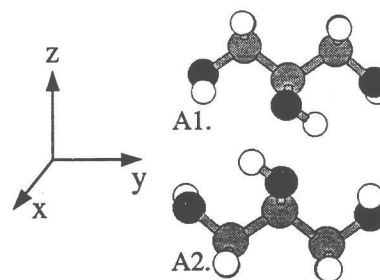


Figure 6.5.6 A1. $\alpha\alpha$ -glycerol "out-of-plane" orientation. A2. 180° rotation of A. in X.

The results of the LOS simulations for these orientations are shown in Figure 6.5.9. If primary emphasis is placed on the C/O atomic ratio, the most accurately

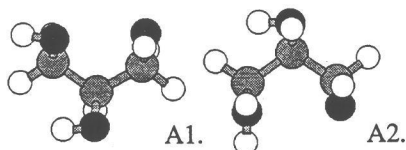


Figure 6.5.7 A1. $\beta\gamma$ -glycerol "out-of-plane" orientation. A2. 180° rotation of A1 in X.

known (≈ 1 at all values of α experimentally investigated), we can immediately rule out the orientation shown in A, which at ~ 2.0 is too high.

This surface has approximately CH_2 stoichiometry at all α . In the B. ratio plot, the C/O ratio is significantly lower than experimental

(≤ 0.63), and the H/C ratio is generally higher than expected, ruling this orientation out.

In Figure 6.5.8 C. and D. the LOS results for the corresponding orientations for the $\beta\gamma$ -glycerol conformer are illustrated. Again using the C/O ratio as the most

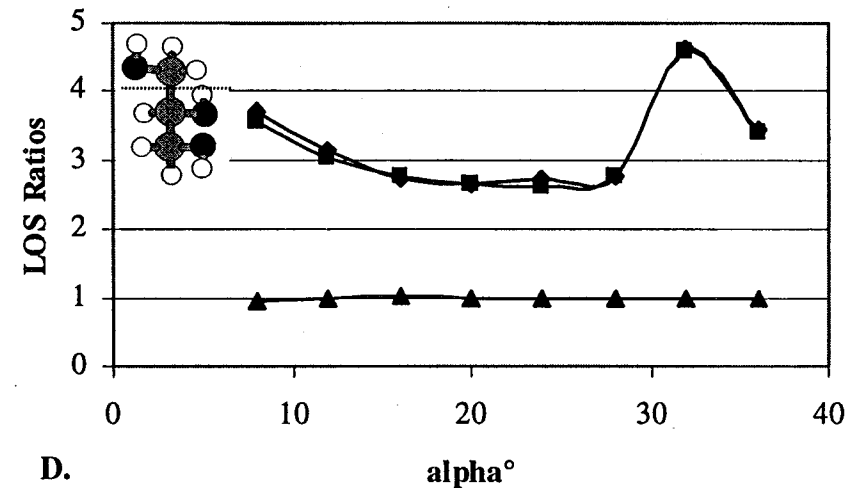
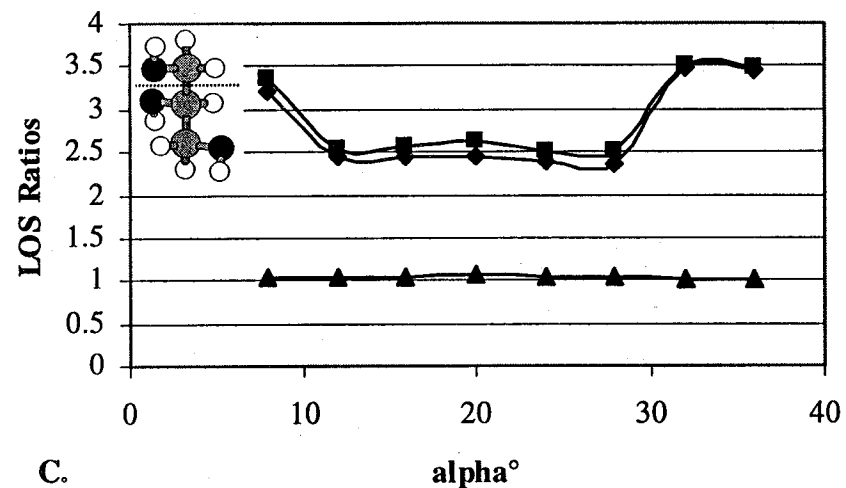
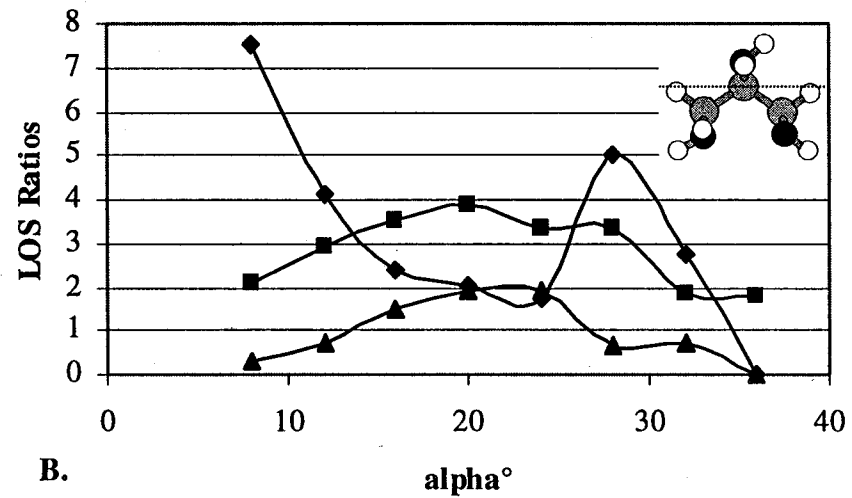
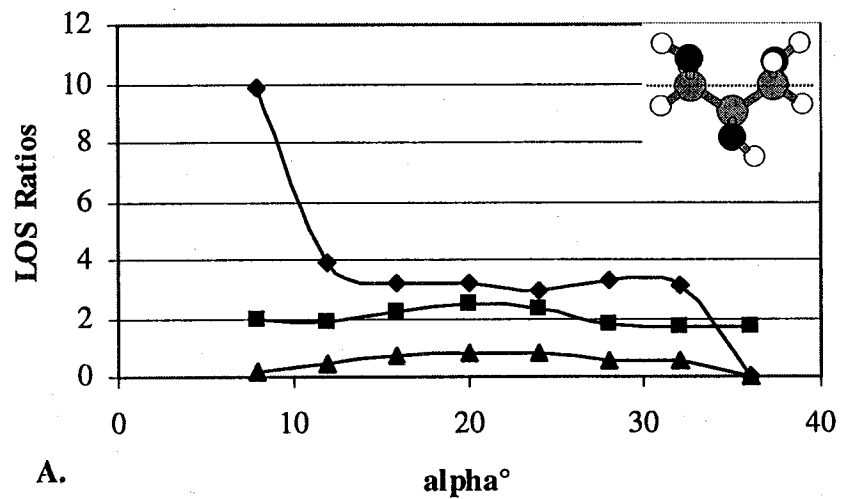


Figure 6.5.8 Calculated LOS atomic ratios as a function of α . A. and B. Horizontal backbone. C. and D. Vertical backbone.
 Legend: ♦ = H/C, ■ = H/O, ▲ = C/O.

stringent test, it is seen that neither of these orientations can be the correct one. The orientation illustrated in C. shows the C/O ratio as too low at all α , reaching 0.79 at the maximum. The H/C ratio is slightly high (~ 3.0) at intermediate α values and the behavior at the extremes is due to complete blocking of carbon atoms. The configuration of Figure 6.5.8 D. displays quite erratic behavior of all the calculated ratios. In this case the C/O ratio displays a broader range of values, from nearly zero at the extremes to almost 2.0 at intermediate α values. The structure in the C/O curve suggests that the true orientation cannot involve this horizontal “out-of-plane” backbone structure, as we expect a fairly constant trace. The H/C ratio exhibits similar behavior to the “B” orientation, particularly at high and low alphas, and further exclude this orientation as a possibility.

6.5.3.2 Horizontal Backbone “In Plane”

Figure 6.5.9 illustrates the pair of orientations corresponding to $\alpha\alpha$ -glycerol molecules with all three carbon atoms lying in the X-Y (surface) plane and differ by a 180° rotation about the X-axis. The analogous pair of orientations arising from the $\beta\gamma$ -conformer is given in Figure 6.5.10. LOS calculations resulting from these four input orientations are shown in Figure 6.5.11.

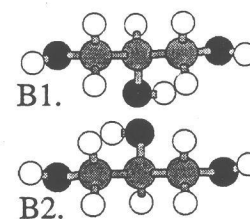


Figure 6.5.9 $\alpha\alpha$ -glycerol orientations with “in-plane” carbon backbones.

Inspection of the plot of LOS ratios vs. α for the orientation presented in Figure 6.5.11 A. reveals a favorable comparison of the C/O ratios, which are close to one at all values of α . The argument could be made that the C/O ratio decreases slightly over the range

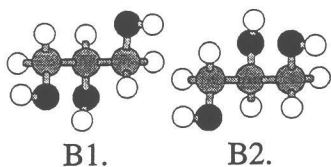
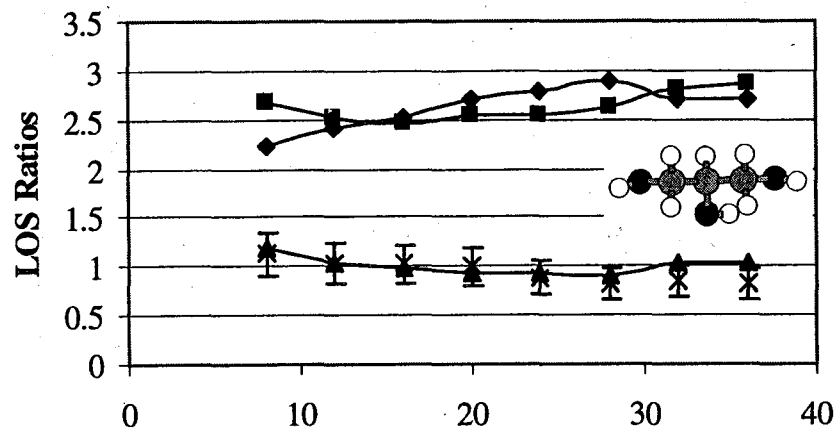


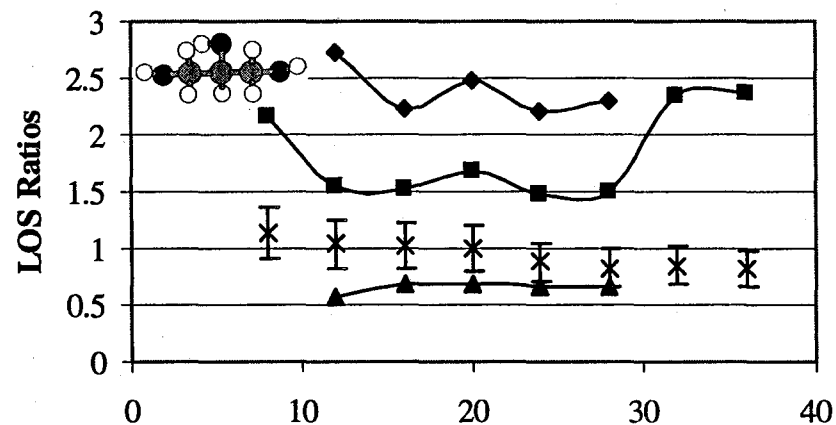
Figure 6.5.10 “In-plane” horizontal orientations of $\beta\gamma$ -glycerol.

of α investigated, whereas the LOS ratio increases slightly at high α , but within the limits of experimental error this is inconclusive. The H/C and H/O ratios also compare reasonably well with the experimental values, with the exception of the shape of the curves. The experimental C/H and H/O curves are concave and have local minima below 2.5. This orientation would also make physical sense, with a reasonable compromise between intermolecular and intramolecular hydrogen bonding.

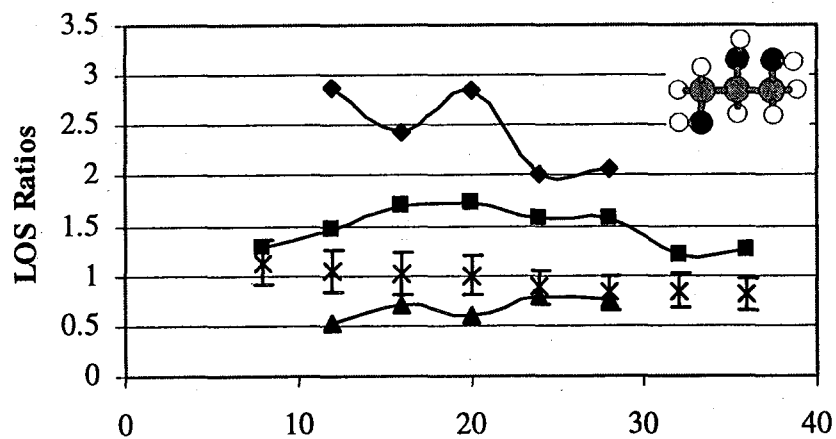
Figure 6.5.11 B. illustrates the LOS ratios calculated for the complementary in-plane backbone orientation. This orientation would be intuitively less favorable, with a more free hydroxyl group oriented outward. The LOS ratios calculated support this reasoning, particularly in the C/O ratio which never gets close to the expected value of one. The H/C ratios are reasonable but the H/O ratios are consistently low at the important intermediate α values. This orientation is very unlikely to be the correct one. Considering the horizontal in-plane orientations of $\beta\gamma$ -glycerol, we can rule out the orientation of Figure 6.5.11 C. based on the low C/O ratio, a result of the two oxygen atoms oriented outward. This orientation would be unlikely as it limits H-bonding with the bulk layer below. The H/O ratio, though not the best indication, is also lower than expected. Figure 6.5.11 D. gives the corresponding $\beta\gamma$ - orientation with two hydroxyls downward, and it too suggests an unlikely configuration. The C/O ratio is nearly one at some intermediate values, but rises to over 1.5 at high α , an unexpected behavior. The H/C ratio is lower than the experimental for most α , reaching 2.5 at $\alpha = 20^\circ$ only. The H/O ratios reach values that are too high at high



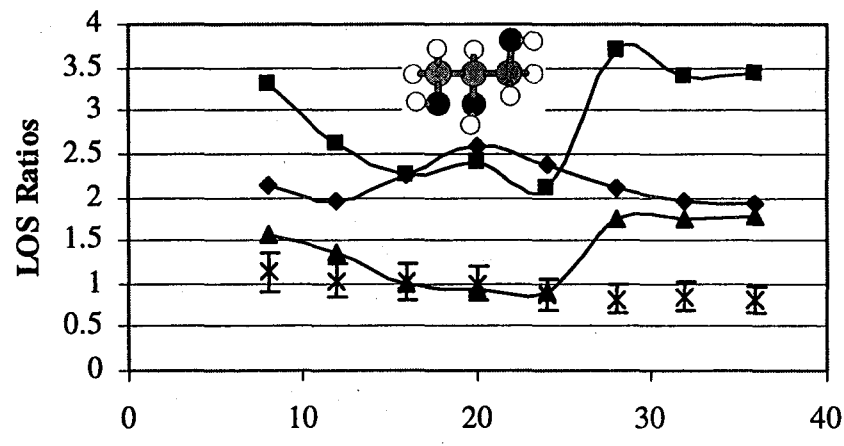
A. α -glycerol



B. α -glycerol



C. β -glycerol



D. β -glycerol

Figure 6.5.11 LOS atomic ratios for horizontal "in-plane" glycerol orientations as a function of α . A. and B. α -glycerol. C. and D. β -glycerol. Legend: \blacklozenge = H/C, \blacksquare = H/O, \blacktriangle = C/O, \times = experiment C/O.

alphas as well. It can be concluded that neither of these $\beta\gamma$ in-plane configurations is acceptable.

6.5.3.3 Vertical Backbone

Four orientations of the glycerol molecule that involve the long axis of the carbon backbone along the Z axis, perpendicular to the surface plane, were considered. The first two are illustrated in Figure 6.5.12 and are a pair of $\alpha\alpha$ -conformers of the molecule. The two are identical except that in C2 the β -hydroxyl hydrogen has been rotated

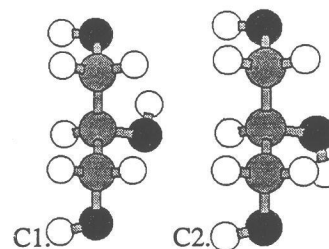


Figure 6.5.12 $\alpha\alpha$ -glycerol in vertical orientations. C1. b-hydroxyl H upward. C2. b-hydroxyl H downward.

downward relative to the surface. This was done with the intent of investigating the

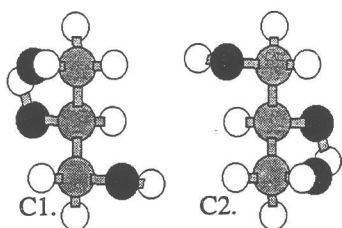


Figure 6.5.13 $\beta\gamma$ -glycerol in vertical orientations. C1. b-hydroxyl H upward. C2. b-hydroxyl H downward.

effect of rotation about the C-O bond on the H/C ratio, and the C/O ratio should be relatively unaffected. The complementary pair of $\beta\gamma$ conformers is illustrated in Figure 6.5.13. It should be noted that the $\beta\gamma$ - pair of

conformers have been modified in a slightly different way; in order to preserve intramolecular H-bonding the molecule has been rotated 180° in X. In

comparing the plots in figure 6.5.14 A. and B., it is seen that the H/C and H/O ratios are somewhat higher in the conformer in A., reasonably so as the middle hydroxyl H is rotated upward. In A., the H/O ratio exhibits a broad range of values, from about 0.5 to 2.5 at the maximum, a behavior unlike the experimental observation.

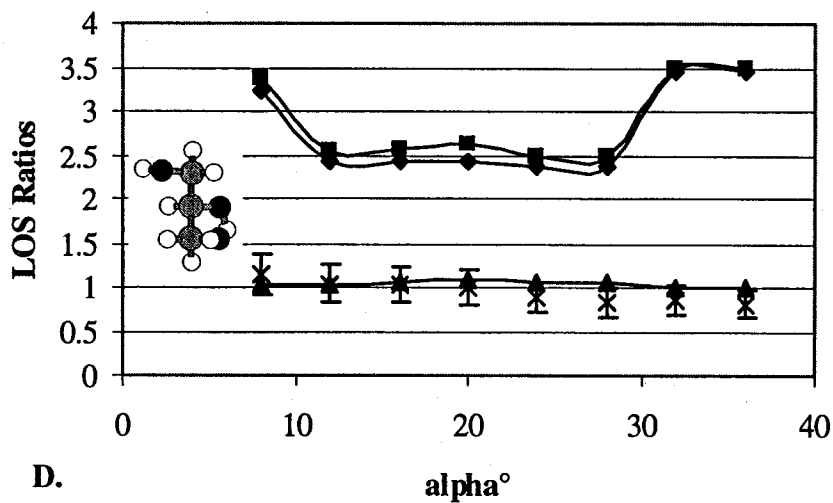
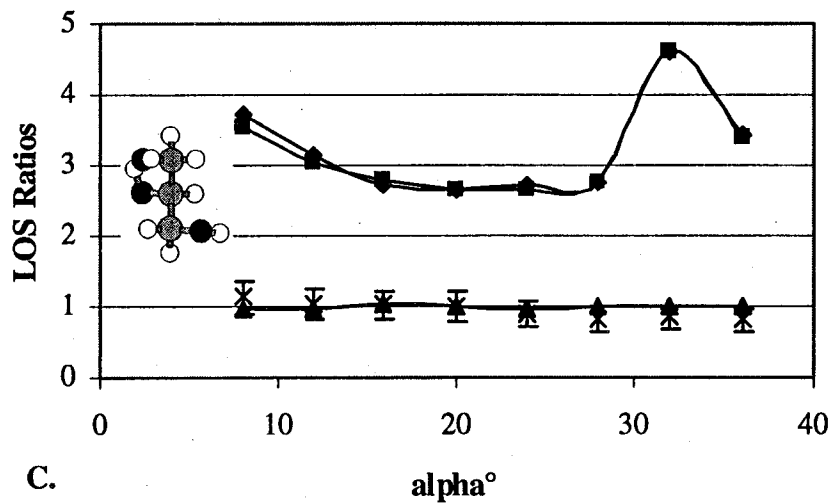
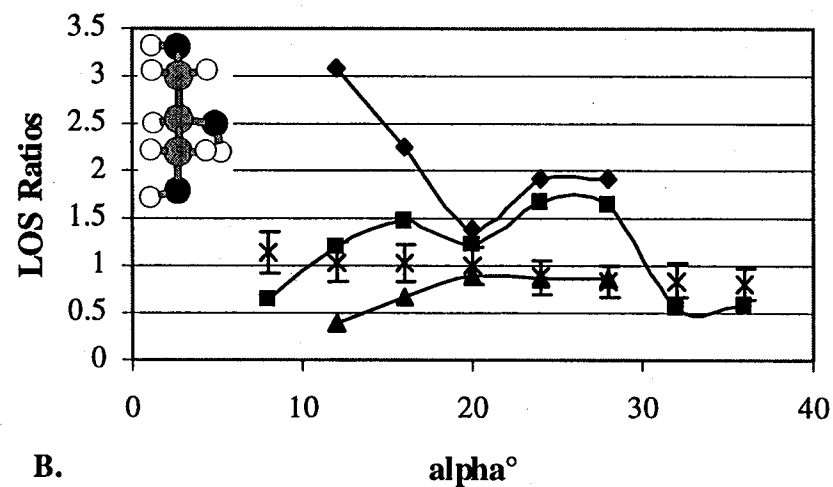
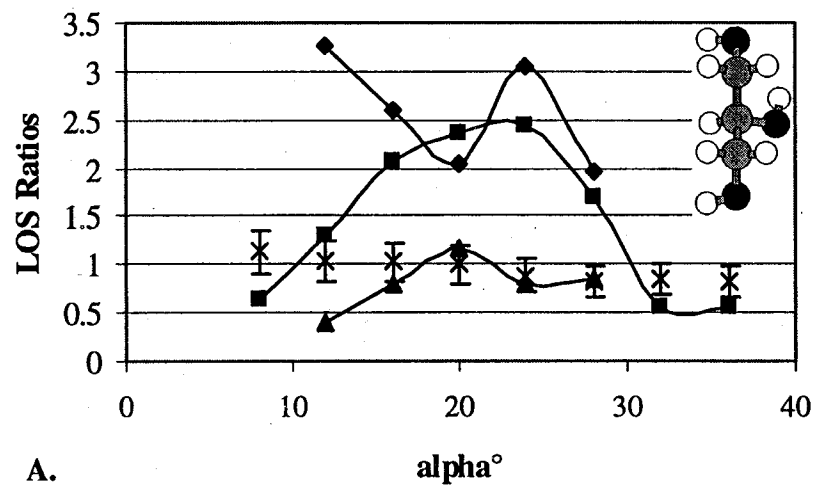


Figure 6.5.14 LOS atomic ratios for vertical glycerol orientations as a function of α . A. and B. $\alpha\alpha$ -glycerol, β -hydroxyl H up and down respectively. C. and D. Analogous figures for $\beta\gamma$ -glycerol. Legend: ◆ = H/C, ■ = H/O, ▲ = C/O, x = experiment C/O.

The C/O ratios in both A. and B. show similar curvature, somewhat low at lower α and reaching values near unity at intermediate to high alphas. Significant blocking of carbon atoms truncates the data series involving carbon at the extremes in both A. and B. Based on the C/O ratios alone, these $\alpha\alpha$ -vertical conformers may fall within the error limits of the experiment but the H/C and H/O ratios are not very favorable.

Considering the $\beta\gamma$ conformer LOS plots in Figure 6.5.14 C. and D., the C/O ratios in both are in excellent agreement with the experimental values at ≈ 1.0 for all α values investigated. In light of this, these orientations should be considered as good candidates for the correct orientation with less emphasis placed on the agreement of the other ratios. The H/C and H/O ratios are quite similar in all cases since the C/O ratio is close to one, and agree with the experimental ratios at intermediate α values but are slightly high at the extremes. With this in mind, the vertical orientation of $\beta\gamma$ -glycerol as simulated should be strongly considered as the correct surface orientation.

6.5.3.4 Backbone Tilted from Vertical in Y-Direction

Without a definitive previously reported determination of whether the glycerol backbone is oriented vertically, horizontally, or at some intermediate angle, it was reasonable to investigate a series of orientations rotated from the vertical and horizontal possibilities. Ideally a range of angles between vertical and horizontal orientations would be investigated, and this may be reserved for future study. Computer processing resources limit this work to the investigation of one angle in particular. It was decided that the first angle of choice should be midway between the two options investigated,

or a 45° rotation from the Z-axis. This rotation was done in both the Y direction and the X direction and these will be treated separately.

In the case of both the $\alpha\alpha$ and $\beta\gamma$ conformers of glycerol a single molecular conformation in terms of bond rotations was chosen and then rotated 45° in both the clockwise and counter-clockwise directions in the Y-Z plane. Ball-and stick renderings of these rotated conformations are given in Figure 6.5.15 ($\alpha\alpha$) and 6.5.16

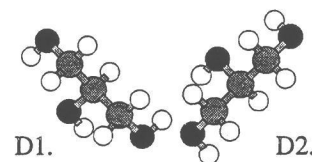


Figure 6.5.15 $\alpha\alpha$ -glycerol tilted in Y. D1. 45° CCW from vertical. D2. 45° CW from vertical.

($\beta\gamma$). There should be obvious differences in the values of the C/O ratios in each pair. The simulated atomic ratios generated by LOS are plotted in Figure 6.5.17.

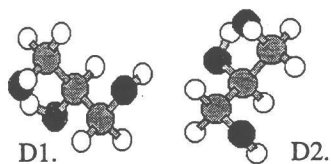


Figure 6.5.16 $\beta\gamma$ -glycerol tilted in Y. D1. 45° CCW from vertical. D2. 45° CW from vertical.

Examination of the C/O ratios of figure 6.5.17 A., the range of values calculated is a bit erratic, though not entirely far from the experimental values except at $\alpha = 28^\circ$ where the value is ~ 1.3 . The trend seen is somewhat discouraging at lower α . The H/C and H/O ratios are also somewhat scattered, particularly the H/C ratio, which has a minimum of 1.6 and a

maximum of 3.5. The ratios calculated in B. can be discounted immediately due to the low C/O ratio, an expected result due to the additional accessible oxygen.

The $\beta\gamma$ orientations simulated in C. and D. of Figure 6.5.17 give some interesting atomic ratios. While the C/O ratios in the first case are acceptable at some intermediate α values, the sharp difference at $\alpha = 8^\circ$ is indicative that this is probably

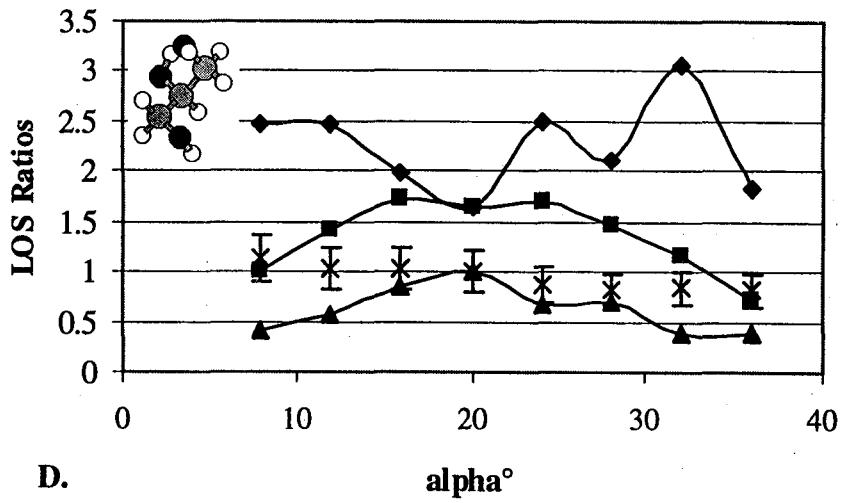
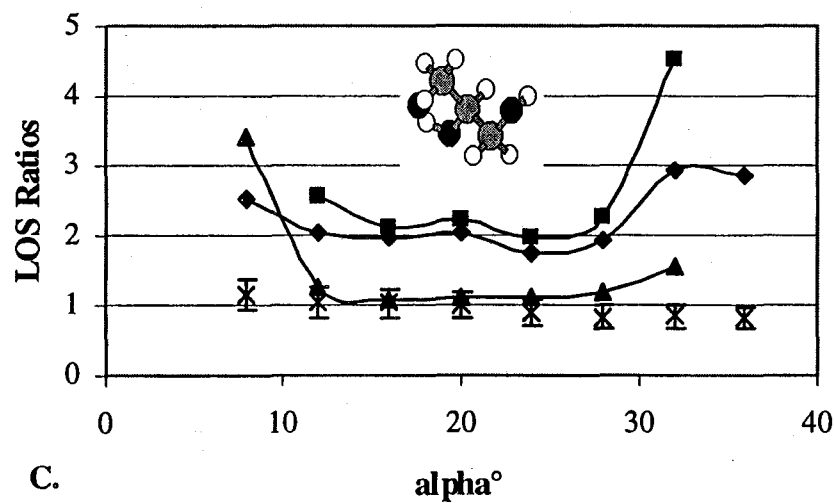
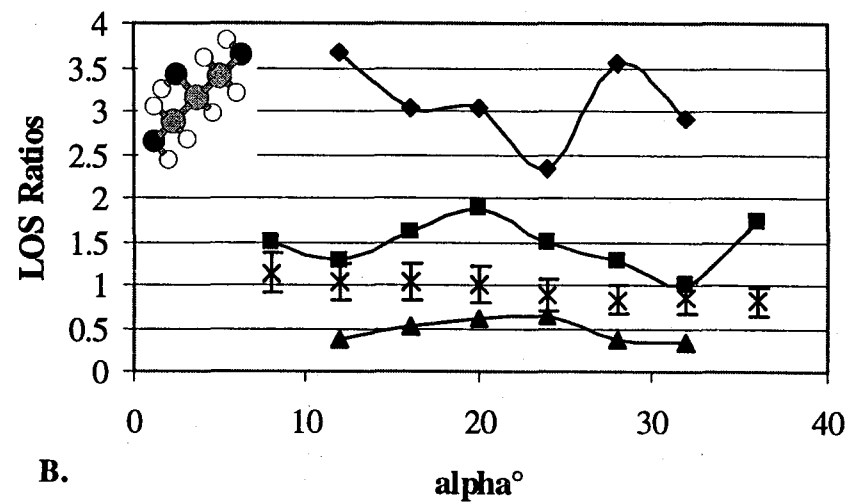
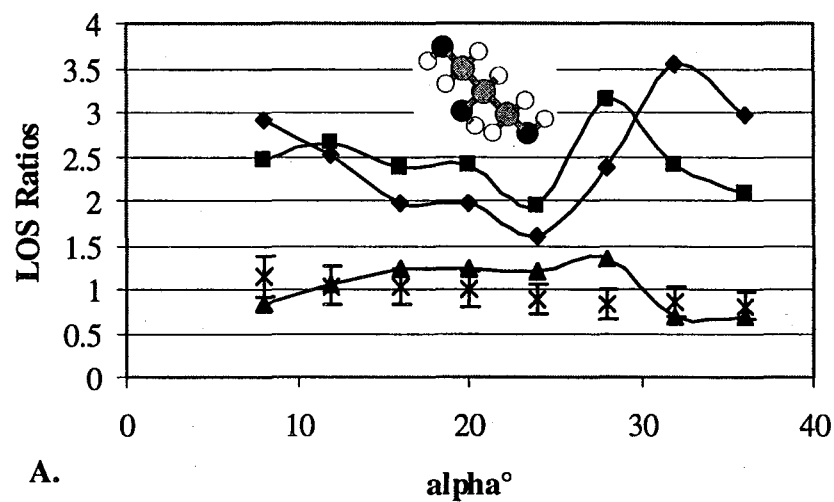


Figure 6.5.17 LOS atomic ratios for backbone orientations tilted in Y as a function of α . A. and B. $\alpha\alpha$ -glycerol, 45° CCW and CW respectively. C. and D. Analogous figures for $\beta\gamma$ -glycerol. Legend: \blacklozenge = H/C, \blacksquare = H/O, \blacktriangle = C/O, x = experiment C/O.

not the best choice. The H/C and H/O ratios support this finding as they are somewhat low at several of the intermediate alphas. The curvature exhibited in the C/O trend of the D. plot, as well as the generally low values, suggest that this is an unlikely orientation as well. Although the H/C ratio is scattered, it remains almost centered around the expected value of ~ 2.5 ; however, the H/O ratios do not support this orientation as the one observed experimentally.

6.5.3.5 Backbone Tilted from Vertical in X-Direction

The final set of glycerol orientations simulated involves 45° tilts away from the Z-axis in the X-Z plane. For ease of viewing, the diagrams presented here are from the perspective of the Y-axis, whereas the previous images have all been looking along the X-axis. Figure 6.5.18 presents the $\alpha\alpha$ - conformer rotations, and the corresponding $\beta\gamma$ -

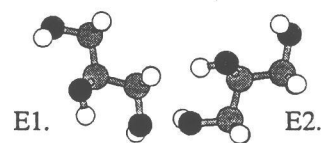


Figure 6.5.18 $\alpha\alpha$ -glycerol tilted in X. E1. $+45^\circ$ from vertical. E2. -45° from vertical.

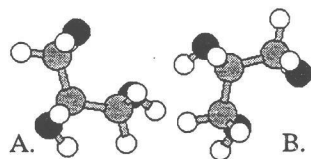


Figure 6.5.19 $\beta\gamma$ -glycerol tilted in X. A. $+45^\circ$ from vertical. B. -45° from vertical.

glycerol rotations are given in Figure 6.5.19. The LOS simulation results for these rotated forms of the molecule are depicted in Figure 6.5.20.

In Figure 6.5.20 A., the C/O ratio trace exhibits some reasonable behavior at shallow and steep incident angles, but reaches a maximum of ~ 2 at $\alpha = 24^\circ$, an undesirable result. The H/C ratio has

nearly the correct trend but appears to cover too broad a range of values, and the H/O ratio has not only the inverse curvature that is expected, but an anomalous high value near 4.5 also at 24° . This scenario is unlikely as a candidate for the correct orientation. In the figure for the opposite rotation (B.), the data is limited by severe blocking of the carbon atoms, as could be expected from the outward location of oxygen atoms. Here, the H/O ratio nearly follows the 1:1 trend expected for C/O, a signal that hydroxyl hydrogens are likely those observed. The inset figure of this orientation supports all of these indications, and it is highly unlikely that this configuration is correct based on the simulation.

The $\beta\gamma$ - rotation shown in Figure 6.5.20 C. depicts C/O ratios that are generally low, and truncated at the high end by blocking of carbon atoms, but this is still not the worst fit seen. Ratios calculated for H/C at the surface are quite scattered, but may result from partial blocking of carbon, which also contributes to the low C/O ratios. The H/O ratios calculated fall within reasonable limits but are not convincing when considered with the C/O ratios. The last plot in Figure 6.5.20 is quite interesting. Calculated C/O ratios are reasonable at all α except 20° , and that value is only slightly higher than the experiment. Although the H/C ratios appear somewhat high, they exhibit the expected trend, as do the H/O ratios. The H/O ratios show a trend very like the experiment as well, only being slightly high at the upper end of the α values investigated. This orientation should remain among those considered for the best possible orientation.

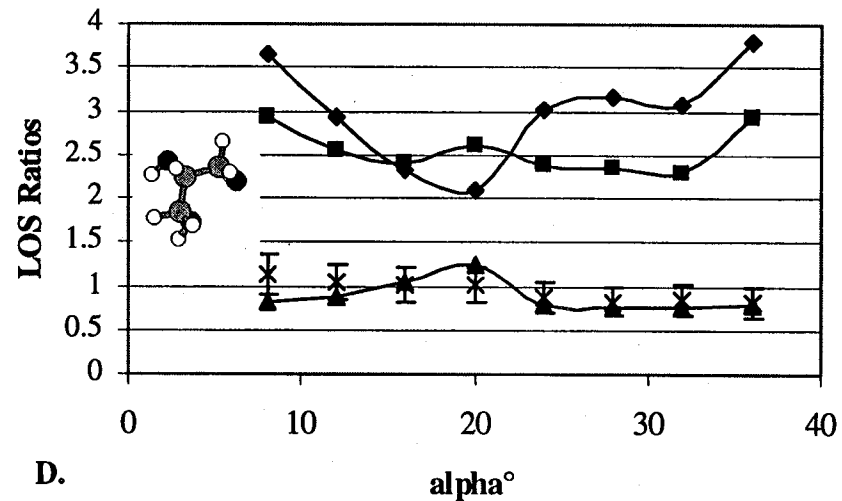
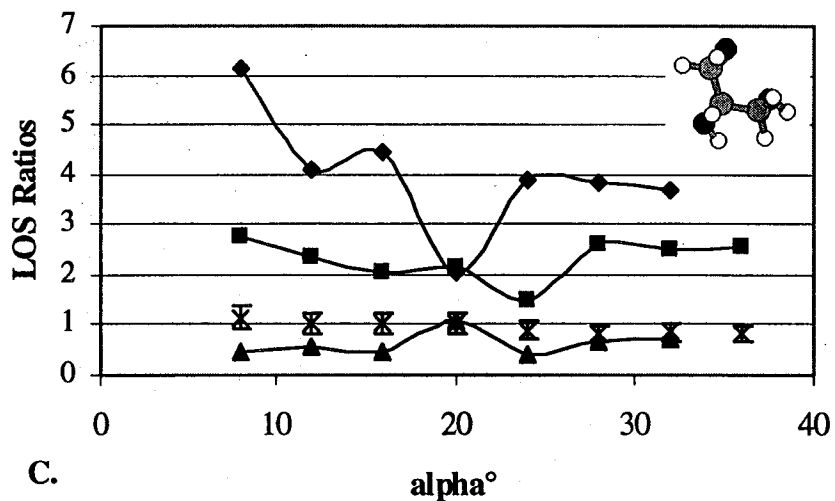
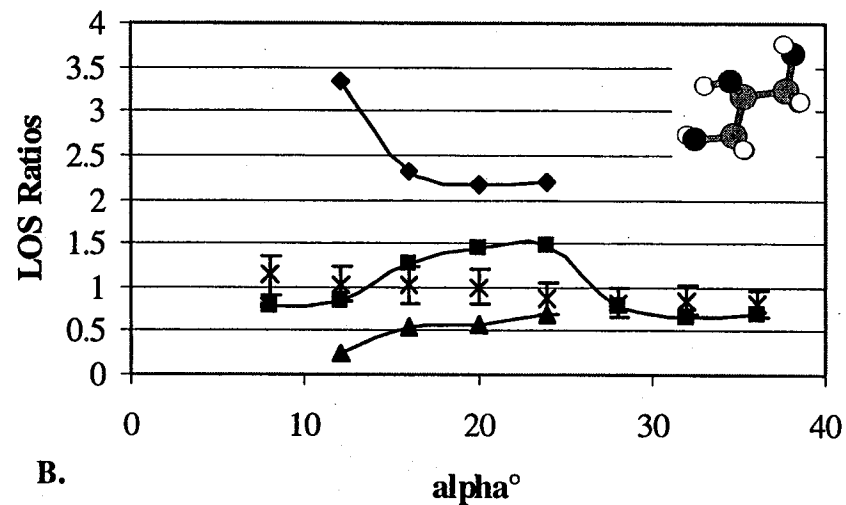
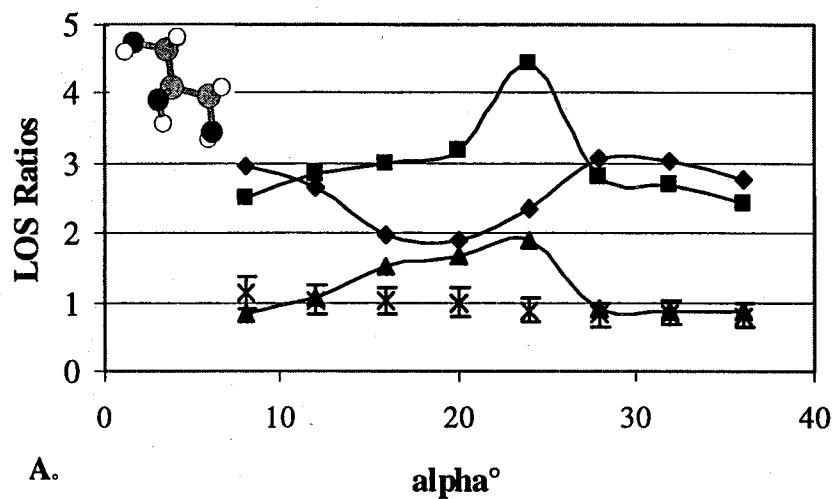


Figure 6.5.20 LOS atomic ratios for glycerol orientations tilted in X as a function of α . A. and B. $\alpha\alpha$ -glycerol, $+45^\circ$ and -45° respectively. C. and D. Analogous figures for $\beta\gamma$ -glycerol. Legend: \blacklozenge = H/C, \blacksquare = H/O, \blacktriangle = C/O, x = experiment C/O.

6.5.4 Quantitative Comparison of C/O Ratios

Throughout the discussion the greatest emphasis in deciding which is the most accurate determination of the surface orientation of glycerol has been placed on the ratio of C to O atoms. Comparisons have been made visually between the LOS simulations and the experimentally determined values, but a more rigorous comparison should be made. The comparison that follows involves calculation of the average deviation s of the LOS-derived C/O ratios from the experimental values. In order to best determine the deviation, the differences between the simulation and experiment were computed at each incident angle that was probed, and the average of these differences were taken for each orientation. Negative and positive deviations were handled in the same way by application of the formula

$$s = \frac{\sqrt{\sum_{\alpha=8}^{36} \left(\frac{H}{C}_{\text{EXPT}} - \frac{H}{C}_{\text{LOS}} \right)^2}}{n} \quad 6.4$$

In each case the appropriate value of n was used, recalling that although eight values of α were probed for each orientation, but not all LOS α -values were reliable. The resulting deviations are listed in Table 6.6 for direct comparison. The orientations in Table 6.5 having the lowest average deviation from the experimental C/O ratio are denoted by asterisks. Of the $\alpha\alpha$ -conformer orientations, the B1 horizontal in-plane orientation having a hydroxyl group above the plane has the lowest of all average deviations, 0.11. Within close proximity are the two vertical orientations C1 and C2 of the $\beta\gamma$ -conformer that differ only by rotation of the middle hydroxyl hydrogen.

Table 6.6 Average deviations between LOS and experiment C/O ratios

Orientation (Figures)	$\alpha\alpha$ Avg. Deviation	$\beta\gamma$ Avg. Deviation
A1 (6.5.6/6.5.7 A.)	1.18	0.33
A2 (6.5.6/6.5.7 B.)	0.43	0.60
B1 (6.5.9/6.5.10 A.)	*0.11*	0.60
B2 (6.5.9/6.5.10 B.)	0.29	0.29
C1 (6.5.12/6.5.13 A.)	0.31	*0.13*
C2 (6.5.12/6.5.13 B.)	0.34	*0.14*
D1 (6.5.15/6.5.16 A.)	0.28	0.91
D2 (6.5.15/6.5.16 B.)	0.65	0.39
E1 (6.5.18/6.5.19 A.)	0.51	0.43
E2 (6.5.18/6.5.19 B.)	0.52	0.17

Figure 6.6.1 illustrates these plausible orientations. The plot given in Figure 6.6.2 allows comparison of the experiment and simulation as a function of α . Note that the scale has been expanded to give a better perspective on the traces, but the experimental error bars are the same magnitude as in all the previous LOS plots. Based on this analysis it is difficult to definitively choose between the orientations; however, this is at least as accurate as any experimental assessment.

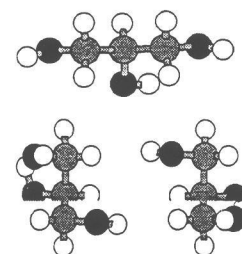


Fig. 6.6.1 Plausible orientations of glycerol. A. $\alpha\alpha$ in-plane; B. and C. $\beta\gamma$ - vertical.

6.6 Conclusions

The TOF-SARS experiments performed on the glycerol surface provide information regarding the ratios of accessible H, C, and O atoms in the top layer of the

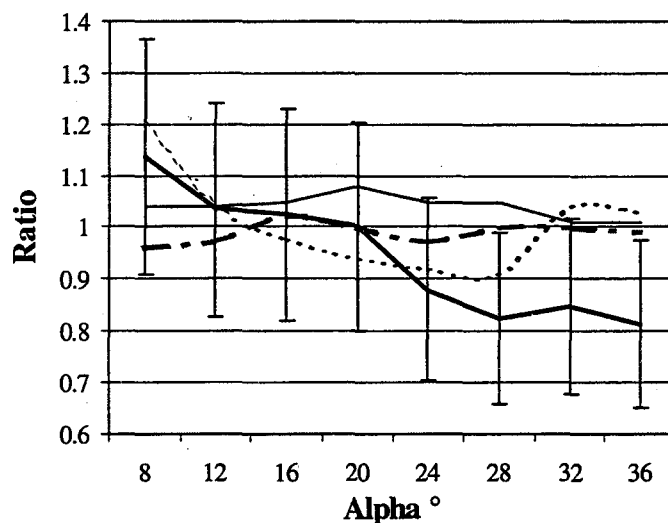


Figure 6.6.2 Comparison of the experimental C/O ratio with the closest LOS-simulated C/O ratios. Legend: — experiment, $\alpha\alpha$ -horizontal in plane, — $\beta\gamma$ -vertical, β -hydroxyl H upward, $\beta\gamma$ -vertical, - - β -hydroxyl H downward.

surface. These ratios can be compared to the accessible atomic ratios calculated by a computer algorithm that counts the accessible atoms in a molecular surface via a “line-of-sight” approach. Comparison of the experimental and theoretical data leads to more than one possible orientation, a consequence of several contributing factors, including:

- The symmetrical nature of the glycerol molecule, leading to more than one orientation exhibiting similar accessible atomic ratios;
- A lack of information on the conformational composition at the liquid surface. Two conformers were chosen, but six variants are possible, and other evidence is unavailable;
- Experimental uncertainty limitations;
- Possible shortcomings of the LOS simulation routine (recall that this program is currently still in development) leading to inaccuracies in the accessible atomic ratios.

At this time it is not possible to select the single best orientation over all others, but significant strides have been made toward differentiating between dissimilar orientations for two conformers of glycerol. The best choices for the possible surface orientations of glycerol at the liquid-vacuum interface include the $\alpha\alpha$ -conformer with all three carbon atoms in the plane of the surface and the β -hydroxyl group downward and vertical orientations of the $\beta\gamma$ -conformer. The findings are reasonably consistent with molecular dynamics simulations in which carbon and oxygen populate the surface nearly equally (Benjamin, Wilson et al. 1994; Benjamin, Wilson et al. 1995) and may lend support to preliminary observations using the sum frequency generation, suggesting a vertical backbone or a slightly tilted orientation (Shultz 1999). Further experiments could potentially make use of deuterated glycerol to differentiate the hydroxyl hydrogens from the methylene hydrogens, and this approach is in progress in a follow-up SFG study. After becoming involved with the LOS simulations it appears that much more effort could be expended toward simulating many conformers and varying C-O bond rotations to effect the positions of hydroxyl hydrogens. A better understanding of the quantitative capabilities of the technique is necessary for more detailed work in this area.

ⁱ Philip R. Watson, author; © 1999.

7. TOF-SARS Investigation of a Room-Temperature Ionic Liquid Surface

7.1 Introduction

An interesting class of materials categorized as ionic liquids is gaining attention in the search for an alternative to volatile organic solvents, a movement toward “clean technology” (Freemantle 1998). Ionic liquids (ILs) have been documented for some 40 years, but their applications and properties have been the subject of several more recent studies dating from the early 1980s (Hussey 1988). At moderate temperatures, these binary salts are actually molten and the cation and anion have been carefully selected to provide this desired property. They are sometimes referred to as “neoteric solvents” in order to escape the prevailing conception associated with molten salts (Seddon 1997). A more detailed review of ILs can be found in print (Seddon 1997) and on the World Wide Web (Seddon 1997).

Ionic liquids possess quite unusual chemical and physical characteristics, including high solvation capacities, adjustable acidity, highly selective catalysis, negligibly small vapor pressures, and broad liquid temperature ranges. All of these properties add to the usefulness of ionic liquids for industrial applications; the most vital of these to our research is the aspect of low vapor pressure, coincidentally the property that makes ILs so environmentally friendly. An added interesting facet is that the atomic compositions of many of these materials include atoms such as chlorine, fluorine, and phosphorus in relatively high stoichiometric ratios. While several current investigations involve catalytic properties of ILs, our studies are the first of any kind to gain further understanding of their surface behavior. Ionic liquids are generally clear and colorless,

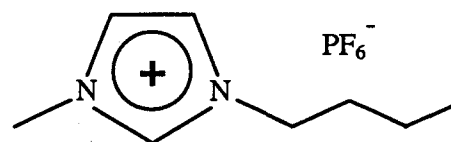
easily handled, non-corrosive, low-viscosity liquids at room temperature. Some IL variations are air sensitive and/or hygroscopic, especially those with chloroaluminate anions; the hexafluorophosphate sample considered here is stable to both.

The major objective of this work is to gain insight into IL surface composition, i.e. whether the outermost layer contains primarily cations, primarily anions, or a mixture of the two. Additionally, we intend to gain orientational knowledge of the ions present, information that would be beneficial in understanding catalysis processes occurring at the interface. The interfacial chemistry is particularly important in two-phase homogeneous catalysis processes, an area of great interest for IL use (Chauvin and Olivier-Bourbigou 1995). In such processes, one phase (the IL) solvates the catalyst, and an immiscible organic phase contains the reactant and product species. It is obvious that the reaction takes place directly at the interface, and the reaction rate depends strongly on both the access of the catalyst to the interface as well as the transfer of material across the interface. At this time a greater knowledge of the makeup of the IL interface would greatly benefit the overall understanding of these catalysis reaction processes.

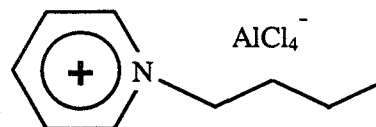
7.2 Bulk Chemistry of Ionic Liquids

The composition of ionic liquids generally consists of an organic cation and an inorganic anion; two examples of common ILs are given in Figure 7.2.1. The cation is typically an alkyl-substituted imidazolium or pyridinium ring, while the anion is usually tetrachloroaluminate, hexafluorophosphate, or tetrafluoroborate. In these liquids, the unusually broad liquid temperature range is due in part to the structure of the chosen cation, which exhibits some asymmetry that hinders crystallization, and the large anion,

whose size is prohibitive. Chemical properties including acidity and catalytic selectivity can be fine-tuned through proper selection of cation (variation of alkyl chain lengths) and anion and variation of the mole fraction of each in the liquid (Chauvin and Olivier-Bourbigou 1995). The decision to investigate 1-butyl-3-methylimidazolium



1-butyl-3-methylimidazolium
hexafluorophosphate ([bmim][PF₆])



1-butylpyridinium
tetrachloroaluminate (NBupy-AlCl₄)

Figure 7.2.1 Examples of ionic liquids.

hexafluorophosphate ([bmim][PF₆]) as

our first sample of its kind was based primarily on practical reasons- availability and ease of handling¹.

7.3 Experimental

The sample of 1-butyl-3-methylimidazolium hexafluorophosphate ([bmim][PF₆]) was prepared as described elsewhere (Gordon, Holbrey et al. 1998; Huddleston, Willauer et al. 1998). The sample cell reservoir was fitted with PTFE blocks in order to reduce the necessary volume of sample from > 50 ml to ca. 30 ml. The final step of preparation of [bmim][PF₆] involves extraction with water, and a small amount of water contamination was present at the time of introduction into vacuum. The sample was degassed under

¹ Prof. K. R. Seddon and co-workers have graciously offered to provide IL samples in small quantities for our work; [bmim][PF₆] is among the simplest to synthesize and handle, hence its ready availability.

high vacuum in the TOF spectrometer for 12 hours in order to remove this water. TOF-SARS data was obtained using Ar^+ and Ne^+ ions in the energy range of 1.5 to 2.5 keV and at incidence angles of $\alpha = 8^\circ$ to 36° in increments of 4° . The laboratory scattering and recoil angles were fixed at a value of 45° . Time-of-flight spectra were acquired for a $40 \mu\text{s}$ time window and 1.5 million passes provided sufficient peak intensities.

7.4 Results

7.4.1 Argon

Figure 7.4.1 represents a composite of the spectra acquired with 2.5 keV Ar^+ ions over the entire a range of $\alpha = 8^\circ$ to 36° . A scalar quantity has been added to all but the 36° spectrum in order to clearly separate the scans. The small photon peak P clearly visible in several of the scans has been used to calibrate the TOF time scales to $P = \text{zero}$. The notable features of the spectra include a well-defined H (DR) signal centered at about $7.3 \mu\text{s}$, C (DR) peak at $9.2 \mu\text{s}$, and a small peak that closely follows the C peak near $10.1 \mu\text{s}$. Table 7.1 details the predicted DR flight times for all atoms present in the formula under 2.5 keV Ar^+ bombardment; under these experimental conditions a SS peak due to Ar^+ scattering from P is predicted near $17.1 \mu\text{s}$ but is not visible. A small time difference between predicted and observed TOF values is likely due to a small error (ca. $\pm 0.1 \text{ keV}$) in the measured ion kinetic energy that was discovered after completion of the data acquisition. Nitrogen DR would be between the C and F signals, but is unresolved under these conditions. The broad feature centered near $14.8 \mu\text{s}$ may be

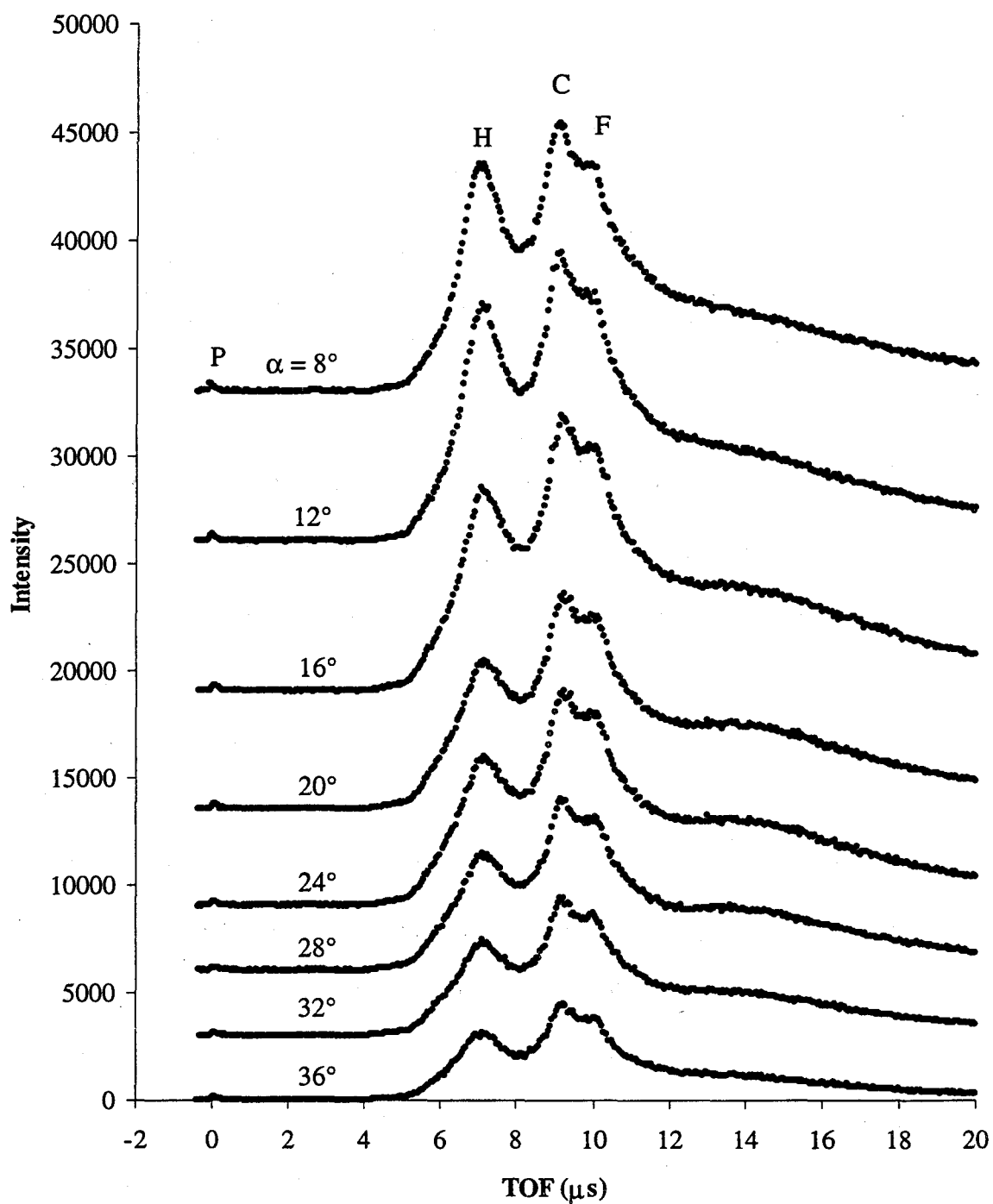


Fig. 7.4.1 Composite of TOF-SARS spectra obtained from [bmim][PF₆] using 2.5 keV Ar⁺ ions. P = photon peak.

Table 7.1 TOFs for selected 2.5 keV Ar⁺ events.

Atom (event)	Predicted TOF, μs	Observed TOF, μs
H (DR)	7.16	7.3
C (DR)	9.08	9.2
N (DR)	9.43	Not resolved
F (DR)	10.31	10.1
P (DR)	12.40	Not observed
P (SS)	17.09	Not observed

attributed to multiply scattered incident ions having a broad velocity distribution. Hydrogen surface recoil events contribute to the shoulder seen on the short TOF-side of the H peak. Although the C and F recoil signals are not completely resolved, the spectrum may be deconvoluted to yield information regarding the atomic ratios accessible. It is advantageous that forward scattering of argon from fluorine is limited to a critical scattering angle of 30.3°, meaning that all the signals observed in spectrum are attributed to recoiled atoms.

In an attempt to better resolve the carbon and fluorine DR signals, the next set of spectra was obtained using 1.5 keV Ar⁺ ions over the same range of α values and is shown in Figure 7.4.2. The spectra appear similar in general- the H (DR) signal appears at 9 μs , and the C (DR) and F (DR) at 11.7 and 12.3 μs respectively. Comparisons between predicted and expected flight times for 1.5 keV Ar⁺ are given in Table 7.2. The fluorine signal is still not fully resolved here; however we can see qualitatively that the carbon signal intensity decreases with increasing α . The signal to noise ratio in the spectra is less than that for the 2.5 keV Ar⁺ data, a consequence of the lower ion beam current at lower energy. A projectile of lower mass, neon, is likely necessary to further resolve the signals.

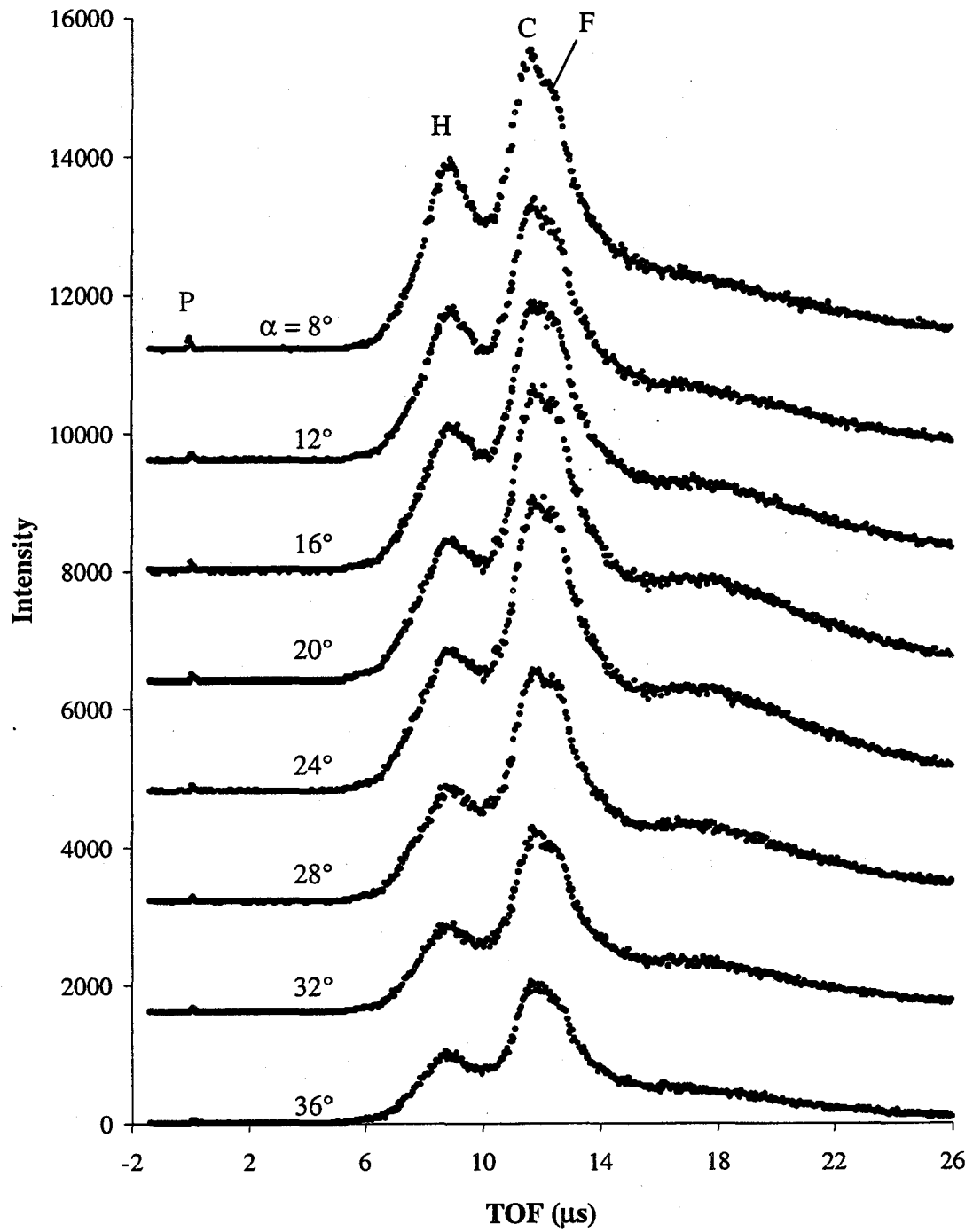


Fig. 7.4.2 Composite of TOF-SARS spectra obtained from [bmim][PF₆] using 1.5 keV Ar⁺ ions. P = photon peak.

Table 7.2 TOFs for selected 1.5 keV Ar⁺ events

Atom (event)	Predicted TOF, μs	Observed TOF, μs
H (DR)	9.24	9.0
C (DR)	11.73	11.7
N (DR)	12.18	Not resolved
F (DR)	13.3	12.8
P (DR)	16.01	Not observed
P (SS)	22.06	Not observed

7.4.2 Neon

Spectra were obtained using Ne⁺ ions over the same range of α values, at energies of 2.5 and 2.0 keV. Although spectra at 1.5 keV were desirable the ion beam current was insufficient at this energy. Figure 7.4.3 illustrates the composite of spectra acquired at all α values for 2.5 keV Ne⁺. It is clear that the signals for H (DR) and C (DR) are resolved better than in the Ar⁺ spectra, and the F (DR) peak is more clearly separated from the C peak. Additionally, we may be observing a signal corresponding to N (DR), expected at 8.4 μs , as this region appears to fill in at higher α as the depth probed increases. It is also expected that Ne⁺ scattering from fluorine (10.26 μs) is present. This Ne scattering signal complicates the interpretation in that the flight times are very close to that of F (DR) and the SS and DR cross sections are very similar (1.1:1) under these conditions. The relative intensities of recoil peaks in the Ne⁺ spectra are quite different than those for Ar⁺, due to dramatically different recoil cross sections when using projectiles of different m_1 . Table 7.3 lists the predicted and observed values for the relevant events. In order to further resolve the signals, the Ne⁺ energy was lowered to

2.0 keV; lower energy would be preferred but it is difficult to obtain sufficient ion current to perform experiments at lower energies. The resulting spectra over the same α range are illustrated in Figure 7.4.4. The time resolution is significantly better, as the F signal maximum is now $> 1.5 \mu\text{s}$ away from the C recoil peak. At $\alpha = 8^\circ$, the F signal is clearly distinguishable from the C signal, but the region between the two fills in considerably as α increases, corresponding to increased incidence of N recoils. Table 7.4 details the predicted vs. observed positions of each TOF event.

Table 7.3 TOFs for selected 2.5 keV Ne^+ events

Atom (event)	Predicted TOF, μs	Observed TOF, μs
H (DR)	5.21	5.1
C (DR)	7.92	8.0
N (DR)	8.41	Not resolved
F (DR)	9.64	9.6
F (SS)	10.26	Not resolved
P (DR)	12.59	Not observed
P (SS)	11.10	Not observed

The procedure for obtaining surface atomic ratios from spectral intensities outlined in Chapter 5 was again used. Comparative sets of spectra were deconvoluted using Peakfit™: 2.5 keV Ar^+ data was analyzed at incident angles of 8° and 36° , and the same angles were chosen from the 2.0 keV Ne^+ data. These particular angles were chosen to compare the results obtained at the extremes of the probe depths. Figure 7.4.5 illustrates the fitted 2.5 keV Ar^+ TOF-SARS spectra at $\alpha = 8$ and 36° and the deconvolution of individual peaks. The corresponding figure for the data obtained using 2.0 keV Ne^+ ions is shown in Figure 7.4.6. A nitrogen recoil peak was added to the neon

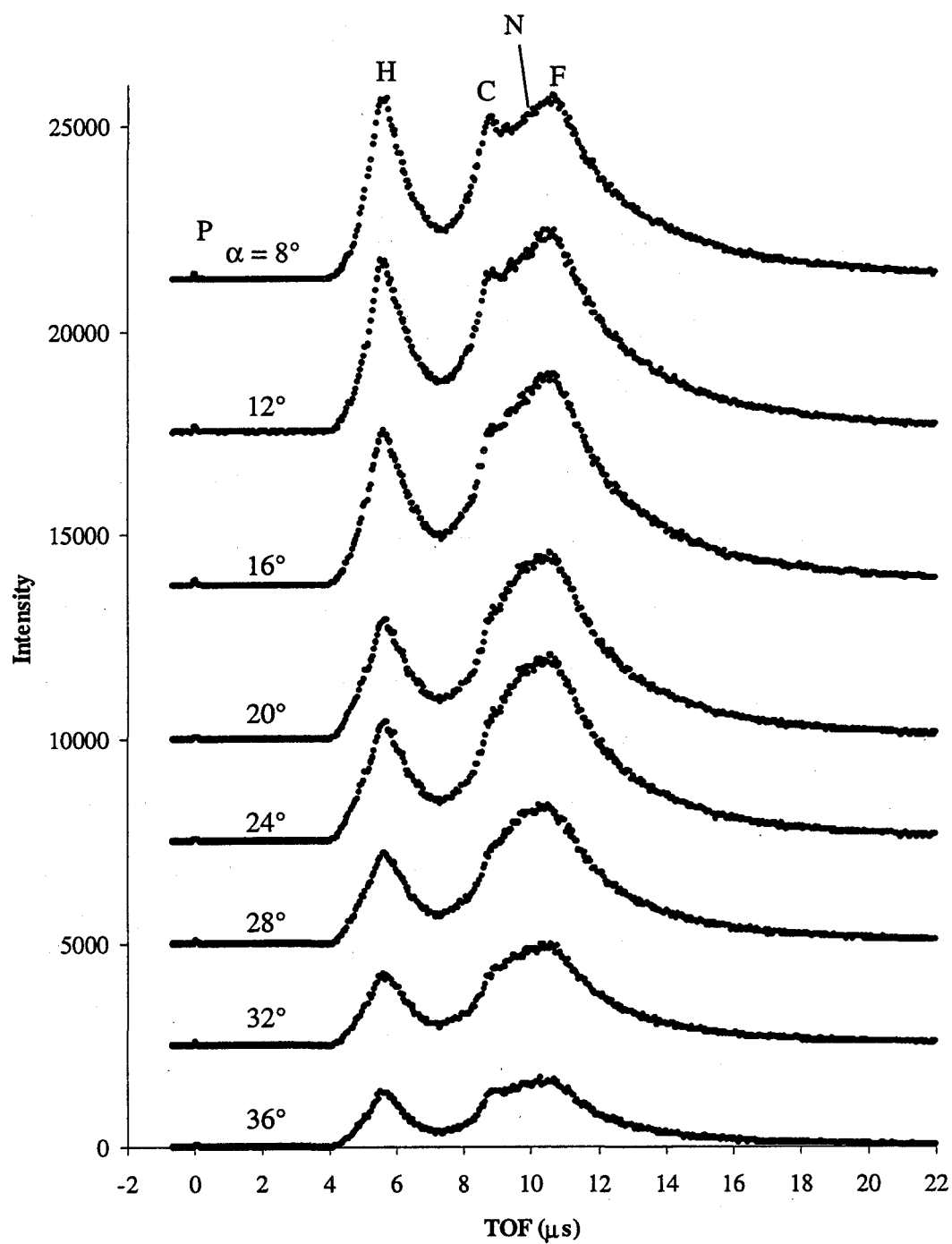


Fig. 7.4.4 Composite of TOF-SARS spectra obtained from [bmim][PF₆] using 2.0 keV Ne⁺ ions. P = photon peak.

Table 7.4 TOFS for 2.0 keV Ne⁺ events.

Atom (event)	Predicted TOF, μs	Observed TOF, μs
H (DR)	5.83	5.8
C (DR)	8.85	9.0
N (DR)	9.40	Not resolved
F (DR)	10.78	10.7
F (SS)	11.47	Not resolved
P (DR)	14.59	Not observed
P (SS)	9.61	Not observed

spectra, as this phenomenon contributes to the curvature in the region near 9.5 μs and this addition improves the accuracy of the fluorine intensity measurement.

Based on the events expected under these two sets of experimental conditions, interpretation of the spectra is somewhat complicated. The argon spectra should be more useful in obtaining information regarding the fluorine atoms, since no single scattering of argon ions is possible, whereas the neon spectral region in the region of 10-12 μs is composed of both events to a nearly equal but undetermined extent. As a result, it should be noted that the figures listed for the neon-based C/F ratios in Table 7.5 are not as reliable as those for the argon data. However, the neon data is appropriate for determining the H/C ratios due to the good separation of the H (DR) and C (DR) signals. Listed in the left side of Table 7.5 are H/C and H/F intensity ratios for atoms at the surface of [bmim][PF₆] based on 2.5 keV Ar⁺ data using the deconvoluted spectra of Figure 7.4.5. The right side of the table contains intensity ratios calculated for the 2.0 keV Ne⁺ data based on the deconvolutions illustrated in Figure 7.4.6. These ratios are converted to the surface atomic ratios listed in Table 7.6.

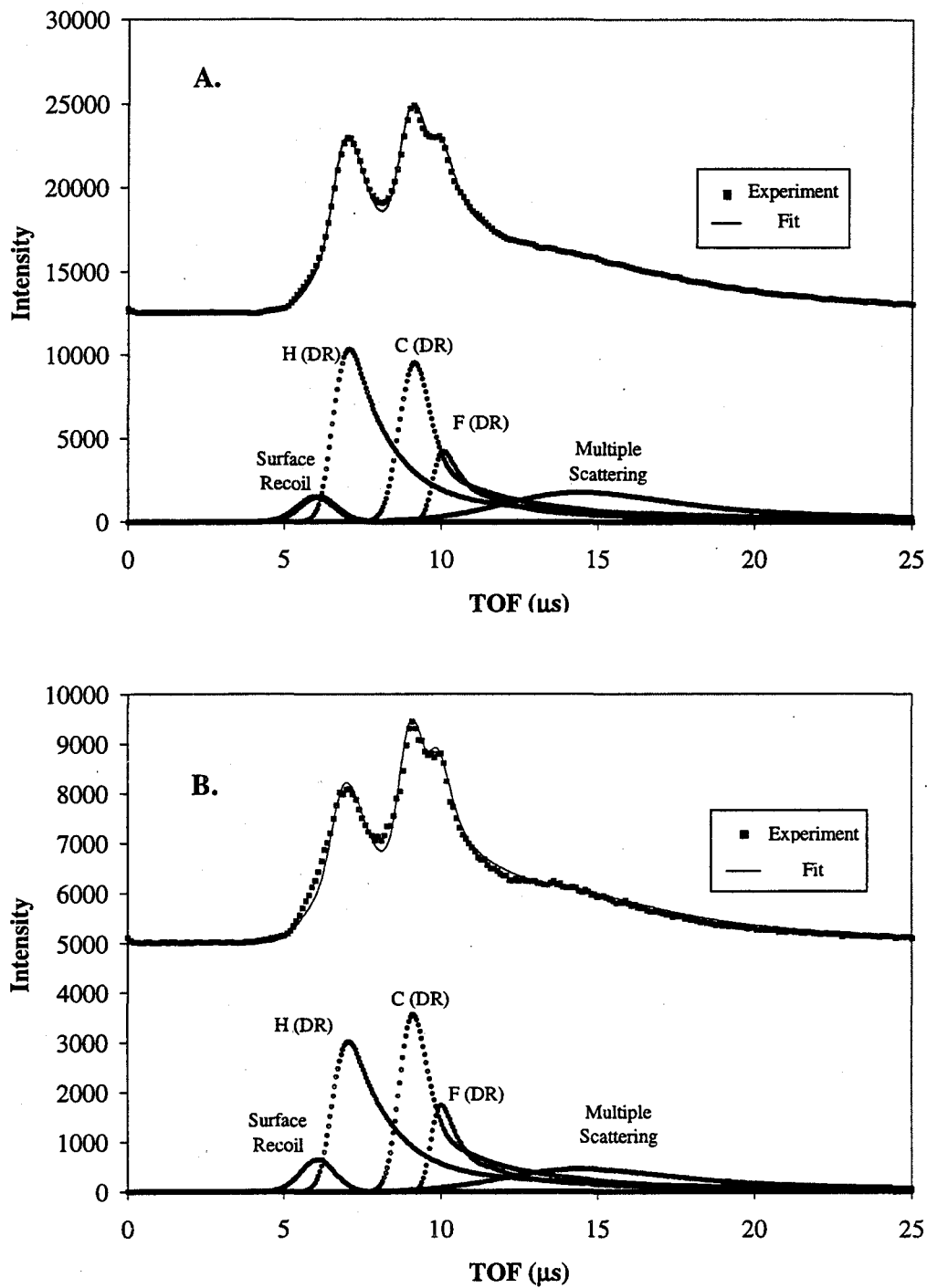


Figure 7.4.5 Fitted 2.5 keV Ar⁺ TOF-SARS spectra of [bmim][PF₆]. A. $\alpha=8^\circ$. B. $\alpha=36^\circ$.

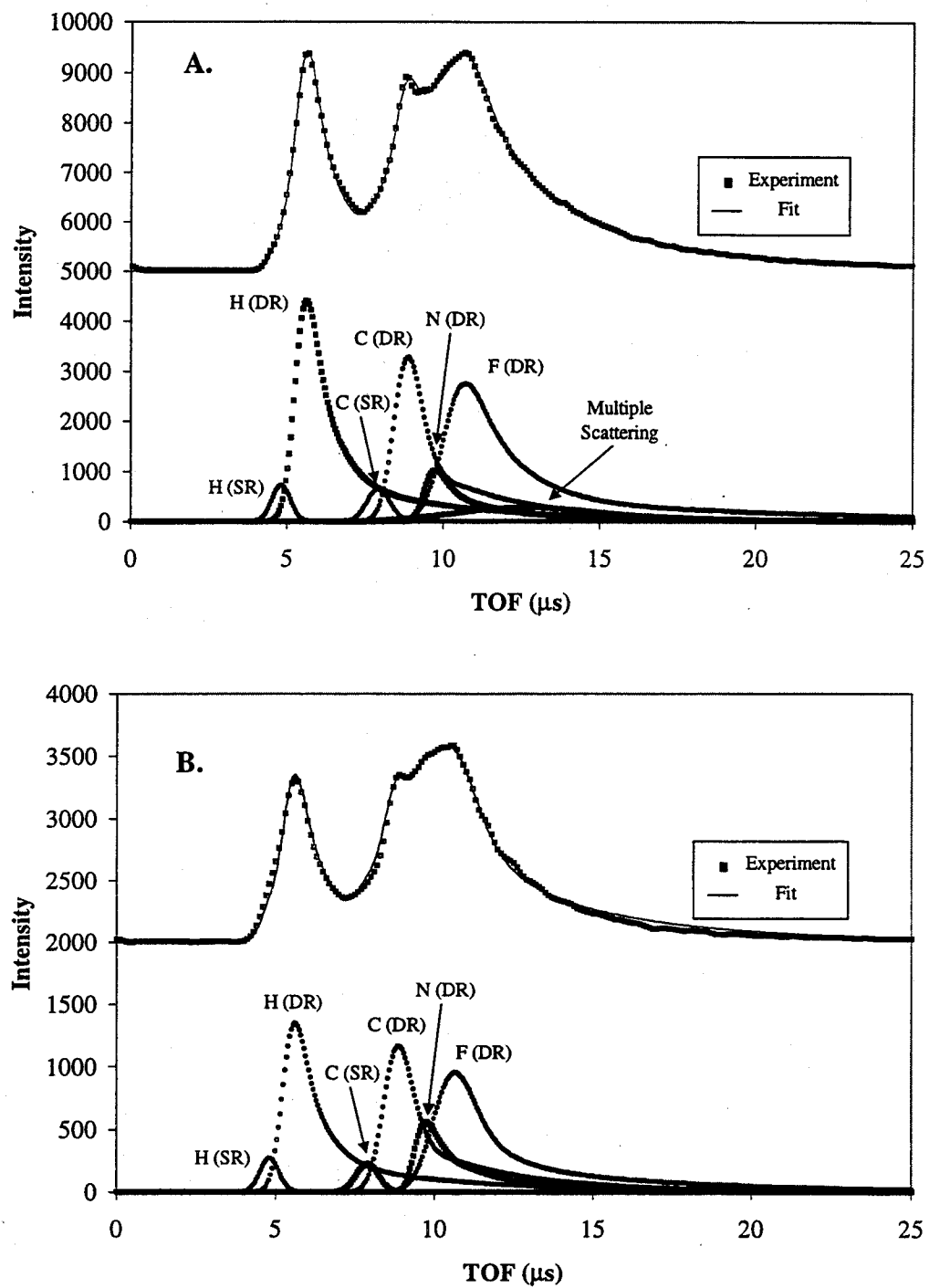


Figure 7.4.6 Fitted 2.0 keV Ne⁺ TOF-SARS spectra of [bmim][PF₆] A. $\alpha=8^\circ$. B. $\alpha=36^\circ$.

Table 7.5 Spectral Intensity Ratios in [bmim][PF₆] from 2.5 keV Ar⁺ and 2.0 keV Ne⁺ data

α°	2.5 keV Ar ⁺		2.0 keV Ne ⁺	
	H/C	C/F	H/C	C/F
8	1.1-1.3	1.9-2.1	1.2-1.4	1.1-1.3
36	0.9-1.1	2.1-2.3	1.1-1.2	1.2-1.3

Table 7.6 Surface Atomic Ratios in [bmim][PF₆] based on 2.5 keV Ar⁺ and 2.0 keV Ne⁺ data

α°	2.5 keV Ar ⁺		2.0 keV Ne ⁺	
	H/C	C/F	H/C	C/F
8	1.5-1.7	1.9-2.1	1.6-1.8	1.1-1.3
36	1.2-1.5	2.1-2.3	1.4-1.6	1.2-1.3

7.5 Discussion

7.5.1 Cation-Anion Surface Composition

In determining the composition of the surface of [bmim][PF₆], the data collected using Ar⁺ ions is of greatest use in determining the C/F ratio for reasons previously mentioned. Values for the C/F ratio based on the neon data are considered inconclusive and have been included in Table 7.6 only for completeness. The left side of Table 7.5 lists the corrected atomic ratios based on the intensity ratios, calculated using Equation 5.5.2. Noting that the surface atomic ratio of C/F is close to 2 at both 8 and 36°, it is immediately obvious that the recoil spectrum contains signals from both the cation (C, H) and anion (F). This rules out extreme variations of the composition where either the cation or anion dominates. If the anion were highly enriched in the surface, the carbon-

containing cation would be essentially excluded from the surface, resulting in a C/F ratio of <1 ; conversely, cation domination would lead to an observed C/F ratio of >1 . Within this argument, it is only sensible to conclude that the surface is neither cation-rich nor anion rich, but that they share the surface composition to a large extent.

Unfortunately [bmim][PF₆] does not crystallize well and X-ray diffraction characterization data is unavailable. A crystallographic study of the similar low-melting salt 1-ethyl-3-methylimidazolium hexafluorophosphate ([emim][PF₆], mp 58-60° C) is the nearest available (Fuller, Carlin et al. 1994). The anion is located above the cation ring with a typical closest cation-anion distance that is near the Van der Waals distance of ~ 2.7 Å, and this is consistent with a simple coulombic-type interaction between the ions. This finding is supported for a series of larger homologous hexafluorophosphates-[C_n-mim][PF₆] where n = 12, 14, 16, and 18 (Gordon, Holbrey et al. 1998). A simple coulombic interaction would lend credence to the assumption that the anion is situated close to the charge center of the aromatic cation ring. In any case there is little reason to expect the surface ratio of cations to anions to deviate significantly from 1:1. This issue will be discussed in more detail.

In addition to the evidence regarding the surface population of anions and cations, the C/F ratio yields some information regarding the orientation of the cation. The two extreme possibilities are either (a) the ring is normal to the surface, vertically oriented or (b) the ring is parallel and lays flat. In the second scenario, the methyl substituent and to a lesser extent the butyl group will necessarily lie in the surface plane. Considering the ideas of local shadowing and blocking of atoms by nearest neighbors, very little shadowing will occur in this case, as essentially all the cation C and N atoms lie in-plane.

If this is true the surface stoichiometry will be very similar to the overall cation stoichiometry, yielding an H/C ratio close to 2. The experimental H/C atomic ratios given in table 7.6 are on average considerably less than 2 (1.4-1.8), which does not support the "cation flat" orientation. Additionally a greater amount of nitrogen would likely be seen, as shadowing and blocking would limit the N recoils. If the cation is instead oriented normal to the surface, a range of H/C values is possible depending on how the cation is rotated relative to surface-parallel axis passing through the ring center. The discussion of the cation orientation in the following section results in an estimate of the surface-accessible C atoms per cation of roughly 5. The data in Table 7.5 indicates that the C/F atomic ratio is approximately 2; this implies that about 2.5 F atoms per anion are accessible at the surface, again assuming an anion to cation ratio of 1:1. This result is consistent with the octahedral geometry of the hexafluorophosphate anion, which on average should expose ~3 of the 6 fluorine ligands at the surface, reduced somewhat by shadowing and blocking effects. Recoiled fluorine atoms originating from the interior side of the anion will be effectively blocked upon exit from the liquid, leaving a maximum of 3 fluorines/anion accessible at the surface. Despite the high symmetry of the anion, not all configurations expose three coplanar F atoms at the surface, and several expose only 1-2 fluorines. The average surface atomic concentration of F atoms should be somewhat less than 3, and the experimentally determined value of about 2.5 is entirely reasonable within this framework.

7.5.2 Cation Surface Orientation

Following the argument that the ring of the [bmim] cation is oriented perpendicularly relative to the surface, further investigation of the rotational orientation about the ring axis is a reasonable extension. Figure 7.5.1 illustrates TOF spectra under matching conditions (2.5 keV

Ar⁺, $\alpha = 8^\circ$) of [bmim][PF₆] and squalane, which exhibits an H/C stoichiometric ratio of slightly greater than 2:1. From this comparison, we can conclude by inspection that the accessible H/C atomic ratio in [bmim][PF₆] is considerably less than 2:1. With that in mind, orientations that place

the butyl side chain outward are immediately ruled out, as the H/C stoichiometry in these configurations is ≥ 2 . The remaining possible orientations involve the carbons of the aromatic ring and/or some combination of the carbons in the alkyl chain substituents.

Consideration of the C/H surface atomic ratio will primarily focus on the 2.0 keV Ne⁺ data, as the H and C recoil signals are better resolved. During the spectral deconvolution (Figure 7.4.6), this improved resolution allows for a better estimate of the H-recoil tail and hence a more accurate determination of the C recoil intensity. Turning to the 2.0 keV Ne⁺ data of Table 7.6 and Figure 7.5.1, the quantitative evaluation of the

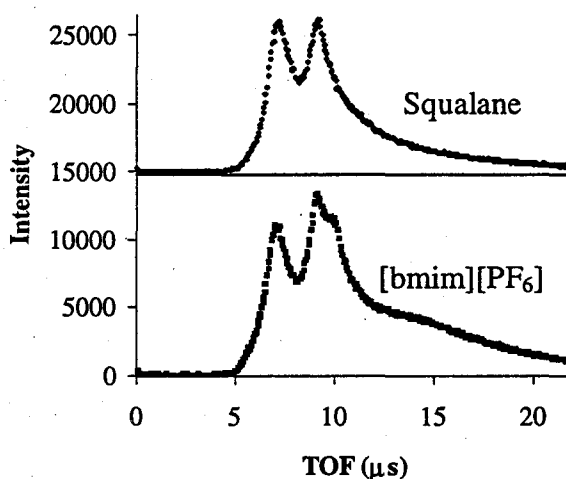


Figure 7.5.1 TOF-SARS spectra of squalane and [bmim][PF₆]. 2.5 keV Ar⁺ ions incident at $\alpha = 8^\circ$.

H/C ratios support the visual impression that the H/C surface atomic ratio is significantly higher at the shallow incidence angle of 8° . This effect can be understood in terms of the varying degrees of surface penetration that occur as α changes- a glancing angle prohibits the penetration, whereas

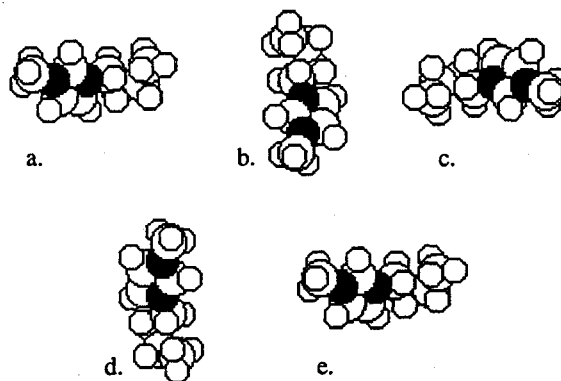


Figure 7.5.2 Rotations of the [bmim] cation relative to the surface-parallel ring axis.

steeper angles allow probing of greater depths. In the [bmim] cation, the outermost layer consists of a significant number of hydrogens; the carbons and nitrogens are less accessible relative to the H atoms at glancing angles- as a result, the information regarding other surface atoms is somewhat limited. Data obtained at higher angles do penetrate the surface to a larger extent, but the phenomenology is the same- recoils that appear at the expected TOFs in the spectrum still originate in the outermost atomic layer of the liquid regardless of corrugation.

In order to infer the [bmim] cation orientation, experimentally obtained H/C ratios will be compared with ratios derived from models of the cation in various orientations. The Line-of-Sight (LOS) program used for the analysis of glycerol in Chapter 6 was employed. A suitable molecular model of the [bmim] cation was constructed, with the butyl group in a partially extended conformation and situated approximately orthogonal to the ring as in all depictions of Figure 7.5.2. The conformation was chosen to reasonably represent the average side chain orientation,

avoiding extreme configurations that place the chain very close to the ring or with the chain completely folded or extended. This is similar to reported conformations of longer-chain [C_n -mim] hexafluorophosphate homologues (Gordon, Holbrey et al. 1998). Once the cation structure was optimized, the ring was oriented in a plane perpendicular to the surface, with the nitrogen atoms (darkest) oriented symmetrically uppermost in the surface as shown in (a) of Figure 7.5.2 and the rotation angle of this orientation was arbitrarily designated as 0° . The ring was then rotated counter-clockwise in 30° increments; several representative rotations are shown in b. through e. (90° to 360°) of Figure 7.5.2. LOS simulations of the accessible surface atoms in each of the rotated orientations shown were performed, and the results are graphically represented below.

Recoil spectrometry performed on crystalline surfaces gives results that can vary dramatically as the azimuthal direction of incidence (rotation about an axis normal to the surface) changes, due to anisotropic shadowing and blocking effects. For liquid surfaces, it is expected that this effect will be largely negated due to continuous molecular motions with respect to nearest neighbors on the surface. As a result, the azimuthal angle of approach of incident ions on surface species is not well defined for liquids, and we assume that the direction is randomized. This azimuthal randomization plays a key role in modeling the estimated surface atomic ratios for [bmim], as the accessible H/C atomic ratio changes markedly, for example, between a direction parallel to the molecular axis of the cation and one perpendicular to it. The effect is dramatically portrayed in Figure 7.5.3 and the corresponding Table 7.7, in which the estimated hydrogen and carbon atoms per orientation for the four 90° azimuths represented are listed. The LOS program

probes azimuthal angles over the entire 360° range in user-defined increments (5° in this case).

Table 7.7 Estimated C and H atoms per [bmim] cation for the azimuthal rotations in Fig. 7.5.3 ($\alpha = 36^\circ$)

	A	B	C	D	Average
H	8.9	9.6	8.1	8.2	8.5
C	7.0	5.4	3.2	4.7	5.3

The averages for the atoms per cation as listed are area-weighted to account for differences in cross-sectional area. Ions approaching from the side direction along an incidence angle of 36° encounter the topmost

CH groups but also have a clear path to several

H and C atoms on the side chains. The lower C

atom in the ring may be shadowed by the anion if the cation ring and anion are closely associated. The resulting ratio of H to C using

this method is calculated to be 1.3 for the (a)

azimuth. Ions approaching from the opposite side as in the (b) azimuth can interact with

many of the hydrogens but experience some

shadowing of the interior carbon atoms, which results in a H/C ratio of ~ 1.8 . In the (c)

and (d) azimuths illustrated, ions are approaching at $\alpha = 36^\circ$ along the molecular axis. In

each of these cases a large number of hydrogens are accessible, but the shadowing effect

of the carbon atoms along the axis is enhanced, which gives higher H/C ratios 2.5 and 1.7

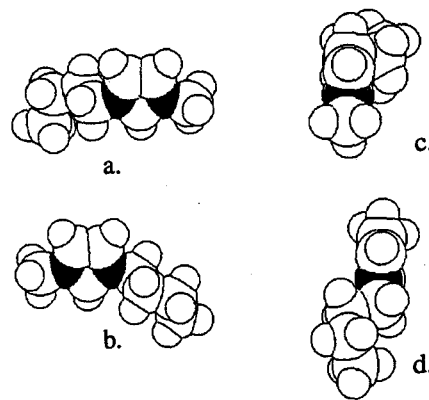


Figure 7.5.3 90° azimuthal rotations of [bmim] viewed at $\alpha = 36^\circ$.

for (c) and (d) respectively. The illuminated areas of (a) and (b) are considerably greater than those of (c) and (d), and the area-weighted H/C ratio is roughly 1.6. The large differences in H/C ratios for the different azimuths reiterate that azimuthal averaging is a crucial step in estimating reasonable accessible atomic ratios, and the LOS program accounts for this. Overall, the actual accessible carbon atomic concentration per cation in this "ring-vertical" orientation varies with the azimuthal direction between the extremes of 7.0 (a) and 3.2 (c). The weighted average is 5.3 atoms per cation and is the source of the value presented in Section 7.5.1.

The results of calculations of the accessible H/C ratio as a function of the rotation angle about the ring axis are plotted in Figure 7.5.4 for both the 8° and 36° incident angles. Horizontal brackets indicate the ratios obtained experimentally using both argon and neon projectiles for direct comparison. Vertical lines through the intersections of the LOS-calculated curves with the experimental ratio values illustrate the range of rotations that most closely correlate with the experimentally determined ratios. The calculated ratio at the reference angle (0° and 360°) is between 1.8 and 2.1; as the butyl group rotates upward the H/C ratio increases, and then decreases markedly to values from 1.5 to 1.8 at ring rotations in the neighborhood of 180°. As could be expected, the ratio again increases as the methyl group becomes more visible, and the calculated H/C values increase to 2.5 to 2.8 at a rotation of 270° before returning to the original value after a full revolution. Experimentally obtained values of the H/C ratio (Table 7.6) overlap, within approximately $\pm 15^\circ$ of rotation, the region of Figure 7.5.4 corresponding to the cation orientation that involves the CH groups of the ring pointed outward. This analysis suggests strongly that there is a rotationally preferred "ring vertical" [bmim] cation

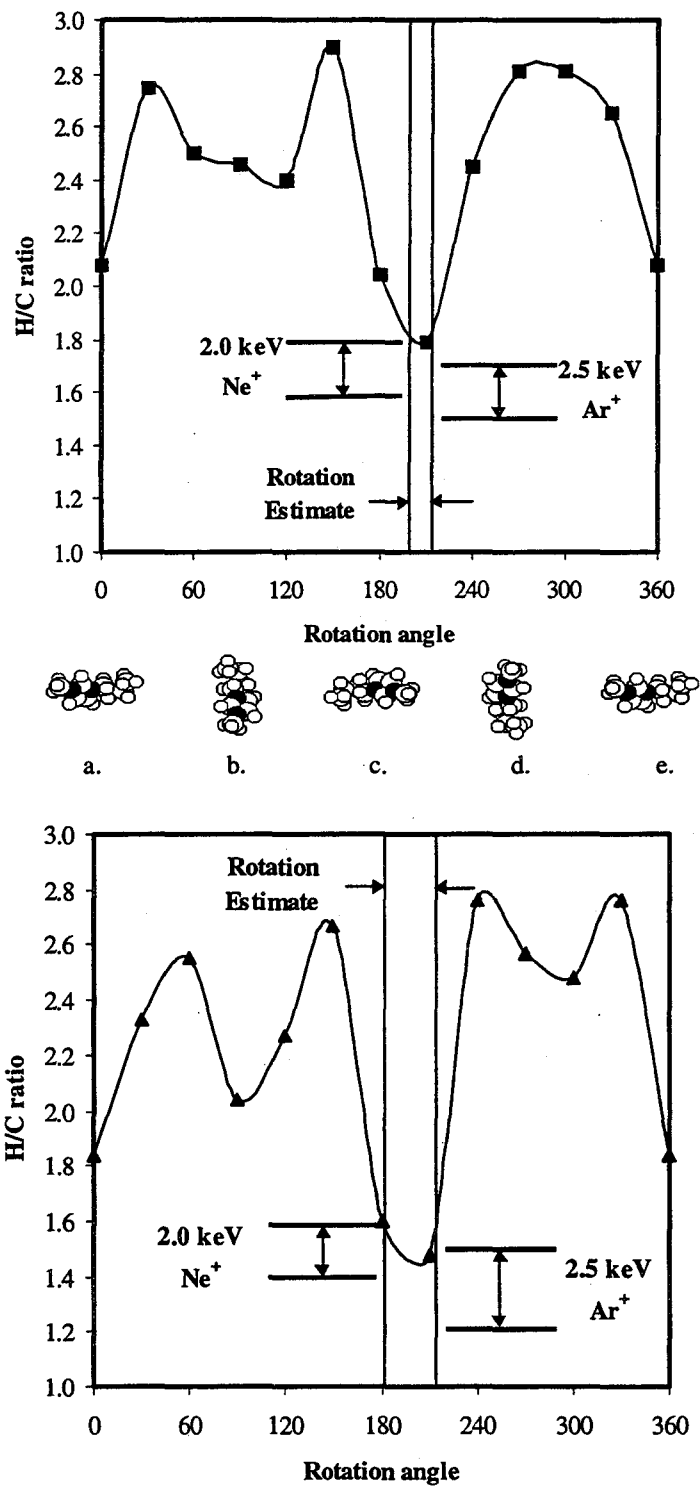


Figure 7.5.4 LOS simulation plots for the [bmim] cation rotated about the ring axis. Vertical lines show the regions of rotation yielding H/C ratios within experimental limits. A. $\alpha = 8^\circ$. B. $\alpha = 36^\circ$.

orientation, that favors the aromatic ring CH groups of the cation ring pointing outward. The analysis is valid even if the actual H/C ratios are slightly higher than those experimentally determined, a possibility based on the current understanding of the ratio of cross-sections.

7.6 Conclusion

This study represents the first measurement of the composition and molecular orientation at the surface of a room-temperature ionic liquid (1-butyl-3-methylimidazolium hexafluorophosphate) using TOF-SARS spectrometry on continuously refreshed surfaces. The findings include a) that bulk stoichiometry is conserved at the surface, i.e. neither cation nor anion is significantly enriched at the surface; b) that the average orientation of the cation is with the plane of the ring vertical relative to the surface plane; and c) that the cation ring is on average rotated about an axis through its center such that the CH groups are oriented outward, and the nitrogens are deeper in the surface, within approximately $\pm 20^\circ$ of the surface normal.

8. Concluding Remarks

8.1 General

It has been shown in this work that the TOF-SARS technique, when applied to molecular liquid surfaces, is capable of resolving different atoms in the outermost surface layer of the liquid. Careful choice of projectile ion, incident kinetic energy, and recoil angle facilitate separation of the signals of different recoiled atoms and also recoiled atoms from scattered primary particles. From experimental intensity ratios, surface atomic composition can be inferred; this information suggests the molecular orientation at the surface. A better understanding of the basis for quantitative determination through the intensity ratio conversion is desirable, as some issues regarding the recoil cross sections in this energy range are as yet unresolved. However, important first steps have been taken toward exploiting the TOF-SARS method for investigating molecular liquid surfaces. The potential for the power of this technique in determining surface molecular orientations is not yet fully developed, and will continue to grow. Summaries of the important experimental findings are presented here, as well as the direction of each project should future studies be pursued.

8.2 'Head' vs. 'Tail' Orientation

8.2.1 Summary

In Chapter 6 a TOF-SARS investigation of two similar systems (DOP and BEHC) having similar 'head and tails' molecular structure revealed that the two molecules assume a similar surface orientation. The main difference between the two structures involves an aromatic ring head in the case of DOP and an extensively chlorine-substituted seven-membered bridgehead ring for BEHC. Comparison of the spectra revealed a similar H/C ratio for both, indicating that the molecular 'heads' could not be extensively accessible based on the stark contrast in head stoichiometries. In the BEHC spectrum, the appearance of recoil and scattering signals due to the presence of chlorine atoms indicates that the head of the molecule is at least partially accessible to incident ions. The most likely orientation for both DOP and BEHC is one that involves one or both tails predominantly on the surface, and part of the ring 'head' exposed.

8.2.2 Future Studies

A possible follow-up to this phase of the work involves comparison of the present knowledge with a newly available homologue of BEHC known as diallyl chlorendate ($C_{15}H_{12}O_4Cl_6$, Bimax). This interesting substance is used as a specialty monomer for various applications including flame-retardant materials, antistatic films, and optically curable polymers (Bimax 1999). A sample of the material has been

recently obtained and time limitations on use of the spectrometer prevented inclusion here. This molecule has the chlorine-substituted head of BEHC with allyl ester tails rather than the 2-ethylhexyl substituents. Vapor pressure data is unavailable but its large molecular weight (469) and apparent high viscosity make it at least a possibility for study by this technique. Interesting comparisons would include the accessible H/C ratio, which should be lower than that of BEHC based on stoichiometry alone, even if the tails dominate the surface composition.

8.3 Glycerol Surface

8.3.1 Summary

A new approach to the analysis of TOF-SARS data was used for the first time in investigating the glycerol surface. TOF-SARS was used to probe the surface under different conditions of projectile and incident energy and the resulting signals arising from surface C, H, and O atoms were converted to surface atomic ratios. The Line of-Sight program was used to simulate accessible atomic ratios for a variety of molecular orientations, and the outcomes were compared with the experimentally determined atomic ratios. Two conformers of glycerol were investigated, $\alpha\alpha$ - and $\beta\gamma$ -glycerol, differing by rotations about the C-C bonds. The results of comparison between the LOS simulations and experiment are somewhat inconclusive, but allow many possible orientations to be ruled out. Comparison of the C/O atomic ratios provides the best indication of whether a particular orientation is reasonable. Three LOS-simulated orientations of the molecule were within an average deviation of ± 0.14 from the

experimental C/O ratios over all α ; the next nearest apparent match was within ± 0.17 . Possible orientations based on this analysis would include a horizontal orientation of the $\alpha\alpha$ -conformer and two vertical $\beta\gamma$ -conformers that only differ by rotation of the middle hydroxyl hydrogen. Beyond this a single surface orientation cannot be definitively stated at this time; however, this is probably the most convincing experimental evidence available.

8.3.2 Future Studies

At least two additional approaches would be beneficial in more exactly determining the surface orientation of glycerol molecules. The first of these would be a deuterium-labeled version of glycerol (possibilities are $\text{HOCD}_2\text{CHOHCD}_2\text{OH}$ and $\text{DOCH}_2\text{CHODCH}_2\text{OD}$). LOS simulations would better differentiate between the methylene hydrogens of the terminal carbons and the hydroxyl hydrogens. TOF-SARS experiments could potentially distinguish H recoils from D recoils (predicted $\Delta\text{TOF}_{\text{D-H}} = 0.71 \mu\text{s}$ for 1.5 keV He^+ ions), but not easily. Under any conditions, the D recoil signal falls close the signal due to helium scattering from carbon ($\Delta\text{TOF} \approx 0.15$), and the small recoil signal could wash out within the relatively larger scattering peak. Admittedly this experiment would be difficult under the present capabilities of the spectrometer; a very large current of He^+ or a very long acquisition time would be necessary to produce measurable recoil signals. Alternatively a difference between the spectra of deuterated and normal glycerol could be taken much like the comparison made between DOP and BEHC. Deuterated samples are quite expensive but

economically these experiments would be more feasible now than originally, as a cell with a ca. 5 mL volume is in development.

The second mode of study involves a more rigorous simulation of the conformer of glycerol molecules at the surface. A very careful experimental quantitative analysis compared with a broader variety of LOS-simulated conformers in different orientations may hold more clues to the true identity of the surface conformation and orientation. It is my opinion that some assumption or additional information beyond a TOF-SARS will be necessary in any case, as the small highly symmetrical glycerol molecule can have quite similar accessible atomic ratios in more than one surface orientation as has been observed here.

8.4 Ionic Liquid Surfaces

8.4.1 Summary

A room-temperature hexafluorophosphate salt, 1-butyl-3-methylimidazolium hexafluorophosphate was investigated by TOF-SARS in what was likely the most fascinating phase of the project to this point. In this ionic liquid, signals arising from H and C ([bmim] cation) and F (PF_6^-) were observed and analyzed. From the ratio of C to F atoms observed it was deduced that the cation and the anion share the surface nearly equally. If coulombic attraction between cation and anion accurately describes the interaction, the anion and the charged ring should exhibit local ordering with the anion ~ centered above the ring, as has been observed through crystallography of analogous ionic liquids (Fuller, Carlin et al. 1994). Based on this assessment the

cation, consisting of an alkyl-substituted aromatic ring, is limited to an orientation that places the ring vertical relative to the surface in some rotated orientation. Comparison of experimental H/C ratios with LOS simulations provides a reasonable estimate of the rotation of the cation ring, within about $\pm 20^\circ$. The preferred orientation has the adjacent aromatic carbons of the imidazolium ring facing outward at the interface. The H/C ratio may be slightly underestimated, but this does not significantly alter the result.

8.4.2 Future Studies

Ionic liquids are a very precious commodity in the development of TOF-SARS as a surface investigation technique. As a class of materials they are of extreme interest to this work not only for their desirable bulk properties, but also for their inclusion of interesting heavy atoms (F, P, Cl, etc.). These substances have an almost unlimited potential to help characterize the capabilities of TOF-SARS while the technique reveals more about their microscopic surface properties.

Work is underway in this lab to begin a new study involving a series of [bmim][PF₆] homologues. Several samples are in hand, including [bmim][BF₄] and the corresponding pair of 1-octyl-3-methylimidazolium phosphates. The hope is that trends in cation orientation and surface population the ion pairs can be developed within like groups of ionic liquids, for example the chloride, bromide, and iodide of [bmim]. Alternatively one could probe the effect of altering of the cation by successively extending the length of the 1-substituent chain (C₆, C₈, and C₁₂ are common cations). Ionic liquids have introduced the means of investigating the existence of trends in surface orientation in a nearly limitless variety of ways.

BIBLIOGRAPHY

- Aduro, S. and J. W. Rabalais (1987). Langmuir **3**: 543.
- Baldelli, S., C. Schnitzer, et al. (1998). "The structure of water on HCl solutions studied with sum frequency generation." Chem. Phys. Letts. **302**(1): 157.
- Baldelli, S., C. Schnitzer, et al. (1997). "Sum Frequency Generation Investigation of Glycerol/Water Surfaces." J. Phys. Chem. B **101**: 4607-4612.
- Ballard, R. E., J. Jones, et al. (1984). "Determination of the Liquid Surface Composition of a Binary Mixture by Photoelectron Spectroscopy-Adiponitrile and Tris(dioxa-3,6-heptyl)amine." Chem. Phys. Lett. **112**: 452.
- Bastiansen, O. (1949). Acta Chem. Scand. **3**: 415.
- Beaglehole, D. (1983). "Ellipsometry of Liquid Surfaces." J. de Physique **44**: C10.
- Beaglehole, D. (1986). Ch. 11. Fluid Interfacial Phenomena. C. A. Croxton. Chichester, John Wiley & Sons.
- Benjamin, I., M. Wilson, et al. (1994). "Scattering of Ne from the liquid-vapor interface of glycerol: A molecular dynamics study." J. Chem. Phys. **100**: 6500.
- Benjamin, I., M. Wilson, et al. (1995). "Scattering of Water from the Glycerol-Vacuum Interface." Chem. Phys. Letts. **243**: 222.
- Bimax (1999) World Wide Web page. <http://www.bimax.com/bimax/dac.htm>.
- Boers, A. L. (1984). Nucl. Instrum. Meth. Phys. Res. B **2**: 353.
- Buck, T. M., H. Wheatley, et al. (1978). "Comparison of a time-of-flight system with an electrostatic analyzer in low-energy ion scattering." Nucl. Instrum. Meth. **149**: 591-594.

BIBLIOGRAPHY (Continued)

Burrous, C. N., A. J. Lieber, et al. (1967). "Detection efficiency of a continuous channel electron multiplier for positive ions." Rev. Sci. Instrum. **38**(10): 1477-1481.

Chauvin, Y. and H. Olivier-Bourbigou (1995). Chemtech **25**(9): 26.

Chelli, R., P. Procacci, et al. (1999). "Glycerol Condensed Phases Part I. A molecular dynamics study." Phys. Chem. Chem. Phys. **1**: 871-877.

Chelli, R., P. Procacci, et al. (1999). "Glycerol condensed phases Part II. A molecular dynamics study of the conformational structure and hydrogen bonding." Phys. Chem. Chem. Phys. **1**: 879-885.

Chen, J. N., M. Shi, et al. (1986). "Detection of Low Energy Neutrals by a Channel Electron Multiplier." Nucl. Instrum. Methods **B16**: 91.

Chen, Z., D. H. Gracias, et al. (1999). "Sum frequency generation (SFG) - surface vibrational spectroscopy studies of buried interfaces: catalytic reaction intermediates on transition metal crystal surfaces at high reactant pressures; polymer structures at the solid-gas and solid-liquid interfaces." Appl. Phys. B **68**: 549.

Chu, W.-K., J. W. Mayer, et al. (1978). Backscattering Spectrometry. New York, Academic Press.

Contarini, S., J. A. Schultz, et al. (1987). Appl. Surf. Sci. **28**: 291.

Croxton, C. A., Ed. (1986). Fluid Interfacial Phenomena. Chichester, John Wiley & Sons.

Dietz, L. A. and J. C. Sheffield (1975). "Secondary electron emission induced by 5-30 keV monatomic ions striking thin oxide films." J. Appl. Phys. **46**(10): 4361-4370.

Eckstein, W. (1981). Inelastic Particle-Surface Collisions, Berlin, Springer-Verlag.

BIBLIOGRAPHY (Continued)

Eisenthal, K. B. (1996). "Liquid Interfaces Probed by Second-Harmonic- and Sum-Frequency- Spectroscopy." Chem. Rev. **96**: 1343.

Freemantle, M. (1998). "Designer Solvents". C&E News. **76**: 32-37.

Fuller, J., R. T. Carlin, et al. (1994). "Structure of 1-ethyl-3-methylimidazolium hexafluorophosphate: Model for room temperature molten salts." J. Chem. Soc., Chem. Commun.: 299-300.

Gemmel, D. S. (1974). Rev. Mod. Phys. **46**: 129.

Giles, C. H. (1969). "Franklin's teaspoonful of oil (Studies in the early history of surface chemistry, pt. 1)." Chemistry and Industry **45**: 1616-1624.

Glycerine Producers Association Research Laboratories (1939). Glycerine and its Derivatives. Chicago, Glycerine Producers Association Research Laboratories.

Goh, M. C., J. M. Hicks, et al. (1988). "Absolute Orientation of Water Molecules at the Neat Water Surface." J. Phys. Chem. **92**: 5074.

Gordon, C. M., J. D. Holbrey, et al. (1998). "Ionic liquid crystals: hexafluorophosphate salts." J. Mater. Chem. **8**(12): 2627.

Govoni, S. T. and G. M. Nathanson (1994). "Exploring the fate of water molecules striking concentrated sulfuric acid: scattering versus solvation." J. Am. Chem. Soc. **116**(2): 779.

Gragson, D. E., B. M. McCarty, et al. (1996). "Surfactant/Water Interactions at the Air/Water Interface Probed by Vibrational Sum Frequency Generation." J. Phys. Chem. **100**(34): 14272.

BIBLIOGRAPHY (Continued)

Gragson, D. E. and G. L. Richmond (1997). "Comparisons of the Structure of Water at Neat Oil/Water and Air/Water Interfaces as Determined by Vibrational Sum Frequency Generation." Langmuir **13**(18): 4804.

Hall, D. G., B. A. Pethica, et al. (1970). Bull. Chem. Soc. Japan **48**: 1991.

Hicks, J. M., K. Kemnitz, et al. (1986). "Studies of Liquid Surfaces by Second Harmonic Generation." J. Phys. Chem. **90**: 560.

Holmberg, S., R. Moberg, et al. (1986). "Angle Resolved Electron Spectroscopy for Measurement of Surface Segregation Phenomena in Liquids and Solutions." J. Electron Spectrosc. Rel. Phenomena **41**: 337.

Huddleston, J. G., H. D. Willauer, et al. (1998). "Room temperature ionic liquids as novel media for 'clean' liquid-liquid extraction." Chem. Commun.(16): 1765.

Hussey, C. L. (1988). "Room temperature haloaluminate ionic liquids. Novel solvents for transition metal solution chemistry." Pure & Appl. Chem. **60**(12): 1763-1772.

Jaeger, R. J. and R. J. Rubin (1997). "Migration of a Phthalate Ester from Polyvinyl Chloride Blood Bags into Stored Human Blood and its Localization in Human Tissues." Nutrition **13**(11-12): 1010.

Keller, W., H. Morgner, et al. (1986). "He(2^3S) and hydrogen bonding molecules: A comparative study of He(2^3S) Penning ionization versus HeI photoionization of formamide and N-methylformamide." Mol. Phys. **57**: 637-644.

Keller, W., H. Morgner, et al. (1986). "Probing the Outermost Layer of a Free Liquid Surface. Electron Spectroscopy of Formamide under He(2^3S) Impact." Mol. Phys. **57**: 623.

BIBLIOGRAPHY (Continued)

Langevin, D., Ed. (1992). Light Scattering by Liquid Surfaces and Complementary Techniques. Surfactant Science Series. New York, Marcel Dekker.

Lehmann, C. (1977). Interaction of Radiation with Solids and Elementary Defect Production. Amsterdam, North-Holland.

Macritchie, F. (1990). Chemistry at Interfaces. San Diego, Academic Press.

Marion, J. B. and S. T. Thornton (1995). Classical Dynamics of Particles and Systems. Fort Worth, Saunders College Publishing.

Mashkova, E. S. a. M., V.A. (1985). Medium Energy Ion Reflection from Solids. Amsterdam, North-Holland.

Mintz, M. H., J. A. Schultz, et al. (1984). Surf. Sci. **146**: 438.

Morgner, H. and J. Oberbordhage (1995). "Tetrabutylammonium iodide in formamide and hydroxypropionitrile : the temperature dependence of segregation studied by metastable induced electron spectroscopy." J. Phys. Condens. Matter **7**: 7427-7441.

Morgner, H., J. Oberbrodage, et al. (1991). "Surface segregation of a binary liquid mixture as studied by metastable impact electron spectroscopy." Mol. Phys. **73**: 1295.

O'Connor, D. J., R. J. MacDonald, et al. (1986). Nuc. Instrum. Meth. B **13**: 235.

O'Hanlon, J. F. (1980). A User's Guide to Vacuum Technology. New York, John Wiley & Sons.

Penfold, J. and R. K. Thomas (1990). "The Application of the Specular Reflection of Neutrons to the Study of Surfaces and Interfaces." J. Phys. Condensed Matter **2**: 1369.

BIBLIOGRAPHY (Continued)

Poelsema, B. and A. L. Boers (1977). "Quasi single collisions in noble gas ion scattering from single crystals: a new calculational approach." Phys. Letts. **64A**: 304-306.

Porter, J. J., J. K. Klassen, et al. (1997). "Energy and angle-resolved uptake of organic molecules in concentrated sulfuric acid." J. Am. Chem. Soc. **12**(22): 251.

Rabalais, J. W. (1988). "Direct Recoil Spectrometry." CRC Critical Rev. Sol. State Sci. Eng. **14**: 319.

Rabalais, J. W. (1990). "Scattering and Recoiling Spectrometry: An Ion's Eye View of Surface Structure." Science **250**: 521.

Rabalais, J. W. (1991). "Time-of-Flight Scattering and Recoiling Spectrometry." J. Vac. Sci. Technol. **A9**: 1293.

Rabalais, J. W., Ed. (1995). Low Energy Ion-Surface Interactions. New York, John Wiley and Sons.

Rabalais, J. W., J. A. Schultz, et al. (1983). J. Chem. Phys. **78**: 5350.

Rice, S. A., J. Gryko, et al. (1986). . Fluid Interfacial Phenomena. C. A. Croxton. Chichester, John Wiley & Sons.

Robinson, M. T. and O. S. Oen (1963). "Comptuer studies of the slowing down of energetic atoms in crystals." Phys. Rev. **132**: 2385-2398.

Ronk, W. R., D. V. Kowalski, et al. (1996). "Inert gas scattering from molten metals: Probing the stiffness and roughness of the surfaces of atomic liquids." J. Chem. Phys. **104**(12): 4842.

Saecker, M. E., S. T. Govoni, et al. (1991). "Molecular Beam Scattering from Liquid Surfaces." Science **252**: 1421.

BIBLIOGRAPHY (Continued)

Saecker, M. E. and G. M. Nathanson (1993). "Collisions of Protic and Aprotic Gases with Hydrogen Bonding and Hydrocarbon Liquids." J. Chem. Phys. **99**: 7056.

Schlossman, M. L. (1992). . Light Scattering by Liquid Surfaces and Complementary Techniques. D. Langevin. New York, Marcel Dekker.

Schultz, J. A., Y. S. Jo, et al. (1985). Nuc. Instrum. Meth. B **10/11**: 713.

Schultz, J. A., M. H. Mintz, et al. (1984). Surf. Sci. **146**: 438.

Schwartz, D. K., M. L. Schlossman, et al. (1990). "Thermal Diffuse X-Ray-Scattering Studies of the Water-Vapor Interface." Phys. Rev. **A41**: 5687.

Seddon, K. R. (1997). "Ionic Liquids for Clean Technology." J. Chem. Tech. Biotechnol. **68**: 351-356.

Seddon, K. R. (1997). Room-Temperature Ionic Liquids: Neoteric Solvents for Clean Catalysis, The Queen's University of Belfast School of Chemistry WWW Server. <http://www.ch.qub.ac.uk/resources/ionic/review/review.html>.

Shen, Y. R. (1989). Nature **337**: 519.

Shultz, M. J. (1999). Personal Communication. September 7, 1999.

Siegbahn, H. (1985). "Electron Spectroscopy for Chemical Analysis for Liquids and Solutions." J. Phys. Chem. **89**: 897.

Simonelli, D., S. Baldelli, et al. (1999). "Ammonia-water complexes on the surface of aqueous solutions observed with sum-frequency generation." Chem. Phys. Letts. **298**(4): 400.

BIBLIOGRAPHY (Continued)

Smith, D. P. (1967). "Scattering of low-energy noble gas ions from metal surfaces." J. Appl. Phys. **38**: 340-347.

Stensgaard, I., L. C. Feldman, et al. (1978). "Calculations of the backscattering-channeling surface peak." Surf. Sci. **77**: 513-522.

Superfine, R., J. Y. Huang, et al. (1990). "Phase Measurements for Surface Infrared-Visible Sum-Frequency Generation." Opt. Lett. **15**: 1276.

Turkenburg, W. C., R. G. Smeenk, et al. (1978). "Investigations of surface relaxation and surface composition of Ni (100) by medium energy ion scattering spectroscopy." Surf. Sci. **74**: 181-200.

Turkevich, A. (1961). "Chemical analysis of surfaces by use of large-angle scattering of heavy charged particles." Science **134**: 672.

Turkevich, A. L. (1968). in Surveyor Project Final Report, Part II. Scientific Results. NASA Tech. Rep. **32**: 303-387.

Watson, P. R. (1999). In preparation.

Wolfrum, K., H. Graener, et al. (1993). "Sum-frequency vibrational spectroscopy at the liquid-air interface of methanol. Water solutions." Chem. Phys. Letts. **213**: 41.

APPENDICES

Appendix A. Ion Beam Optimization and Pulsing

The first step involves introduction of a low partial pressure of the inert gas to be used, of the order of 10^{-6} Torr. Next, the beam energy is selected, at settings of 1.5, 2.0, or 2.5 kiloelectron volts. The current is then monitored at the available test points, including the pulse plate, shield, and Faraday cup. The procedure involves variation of all the parameters in succession to initially generate the most current possible at the first test point, and then to focus and steer the beam through to the target.

When a new gas is introduced, e.g. a change from Ar^+ to Ne^+ , or when the gun has been removed for maintenance, it is usually necessary to start with the simplest possible setup in order to locate the beam before optimization. In this case, the tilt positioner is aligned to a 0° offset (straight through), the Wien filter magnets removed, and the Wien filter deflection plate is grounded. This allows all masses and ionization states as well as neutrals to pass, but it makes finding the current easier by eliminating some of the variables. The total Faraday cup current is optimized under these conditions before moving forward. Once this process takes place, the Wien filter magnets are replaced and the voltage reapplied to the WF deflection plate, and again the beam is optimized. At this point, neutrals in the beam path will still pass, but mass and energy of the ions can be selected. Finally, the tilt positioner is adjusted to eliminate the neutrals in the beam, and optimization is done again.

For a given ion, the total beam current depends not only on the electrostatic optical element settings, but also the gas pressure and emission current so these parameters are optimized as well. In maximizing the beam current, adjustment of a

single parameter may improve the current to a local maximum, but changing each setting will affect several other parameters, so the adjustments must be repeated several times to obtain the best possible current.

After the continuous current is optimized, the beam must be pulsed in order to perform an experiment. When the maximum continuous current is observed at the Faraday cup, the Y1+ voltage is adjusted so that the beam current reading drops to zero ± 2 pA. In so doing, the beam is deflected completely downward and away from the pulse aperture in the vertical direction; the current is registered on the pulse plate rather than in the cup. The "A" output of the Avtech pulser is then connected to the Y1- deflection plate, so that positive pulses applied will deflect the beam upward and across the pulse aperture. The pulser output is adjusted so that the observed Faraday cup current goes through a maximum and reaches a local minimum. Physically, this signifies that the applied Y pulses are large enough to deflect the beam upward and past the pulse aperture in the Y direction. Once done, the A pulse amplitude setting is recorded and then adjusted back to zero. In the horizontal direction, the procedure must be repeated using the "B" output of the Avtech unit. The Y1+ voltage is reduced back to its original value so that the continuous current is again maximized, and voltage is applied to X1- so that the beam is deflected from the aperture in the horizontal direction. Pulses are applied to the X1+ plate and the current is observed as the X pulse amplitude is adjusted until a local minimum is obtained. At this point, the pulse amplitudes in both the X and Y directions have been established, and the Y pulse is restored to the proper setting. The PRF (pulse repetition rate) is adjusted to the maximum setting that prevents the pulser from overloading. Finally, the lens 2

elements are adjusted to optimize the pulsed beam current in the Faraday cup. It is important to monitor the current during the final optimization both when the pulser is on and off- the current when “off” must remain low, ca. 1-2 pA, and the current when “on” is maximized.

The pulse width for both the X and Y pulses is nominally set to 400 ns, and the rise time for each pulse is on the order of 10 ns. The X pulse follows the Y pulse by ca. 200 ns, or half the duration of the first pulse. This allows the vertical sweep of the beam to clear the pulse aperture before the horizontal pulse is applied.

Finally, the trigger delay is set to an appropriate value for the experiment. The trigger pulse is a 5-volt TTL signal used synchronously with the MCS unit to start counting for a time-of-flight window.

Appendix B.**Supplemental TOF-SARS Data for Bis(2-Ethylhexyl) Chlorendate**

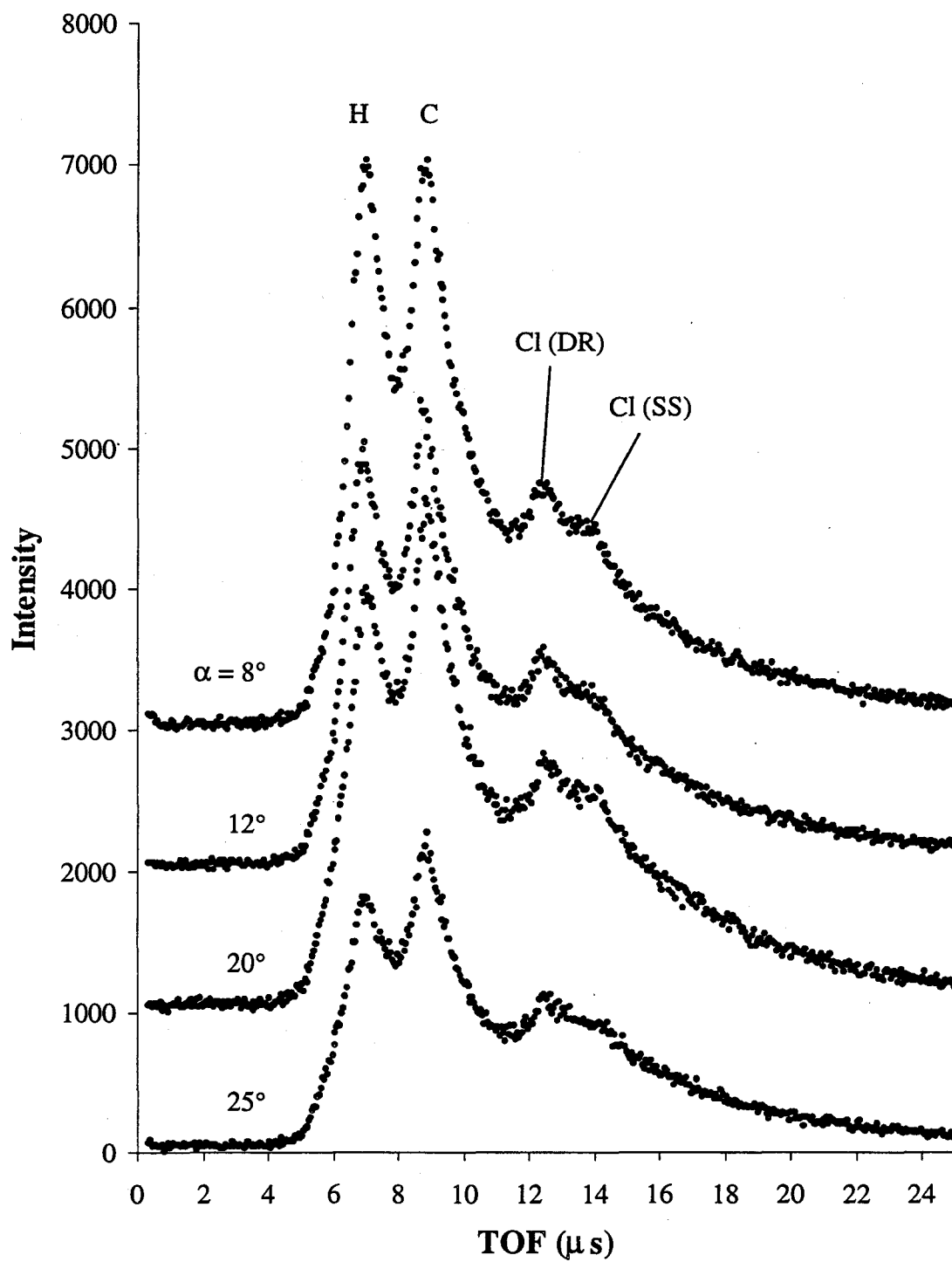


Figure B.1 Composite of TOF-SARS spectra obtained from BEHC using 3.0 keV Ar^+ ions.

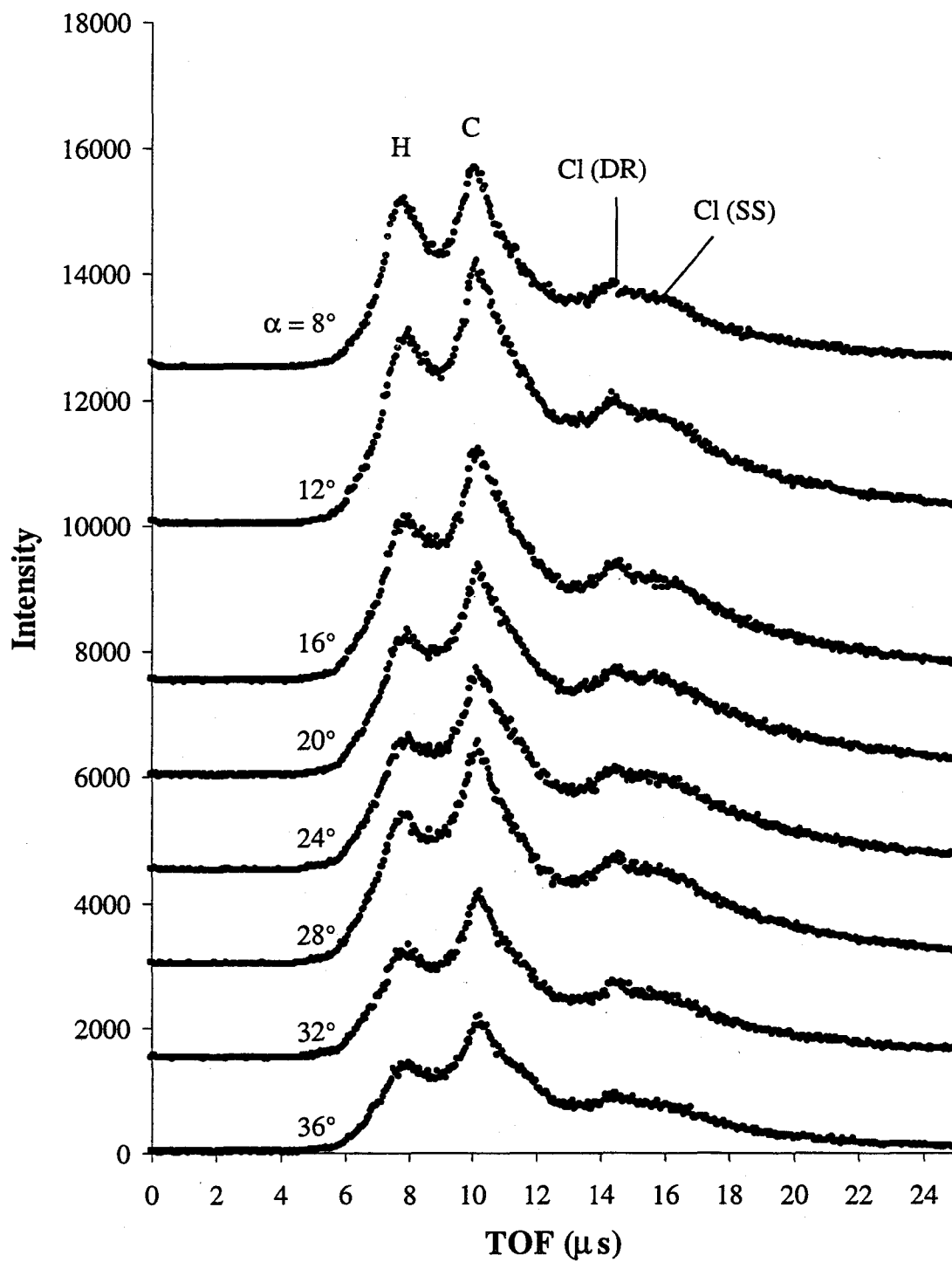


Figure B.2 Composite of TOF-SARS spectra obtained from BEHC using 2.5 keV Ar^+ ions.

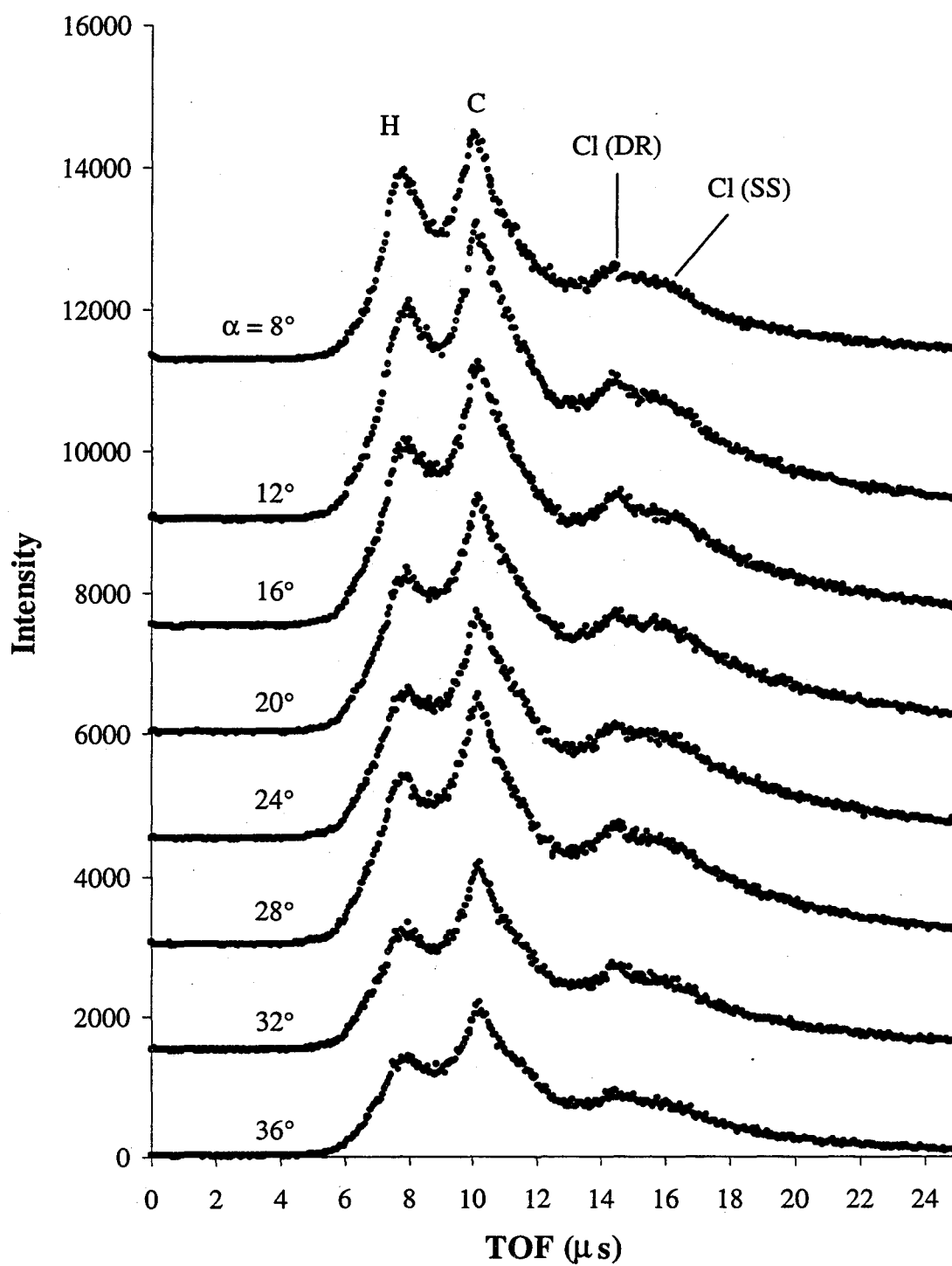


Figure B.3 Composite of TOF-SARS spectra obtained from BEHC using 2.0 keV Ar^+ ions.

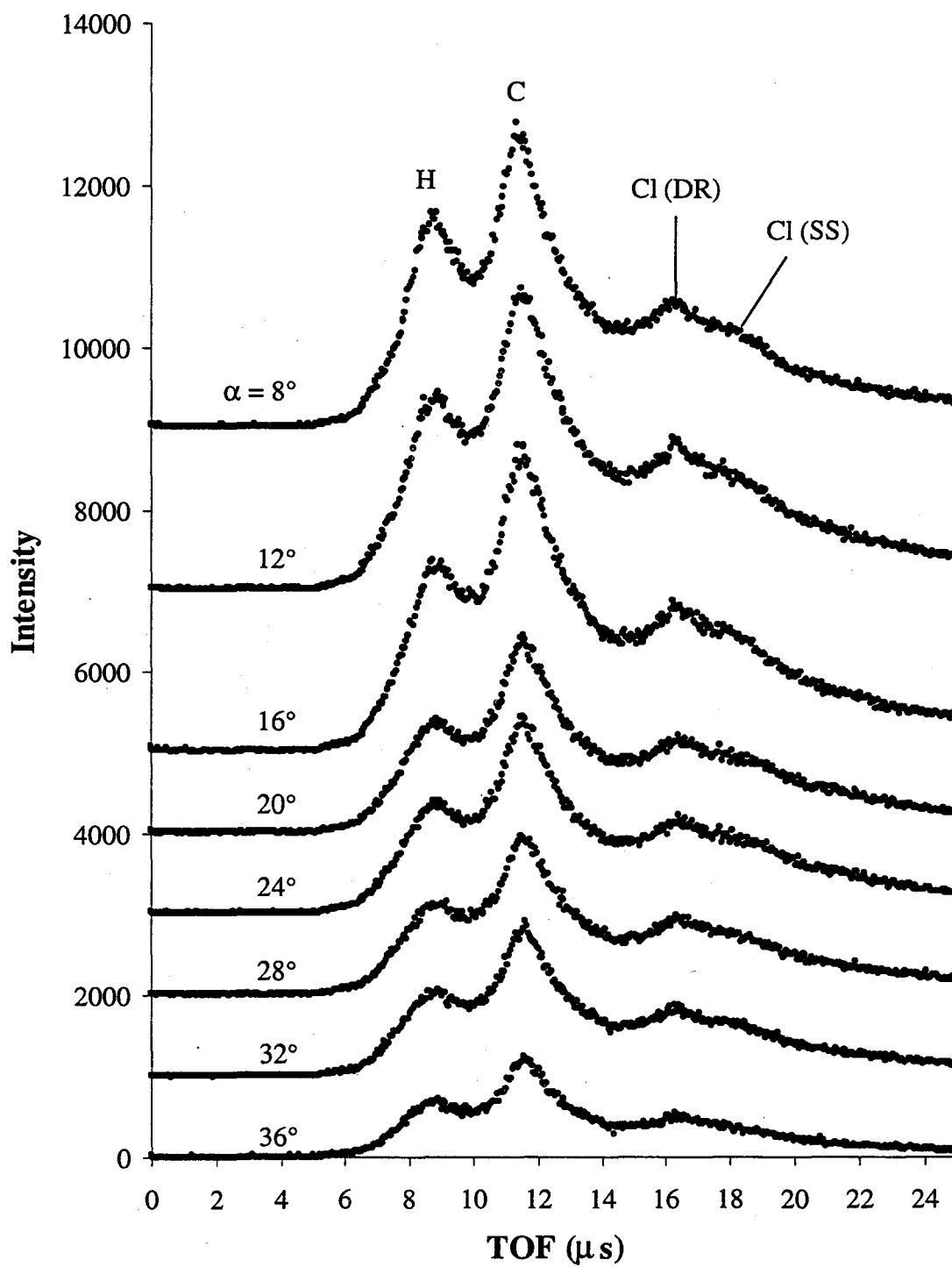


Figure B.4 Composite of TOF-SARS spectra obtained from BEHC using 1.5 keV Ar^+ ions.

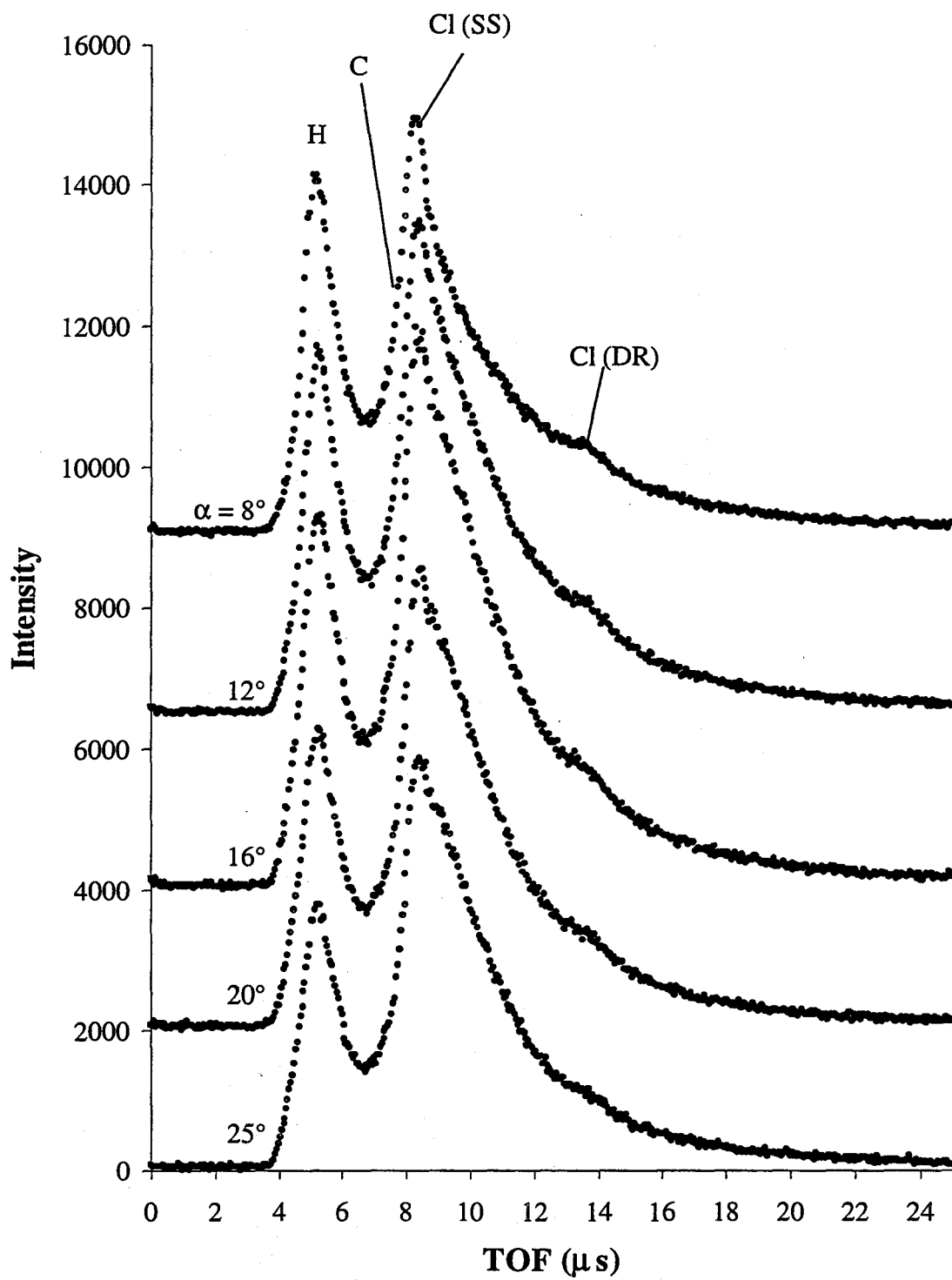


Figure B.5 Composite of TOF-SARS spectra obtained from BEHC using 2.5 keV Ne^+ ions. *C (DR) predicted TOF = 7.92 μs .

Appendix C. Calculated Recoil Cross Sections

All cross sections were calculated using the Molière potential (Equation 2.3.12) and the recoil angle $\phi = 45^\circ$.

Table C.1 Selected Recoil Cross Sections

Energy	Collision	$\sigma_{DR}, \text{\AA}^2$	E_{DR}, eV	Velocity ($\times 10^5 \text{ms}^{-1}$)
2 keV				
	Ar-H	0.313	96.1	1.36
	Ar-C	0.174	716.15	1.07
	Ar-N	0.178	764.89	1.03
	Ar-O	0.179	820.46	1.00
	Ar-F	0.178	867.85	0.94
	Ar-Cl	0.197	1005.2	0.74
	Ar-P	0.196	978.51	0.78
	Ne-H	0.112	179.76	1.86
	Ne-C	0.070	927.37	1.22
	Ne-N	0.074	949.91	1.14
	Ne-O	0.075	991.83	1.09
	Ne-F	0.075	1009.29	1.01
	Ne-Cl	0.096	929.5	0.71
	Ne-P	0.092	960.47	0.77
2.5 keV				
	Ar-H	0.257	119.69	1.51
	Ar-C	0.143	884.59	1.19
	Ar-N	0.143	966.4	1.15
	Ar-O	0.148	1012.64	1.11
	Ar-F	0.143	1097.56	1.06
	Ar-Cl	0.164	1240	0.82
	Ar-P	0.160	1233.66	0.88
	Ne-H	0.088	226.03	2.08
	Ne-C	0.055	1166.94	1.37
	Ne-N	0.058	1191.68	1.28
	Ne-O	0.059	1245.34	1.23
	Ne-F	0.059	1267.96	1.14
	Ne-Cl	0.078	1152.72	0.79
	Ne-P	0.074	1193.86	0.86